Miguel
Monteagudo
Honrubia

Universidad Pontificia Comillas
Escuela Técnica Superior de Ingeniería ICAI
Instituto de Investigación Tecnológica (IIT)

Machine Learning techniques to enhance the capacitive sensing of microwave resonant structures

Autor: Miguel Monteagudo Honrubia
Directores: Dr. Francisco Javier Herraiz-Martínez
Dr. Javier Matanza Domingo

Machine Learning techniques to enhance the capacitive sensing of microwave resonant structures

MADRID | Agosto 2024

Hay una voluntad, hay un camino.

Agradecimientos

La investigación es siempre un esfuerzo colectivo, un proceso colaborativo de intercambio de ideas con el fin de resolver problemas complejos. Gracias al trabajo compartido, el conocimiento científico avanza y se construye de manera acumulativa. Esta tesis doctoral no ha sido una excepción y cada artículo presentado en este compendio no hubiera sido posible sin la contribución de numerosas personas.

En primer lugar, quiero expresar mi más profundo agradecimiento a mis directores de tesis, Francisco Javier Herraiz-Martínez y Javier Matanza Domingo, por darme la oportunidad de trabajar en este proyecto en los complicados momentos de la pandemia del COVID-19. Junto a mi tutor, Romano Giannetti, han enriquecido significativamente este trabajo gracias a sus valiosas sugerencias y compromiso, que han sido clave para la realización de esta investigación. También quiero mencionar a los técnicos del taller de electrónica y del laboratorio de química por su amable ayuda, a todos los estudiantes que han colaborado en la realización de experimentos, y sin duda a Gianluca Caposciutti y la gente de la Universidad de Pisa por su estimable trabajo durante la colabaracion realizada durante esta tesis.

Por otro lado, quiero agradecer a todos aquellos que han sido clave para mi formación; en especial, a todos los compañeros y profesores que durante mi vida académica me influyeron para dedicarme a la investigación. Y por supuesto, agradecer el apoyo de mi familia que ha sido fundamental desde el comienzo de este viaje.

Por último, a todas las personas que han hecho de estos últimos años una experiencia agradable, mi más sincero agradecimiento.

Resumen

Durante la última década, la irrupción de nuevos paradigmas tecnológicos como el *"Internet-of-Things (IoT)"* (Internet de las cosas) o los diagnósticos *"Point-of-Care (POC)"* (en el punto de atención) ha generado un incremento significativo en la demanda de sensores *low-cost*. El desarrollo de estos paradigmas ha coincidido con la consolidación de los modelos de aprendizaje automático, o *"Machine Learning (ML)"*, como los métodos de análisis y clasificación más prometedores. Por lo tanto, esta tesis doctoral aborda la inevitable convergencia de estas tendencias y sus potenciales sinergias para la implementación de sensores *low-cost*.

La principal ventaja de este tipo de sensores es precisamente la accesibilidad de su precio, que les permite ser un elemento clave para democratizar el acceso a la tecnología. De este modo, investigadores, pequeñas empresas y comunidades con recursos limitados o en países en desarrollo pueden afrontar con las herramientas necesarias los grandes desafíos de nuestro tiempo, como pueden ser el monitoreo ambiental o la mejora de la salud pública. Por ejemplo, los dispositivos *Point-of-Care* podrían ser utilzados por los trabajadores de la salud (o incluso los propios pacientes) para obtener diagnósticos más rápidos que faciliten decisiones clínicas justo en lugar y el momento donde sean más necesarias. Además, al tratarse de pruebas fuera del laboratorio se reducen en gran cantidad los gastos operativos, lo que es particularmente beneficioso en regiones rurales o en vías de desarrollo. Por otro lado, el bajo coste de estos sensores también permite su despliegue a gran escala en una amplia variedad de entornos, incluyendo ubicaciones remotas donde la instrumentación tradicional puede resultar poco práctica o ser extremadamente costosa. Esta ubicuidad y escalabilidad permiten la medición y la recopilación de datos de forma exhaustiva en tiempo real, lo que es imprescindible para monitorear entornos urbanos, hospitales o campos agrícolas. En definitiva, los sensores *low-cost* también son la base tecnológica necesaria para que las aplicaciones IoT sean viables, eficientes y accesibles.

Considerando las características de este contexto, la investigación realizada durante esta tesis doctoral apuesta por la aplicación de estructuras resonantes

en el espectro de microondas como tecnología clave para diseñar sensores *low-cost*. Este tipo de estructuras permite desarrollar dispositivos con una alta sensibilidad y una geometría adaptable a las características de la aplicación. Sin embargo, debido a la falta de especificidad, su utilidad puede verse limitada en entornos con alto ruido ambiental o en aplicaciones complejas con muchos compuestos involucrados. Por lo tanto, el principal objetivo de este trabajo es aplicar técnicas de *Machine Learning* para mejorar la interpretación de los datos adquiridos para a obtener resultados más fiables y precisos. La integración de ambas tecnologías representa una investigación interdisciplinar, cuyos resultados contribuyen a ampliar los límites y utilidades de los sensores *low-cost*.

El primer capítulo de esta tesis doctoral es una breve introducción al estado del arte para ayudar al lector a adentrarse en el contexto de esta investigación. Primero se define sensor como cualquier dispositivo capaz de detectar información de su entorno y reaccionar transformando esa información en una señal eléctrica que puede ser utilizada por otros dispositivos (u operadores humanos) en una infinidad de aplicaciones. Dado el fenómeno que define su principio de funcionamiento, los sensores pueden clasificarse principalmente entre químicos o físicos, de los cuales esta tesis se centra en los sensores electromagnéticos. Este tipo de sensores se basa en la interacción entre la materia y las ondas electromagnéticas como mecanismo de detección. Dependiendo de la frecuencia de la onda incidente, se manifiestan diferentes fenómenos que se pueden aprovechar para medir diferentes características. Por ejemplo, los sensores ópticos son la base de las técnicas de fluorescencia o espectrografía que se utilizan ampliamente tanto en laboratorio como en la práctica clínica. Sin embargo, requieren de complejos sistemas de medida que dificultan su miniaturización. Por lo tanto, de entre todos los tipos de sensores electromagnéticos, esta tesis doctoral propone la aplicación de estructuras resonantes en el espectro de microondas como sensores capacitivos. Este tipo de sensores detecta cambios en la capacitancia del medio cercano, que son proporcionales a permitividad de la muestra de interés, y que se traducen en una variación de la frecuencia de resonancia del sensor. Entre sus principales ventajas se

incluye su tamaño ajustable y permitir un análisis no destructivo como muy poca o nula preparación de la muestra.

La revisión del estado del arte destaca el interés exponencial en la literatura científica por la combinación de sensores y *Machine Learning*, destacando el impacto y la relevancia de esta tesis. Además, las publicaciones presentes en la literatura se centran únicamente en la combinación con sensores electroquímicos u ópticos. Por lo tanto, la ausencia de sensores capacitivos basados en resonadores de microondas se presenta como una clara oportunidad de investigación. Este campo de la Inteligencia Artificial consiste en el aprendizaje automático de patrones complejos en un conjunto de datos para poder realizar predicciones sobre nuevas adquisiciones. De este modo, los modelos de ML permiten analizar las señales del sensor, mejorando significativamente la capacidad de detección. Hay dos principales tipos de aprendizaje, supervisado y no-supervisado, dependiendo de si los modelos tienen acceso o no a información previa sobre el conjunto de datos. Los modelos supervisados se aplican a tareas de regresión o clasificación automática, mientras que los modelos no-supervisados se utilizan para clustering o reducción de dimensionalidad. Ambos tipos de aprendizaje son utilizados en esta tesis doctoral, ya que ofrecen una metodología alternativa para calibrar el sensor y mejorar su robustez ante el ruido. Además, los modelos generativos de *Deep Learning* pueden aprender de manera no-supervisada una representación latente de la información contenida en las señales adquiridas. De este modo se puede lograr la generación sintética de señales para mejorar la calidad del conjunto de datos de entrenamiento del sensor.

Terminada la revisión del estado del arte, los Capítulos 3, 4 y 5 forman un compendio de artículos publicados en revistas de alto impacto y representan el corpus principal de esta tesis doctoral. El primero de ellos (Capítulo 3) es un proyecto colaborativo con la Universidad de Pisa: *"Measuring Sedimentation Profiles for Nanoparticle Characterization through a Square Spiral Resonator Sensor"*. Este trabajo propone un novedoso método para caracterizar dispersiones de nanopartículas en parafina líquida utilizando un sensor basado en resonadores planos de espiral cuadrada. El artículo desarrolla un protocolo

de medida para inferir las características de las nanopartículas a través de la valoración de sus perfiles de sedimentación. Los resultados demuestran que el método propuesto es una alternativa rápida y de bajo coste en comparación a los procedimientos tradicionales para caracterizar nanopartículas. Este trabajo es un ejemplo práctico de cómo los sensores *low-cost* son una alternativa a las técnicas tradicionales de laboratorio, como pueden ser la microscopía electrónica o la espectrografía de rayos X; técnicas que en hoy en día son esenciales para la fabricación controlada de nanopartículas.

Sin embargo, el principal inconveniente del trabajo anterior es la necesidad de utilizar instrumentación electrónica comercial para operar con los sensores capacitivos. Por lo tanto, el segundo artículo de este compendio, "*"Low-Cost Electronics for Automatic Classification and Permittivity Estimation of Glycerin Solutions Using a Dielectric Resonator Sensor and ML Techniques"*, explora una alternativa al analizador vectorial de redes (VNA). Aunque este dispositivo no es comparable a instrumentos más sofisticados con protocolos más limitantes, el VNA sigue siendo un aparato de un precio significativo, voluminoso y contrario a las necesidades de las aplicaciones IoT/PoC. Por esta razón, el objetivo de este artículo (Capítulo 4) es comparar la calidad de los resultados de un VNA comercial con respecto a un novedoso lector portátil basado electrónica *low-cost* diseñado por investigadores del Instituto de Investigación Tecnológica (IIT). En esta investigación se utiliza un sensor basado en un resonador dieléctrico con una pequeña cavidad para analizar la concentración de disoluciones de glicerina. Las señales adquiridas sirven como datos de entrenamiento para diferentes modelos de *Machine Learning*. A través de la clasificación automática de estas disoluciones y la estimación de su permitividad mediante regresión se pueden evaluar ambos sistemas de medidas. Los resultados demuestran que la aplicación de estos modelos permite que el lector electrónico *low-cost* tenga un rendimiento comparable a la instrumentación comercial.

Aunque los resultados del Capítulo 4 fueron prometedores, el desarrollo del artículo estuvo limitado por las fórmulas empleadas para estimar la permitividad de la mezcla de líquidos binarios. Esta limitación es crítica ya que la permitividad es el valor requerido para entrenar correctamente los modelos de

regresión y realizar predicciones sobre las muestras analizadas por los sensores capacitivos. Por lo tanto, el tercer artículo, *"A ML approach for enhancing permittivity mixing rules of binary liquids with a Gaussian modification and a new interaction factor estimation"*, propone utilizar estos modelos de regresión para investigar la permitividad de las disoluciones y de que factores depende. En la literatura científica se propone modificar estas fórmulas de mezcla con un parámetro que conceptualiza la interacción molecular entre los componentes de la disolución. Este artículo (Capítulo 5) parte de esta línea de investigación, y propone obtener mejores estimaciones de permitividad encontrando el rango óptimo del factor de interacción que minimiza el error de regresión de los modelos ML. Los resultados indican que este enfoque también se podría utilizar para validar medidas experimentales de permitividad o seleccionar que formula de mezcla es la más adecuada para una disolución binaria específica. Además, aplicando esta metodología como demostración, el artículo propone una fórmula para estimar el factor de interacción utilizando las propiedades los componentes de la mezcla. Además, se propone una fórmula de modificación alternativa basada en una función gaussiana multiparamétrica. Ambas propuestas permiten mejorar el modelado de las propiedades dieléctricas de mezclas binarias y obtener estimaciones de permitividad más fidedignas.

Finalmente, como continuación a los artículos publicados, el Capítulo 6 introduce una aplicación indirecta para mejorar las capacidades de los sensores aumentando el tamaño y la calidad de los datos de entrenamiento. Mediante un *Variational Autoencoder* (VAE) entrenado para generar señales sintéticas se propone rectificar posibles problemas durante la adquisición de medidas del sensor. Por ejemplo, un desequilibrio de clases en el conjunto de datos de entrenamiento o un tamaño insuficiente de señales pueden limitar la precisión de los modelos ML. Por otro lado, generar señales sintéticas también podría reducir el número de experimentos necesarios y reducir el coste de construcción del dataset, que para ciertas aplicaciones podría ser una tarea extremadamente costosa. Además, el aprendizaje representativo del VAE también permiten la interpolación de señales no medidas por el sensor. Los resultados preliminares plantean una base sólida para desarrollos futuros para mejorar

los conjuntos de datos de entrenamiento. Actualmente una versión extendida de este capítulo se está preparando para su publicación a una revista de revisión por pares.

En conclusión, las publicaciones incorporadas a esta tesis doctoral han abierto muchas líneas de investigación interesantes que pueden ser continúadas en futuros trabajos. De hecho, las metodologías propuestas para mejorar el rendimiento de los sensores capacitivos basados en estructuras resonantes en el espectro de microondas no se limitan exclusivamente a este tipo de sensores. De hecho, podría aplicarse a cualquier tecnología o diseño de sensores. Por lo tanto, se deben realizar más estudios probando nuevos objetivos analíticos para confirmar la versatilidad de estas metodologías y alcanzar todo su potencial. En definitiva, la aplicación de técnicas de *Machine Learning* han conseguido contribuciones significativas al desarrollo de sensores *low-cost*.

Summary

During the last decade, new technological paradigms such as the Internet-of-Things (IoT) or Point-of-Care (POC) diagnostics have significantly increased demand for low-cost sensors. The development of these paradigms has coincided with the consolidation of Machine Learning (ML) models as the most promising methods for analysis and classification. Thus, this PhD thesis addresses the inevitable convergence of all these trends and their potential synergies for implementing low-cost sensors.

The main advantage of this type of sensor is precisely their price accessibility, which appoints them as the key element to democratize access to sensing technology. Thus, researchers, small businesses, and communities with limited resources or in developing countries can address the major challenges of our time with more resources, such as environmental monitoring or improving public health. For example, Point-of-Care devices could be used by healthcare workers (or even patients themselves) to obtain faster clinical decisions right at the place and moment they are most needed. Additionally, since the POC diagnostics are conducted outside the laboratory, operational costs are significantly reduced, which is particularly beneficial in rural or developing regions. Furthermore, the affordability of these sensors enables a large-scale deployment in a wide variety of settings, including remote locations where traditional instrumentation might be impractical or extremely expensive. This ubiquity and scalability achieve comprehensive real-time data measurement and collection, which is essential for monitoring urban environments, hospitals, or agricultural fields. Therefore, low-cost sensors are the fundamental technology that makes IoT applications viable, efficient, and accessible.

Considering the characteristics of this context, the research conducted during this PhD focuses on the application of microwave resonant structures as the key technology for designing low-cost sensors. These structures enable the development of high-sensitivity devices with a geometry adaptable to the characteristics of the application of interest. However, due to their lack of specificity, their performance may be limited in environments with high ambient noise or for complex applications with several mixed compounds. Therefore,

the main objective of this work is to apply ML techniques to enhance the interpretation of the acquired data to obtain more reliable and accurate results. The integration of both technologies represents an interdisciplinary investigation whose results contribute to expanding the limits and capabilities of low-cost sensors.

The first chapter of this thesis is a brief introduction to the state-of-the-art for presenting the context of this research to the reader. First, a sensor is defined as any device capable of detecting information from its environment and reacting by transforming that information into an electrical signal interpreted by other devices (or human operators) in countless applications. According to the phenomenon that defines its operating principle, sensors can mainly be classified as chemical or physical, with this thesis focusing on electromagnetic sensors. This type of sensor is based on the interaction between matter and electromagnetic waves as a detection mechanism. Depending on the incident wave frequency, different physical phenomena can be exploited to measure target characteristics. For example, optical sensors are the basis for fluorescence or spectroscopy techniques, which are widely used both in laboratory and clinical practice. However, they require complex measurement systems that hinder their miniaturization. Therefore, among all types of electromagnetic sensors, this PhD thesis proposes the application of microwave resonant structures as capacitive sensors. These types of sensors detect changes in the nearby medium capacitance, which are proportional to the permittivity of the sample of interest, and it is detected as a variation of the sensor's resonance frequency. Their main advantages include their tuneable design and enabling a non-destructive analysis with minimum sample preparation.

The review of the state of the art highlights the exponential interest in the scientific literature regarding the combination of sensors and Machine Learning, emphasizing the impact and relevance of this PhD thesis. Additionally, the publications currently available in the literature focus exclusively on the combination with electrochemical or optical sensors. Therefore, the absence of capacitive sensors based on microwave resonators presents a clear research opportunity. This field of Artificial Intelligence involves the automatic learning

of complex patterns in the dataset in order to make predictions on new acquisitions. Thus, ML models analyzing the sensor signals can significantly improve their detection capabilities. There are two main types of learning, supervised and unsupervised, depending on whether the models have prior information about the dataset. Supervised models are applied for regression or automatic classification tasks, while unsupervised models are used for clustering or dimensionality reduction. Both types of learning are used in this doctoral thesis, as they offer an alternative methodology for calibrating the sensor and improving its robustness against noise. Moreover, unsupervised Deep Learning generative models can learn the latent representation of the information of the acquired signals. Thus, synthetic signal generation can be achieved to enhance the quality of the sensor's training dataset.

After the state-of-the-art introduction, the following chapters 3, 4 and 5 represent a compendium of articles published in high-impact journals, which is the main corpus of this PhD thesis. The first article (Chapter 3) is a collaboration with the University of Pisa:*"Measuring Sedimentation Profiles for Nanoparticle Characterization through a Square Spiral Resonator Sensor"*. This work proposes a novel method for characterizing nanoparticle dispersions in liquid paraffin using a sensor based on planar spiral resonators. The article develops a measurement protocol to infer the nanoparticle's characteristics through the assessment of their sedimentation profiles. The results demonstrate that the proposed method is a fast and low-cost alternative compared to traditional procedures for characterizing nanoparticles. This work is a practical example of how low-cost sensors are an alternative to traditional laboratory techniques, such as electron microscopy or X-ray spectroscopy, which are essential today for nanoparticle-controlled fabrication.

However, the main drawback of the previous work is the need to use commercial electronic instrumentation to operate with capacitive sensors. Therefore, the second article in this compendium, *"Low-Cost Electronics for Automatic Classification and Permittivity Estimation of Glycerin Solutions Using a Dielectric Resonator Sensor and ML Techniques"*, explores an alternative to the vector network analyzer (VNA). Although this device is not comparable to more complex

instruments with more limiting protocols, the VNA remains as a significantly expensive, bulky device that does not fulfill the requirements of IoT/PoC applications. For this reason, the aim of this article (Chapter 4) is to compare the quality of the results between a commercial VNA and a novel portable reader based on low-cost electronics designed by researchers at the Institute of Technological Research (IIT). This work uses a sensor based on a dielectric resonator with a small cavity to analyze the concentration of glycerin solutions. The acquired signals serve as training data for different ML models. Both measurement systems can be evaluated by automatically classifying glycerin solutions and estimating their permittivity through regression. The results demonstrate that the application of these models ensures that the low-cost electronic reader performs comparably to commercial instrumentation.

Although the results from Chapter 4 were promising, the development of the article was limited by the mixing-rules used to estimate the permittivity of binary liquid mixtures. This limitation is critical because permittivity is the required value for training regression models and making predictions about the samples analyzed by capacitive sensors. Therefore, the third article, *"A ML approach for enhancing permittivity mixing rules of binary liquids with a Gaussian modification and a new interaction factor estimation"*, proposes using these regression models to investigate the solution's permittivity. The scientific literature suggests modifying these mixing-rules with a parameter that conceptualizes the molecular interaction between the solution's components. This article (Chapter 5) follows this research line and proposes obtaining better permittivity estimations by finding the optimal interaction factor that minimizes the regression error from ML models. The results indicate that the proposed approach could be applied to validate experimental permittivity measurements and select the most suitable mixing-rule for a specific binary solution. Besides, by applying this methodology as a demonstration, the article proposes a formula to estimate the interaction factor using the properties of the mixture's components. In addition, an alternative modification formula based on a multiparametric Gaussian function is proposed. Both proposals improve the modeling of the dielectric properties of binary mixtures and provide more ac-

curate permittivity estimation.

Finally, as a continuation of the published articles, Chapter 6 introduces an indirect application to enhance sensor capabilities by increasing the size and quality of training data. A Variational Autoencoder (VAE) trained to generate synthetic signals is proposed to address potential issues during sensor data acquisition. For example, class imbalance in the training dataset or insufficient signal size can limit the accuracy of ML models. Additionally, generating synthetic signals could reduce the number of necessary experiments and decrease the cost of dataset construction, which can be expensive for certain applications. Moreover, representation learning from VAE can interpolate signals that are not measured by the sensor. Preliminary results establish a solid foundation for future research for improving training datasets. Currently, an extended version of this chapter is being prepared for submission to a peer-reviewed journal.

In conclusion, the publications included in this PhD thesis have opened many interesting lines of research that can be continued in future works. In fact, the methodologies proposed to improve the performance of capacitive sensors based on microwave resonant structures are not limited exclusively to this type of sensor. Indeed, they could be applied to any sensor technology or design. Therefore, further studies should be conducted to test new analytical targets in order to confirm the versatility of these methodologies and achieve their full potential. Definitively, the application of Machine Learning techniques has made significant contributions to the development of low-cost sensors.

Contents

List of Figures

List of Tables

CHAPTER 1

INTRODUCTION

1.1. Motivation: Why Low-Cost sensors?

Over the past decade, the irruption of the Internet of Things and Point-of-Care diagnostics has increased the demand for low-cost (bio) sensors. At the same time, this trend has evolved in parallel to the growing field of Machine Learning (ML), and therefore, this PhD research addresses the inevitable convergence of both technologies (Figure 1.1).

The importance of low-cost sensors lies precisely in their price accessibility for any user, making them available to small businesses, researchers, and especially for communities with limited resources in developing countries. Thus, low-cost sensors are the key to democratizing sensor technology, empowering communities and individuals to address challenges in diverse domains such as environmental monitoring or public health surveillance. For example, Point-of-Care devices could be employed by healthcare workers or even patients to obtain rapid results and clinical decisions outside the laboratory, thus reducing the associated operational costs, which is particularly beneficial in undeveloped or rural regions.

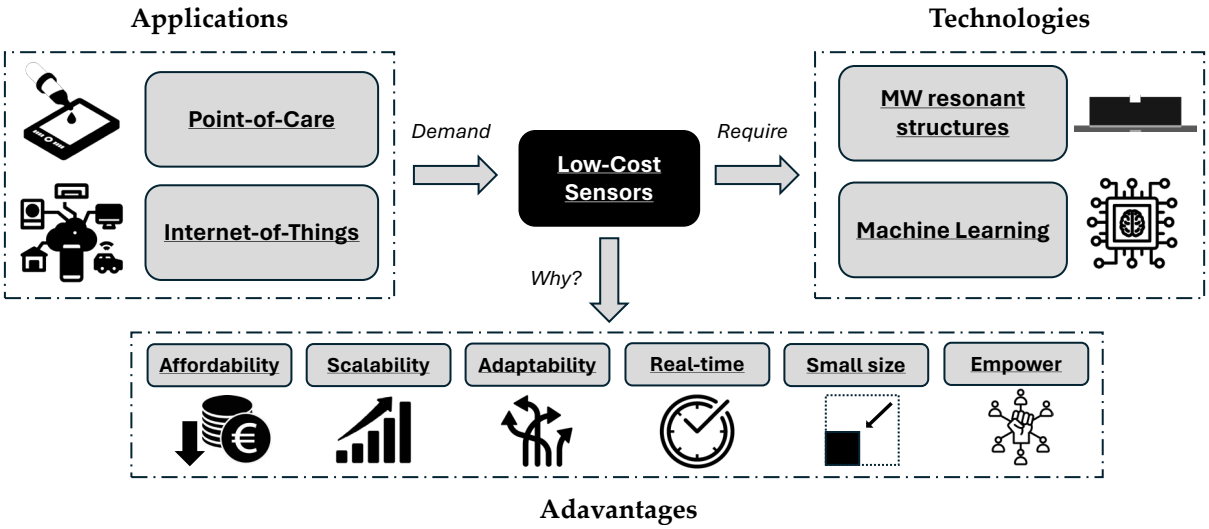

Figure 1.1: *An overview of low-cost sensors applications and advantages and the proposed technologies to develop them.*

In fact, their affordability enables the deployment of sensors on a large scale across a wide variety of environments, including remote or challenging locations where traditional instrumentation may be impractical or cost-prohibitive (Figure 1.1). This ubiquitous and scalability align perfectly with the needs of the Internet of Things applications, enabling extensive monitoring and data collection. Therefore, low-cost sensors can lead to a better understanding of complex systems, such as urban environments, hospitals, or agricultural fields. In that way, open data initiatives and collaborative platforms can leverage low-cost sensor networks to create shared repositories of real-time data, fostering transparency and collaboration.

Low-cost sensors provide the technological foundation that makes these applications feasible, efficient, and accessible (Figure 1.1). Given this context, this PhD research focuses on Microwave (MW) resonant sensors as the key technology for developing low-cost sensors. Although this sensor type has the potential to be both cost-effective and highly sensitive, due to the lack of specificity, its performance can be hindered by environmental noise or complex applications with many analytes involved. Nevertheless, by integrating ML techniques, this PhD research aims to enhance sensing data interpretation, leading to more accurate and reliable measurements. This integration is expected

to result in significant performance improvements, pushing the boundaries of what low-cost sensors can achieve and contributing to the broader field of sensor technology and its applications.

In summary, this PhD thesis is driven by the urgent need for affordable sensing solutions and the potential for significant technological progress. Indeed, the intersection of ML and MW resonant structures represents a rich interdisciplinary research area. Therefore, this PhD research aims to make a meaningful contribution to developing the next generation of low-cost sensors.

1.2. Objetives: Machine Learnig, How?

The principal objective for this PhD thesis is to leverage ML techniques to enhance the capacitive sensing capabilities of MW resonant structures, thereby developing low-cost, high-performance sensors. In order to fulfill this objective, this research established the following secondary objectives as milestones:

- **(O-0) –** Explore the state-of-the-art to identify gaps in current research and potential areas where ML could significantly contribute to improve sensing applications. This includes an analysis of the electromagnetic sensing principle, its advantages, limitations, and possible synergies with ML techniques.

- **(O-1) –** Establish a baseline example of how MW resonant sensors can offer a low-cost alternative to traditional laboratory practices.

- **(O-2) –** Implement ML models to enhance the sensitivity and reliability of sensors, therefore enabling the substitution of complex instrumentation by low-cost electronics and open-hardware.

- **(O-3) –** Demonstrate how the trained models with sensor signals can help investigate the sensing principle's nature and improve the interpretation of the results.

- **(O-4) –** Develop Deep Learning models to generate realistic synthetic data that could increase the size and quality of the acquisition dataset, as well as allow the interpolation of undetected signals.

Fulfilling these objectives will contribute to MW engineering, computer science, and applied physics, fostering collaboration and innovation across these fields. In addition, the outcomes of this PhD research aspire not only to advance academic knowledge but also to catalyze real-world applications.

1.3. Thesis Outline

The corpus of this PhD thesis consists of three published papers and the preliminary results of a fourth work in preparation to be submitted for peer-review (Figure 1.2). Each of these works addresses one of the proposed objectives. In addition, an introduction to the state-of-art is included to establish the context of this research **(O-0)**.

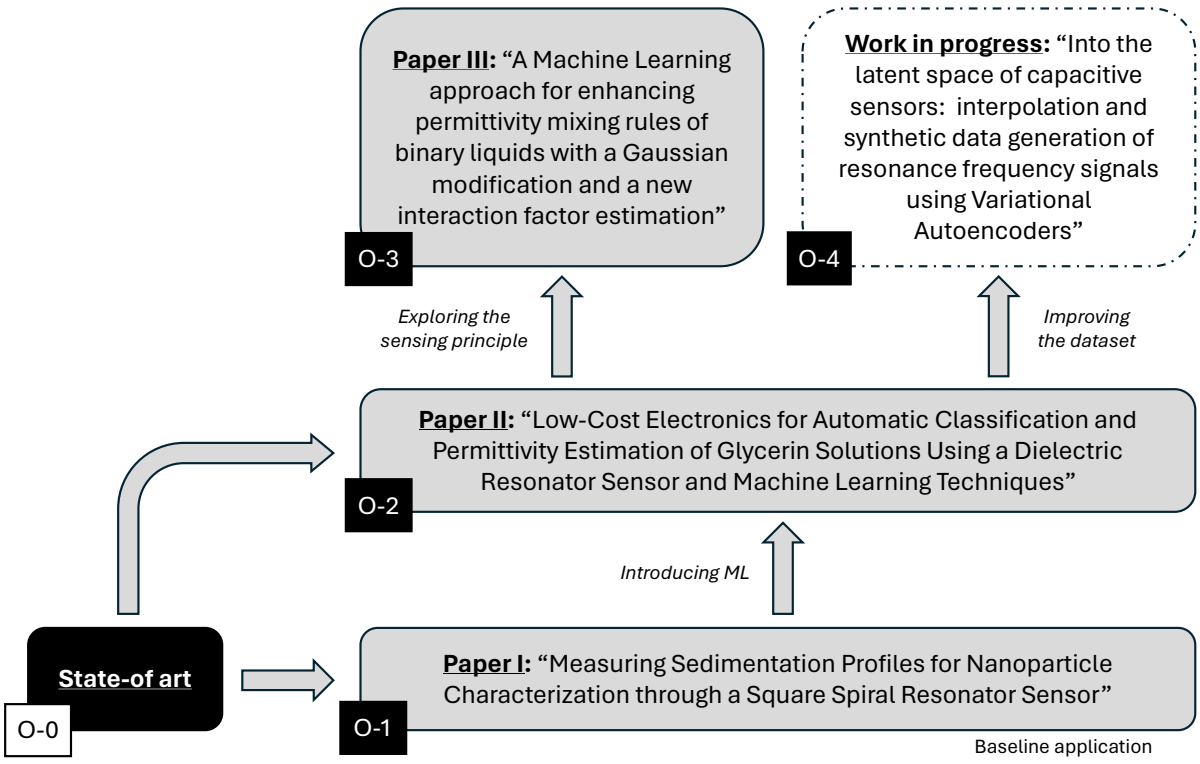

Figure 1.2: *Thesis outline showing the relationship between papers and the objectives addressed.*

Thus, Chapter 2 briefly explains the fundamentals of sensors and the advantages of MW resonant structures for low-cost sensing applications. Moreover, this revision recapitulates the uses of ML in the literature for developing intelligent sensors and proposes the novel application of Deep Learning generative models for data augmentation.

Measuring Sedimentation Profiles for Nanoparticle Characterization through a Square Spiral Resonator Sensor

The first paper of this compendium (Chapter 3) is a collaborative work with the University of Pisa. Using a MW sensor based on Square Spiral Resonators, the paper proposes a measurement system for the sedimentation profile of nanoparticles in liquid paraffin dispersions. The main objective of the paper is to reveal the nanoparticle properties from the analysis of the sedimentation dynamics. The results proved that initial concentration or chemical composition impacts the sedimentation profile. Therefore, variables such as sedimentation time or curve steepness could be analyzed in future works to characterize other properties, such as nanoparticle size distribution, which highly influences dispersion stability and is critical for many applications. In conclusion, the proposed method could represent a low-cost alternative to standard techniques for characterizing nanoparticles, such as electron microscopy **(O-1)**.

Low-Cost Electronics for Automatic Classification and Permittivity Estimation of Glycerin Solutions Using a Dielectric Resonator Sensor and ML Techniques

The second paper (Chapter 4) addresses the main drawback of the previous baseline example: the need for complex electronic instruments, such as a Vector Network Analyzer (VNA), to operate with MW sensing techniques. For this reason, the second paper aimed to compare the performance of a commercial VNA and a novel low-cost portable electronic reader designed by researchers

of the Instituto de Investigación Tecnológica (IIT). A Dielectric Resonator sensor with a small cavity is used to measure several glycerin solutions with both acquisition systems. The signals collected served as a training dataset for ML models to perform the classification of glycerin solutions and the regression of their permittivity. The results prove that applying these models ensures that the low-cost electronic reader performs comparable to the commercial instrumentation **(O-2)**.

A ML approach for enhancing permittivity mixing rules of binary liquids with a Gaussian modification and a new interaction factor estimation

The previous article had to deal with the physical limitations of mixing rules to estimate the permittivity of binary liquids, which is a critical value to train regression models correctly. Consequently, the third paper (Chapter 5) aims to enhance the traditional mixing rules with interaction factors that address the mixture characteristics. This article proposed to find the optimal value of these tunable parameters by minimizing the regression error of ML models. The insights of this research lead to a novel Gaussian modification formula that improves the modeling of the dielectric properties of binary mixtures **(O-3)**.

Into the latent space of capacitive sensors: interpolation & synthetic data generation of resonance frequency signals using Variational Autoencoders

Finally, the follow-up of this PhD research is an indirect application to improve the performance of sensors (Chapter 4). This work is currently being prepared for submission to a peer-reviewed journal. Instead of focusing on the sensing data analysis, this approach seeks to rectify issues in the training dataset, such as insufficient size or class imbalance **(O-3)** This work applies generative models, one of the most promising Deep Learning techniques, to obtain realistic synthetic signals from the sensor. Thus, the dataset can be expanded, leading to better results or completed with fewer experiments.

CHAPTER 2

STATE-OF-THE-ART

2.1. Sensors everywhere

A sensor is any device able to detect any information input from its external environment and react by transforming this input into valuable insights for other devices or human users (Figure 2.1) [1]. This definition may sound vague, but it fits with the vast collection of sensor types. In fact, many different effects in physics, chemistry, or biology can be employed as the sensing element that converts the target input into an electrical signal [2]. However, sensors are exposed to external disturbance variables that represent noise sources that corrupt the output and limit sensor functionality. Therefore, sensors require an electronic system to process the electric signal, i.e., filtering the noise and/or enhancing signal characteristics by amplification or Fourier transformation [3]. Recently, due to advances in miniaturization, the sensor element and its evaluation electronics can be integrated into a single unit known as a "smart sensor" [4]. Likewise, different sensors can be integrated together to form complex instruments for very specific applications or scientific tasks.

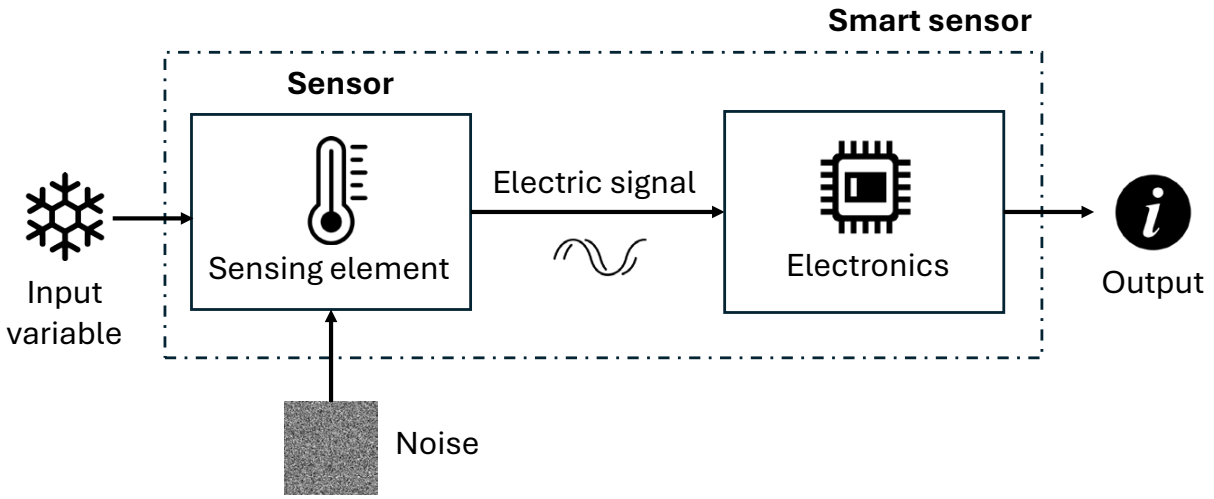

Figure 2.1: *Workflow diagram of a temperature (smart) sensor showing the relationship between inputs and main elements.*

There are many approaches to classifying sensors, and most of them address their mode of operation. For example, sensors can be divided into active or passive if they need an external energy source, digital or analogic, depending on their output signal, contact or contactless whether the sensitive element physically touches the target [2]. Besides, sensors can be classified according to the three main sensing mechanisms: physical sensors (i.e., electromagnetic or mechanical), chemical sensors, and biosensors [5]. This is just a brief overview since the focus of this thesis is on capacitive sensors. The reader interested in a more complete discussion may consult the proposed bibliography [1, 5, 6, 7].

As introduced before, this variety of sensors can fulfill the needs of numerous applications. Consequently, sensors are ubiquitous worldwide, playing a critical role in many common applications such as consumer electronics [8], medical devices [9], or environmental monitoring [10]. For example, in agriculture, measuring soil moisture, air humidity, and temperature would optimize irrigation and crop management [11]. In the same way, sensors are essential in enhancing efficiency and security in industrial processes since monitoring by gathering data that can be used for automation, monitoring, and control [12]. On the other hand, sensors have a great human impact; indeed, the development of medicine in the last century has been impulsed by sensors that

enable more precise diagnostics and personalized patient attention by recording vital signs such as heart rate or blood pressure [13]. In addition, it is worth highlighting the development of biosensors, which aim to translate complex laboratory diagnostics into portable devices at the "Point-of-Care" [14].

In a biosensor, the sensing element is a receptor-transducer system that converts a biological response into a measurable signal, providing analytical data to detect specific analytes or clinical insights [15]. In this specialized sensor, the biological recognition element (such as enzymes, antibodies, or nucleic acids) provides selectivity and specificity since it only interacts with the target analyte, which is commonly mixed with other substances [16]. Afterward, as in a regular sensor, the transducer converts this biological interaction into a measurable signal (Figure 2.2).

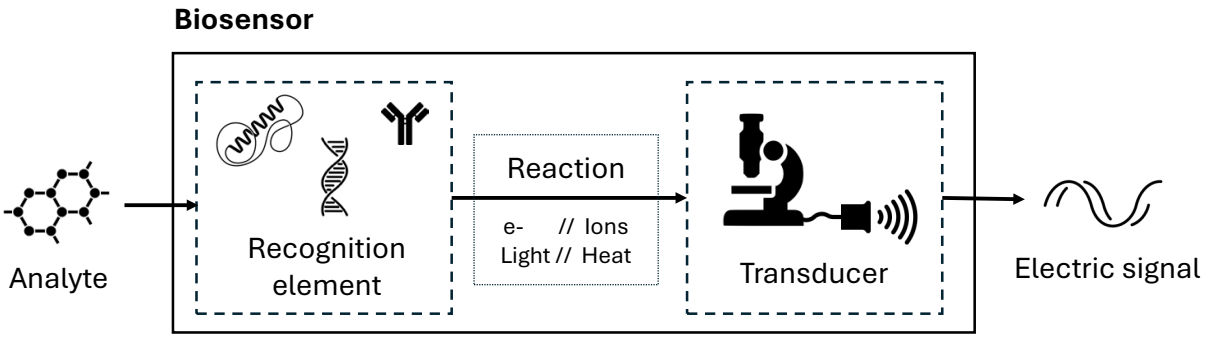

Figure 2.2: *Workflow diagram of a biosensor showing the most common recognition elements (antibodies, proteins, and DNA), as well as the main reaction products to be converted by the transducer.*

There are many types of biosensors depending on the physical phenomenon used by the transducer to collect information about the biological process. At the present time, the most popular biosensors have been electrochemical, which take advantage of known biochemical reactions to recognize the presence of analytic targets [17]. This is the case with glucometers, which allow the precise measurement of blood glucose concentration by means of the glucose oxidation reaction [18]. The development of these devices has significantly helped diabetic patients to live with their pathology.

Although biosensors are out of the scope of this PhD research, the proposed

capacitive sensors and ML analysis techniques can be supporting technologies for future developments of biosensing applications. Indeed, as an example case, despite the proven effectiveness of electrochemical biosensors, they have a number of drawbacks that limit the range of uses and applications [19]. First of all, they depend on finding a target biochemical reaction in a controlled environment, which is not always possible. Moreover, the reusability and cost-effectiveness of these sensors can be limited due to a complex sample preparation that requires several reagents, as well as controlling electrode biofouling [20]. In the same way, biorecognition elements are affected by the exposition to variations in temperature, pH, and ionic strength, and therefore, losing their activity and stability in the long term [21].

In contrast, electromagnetic sensing relies on the interaction between an incident electromagnetic field and matter as the phenomena to obtain valuable information. Indeed, optical sensors have been proven to be a solid alternative for sensing applications [22, 23]. In particular, this PhD research focuses on microwave (MW) capacitive sensors that, although they are not so common as (bio)sensors, have been successfully employed in other fields such as dielectric characterization [2, 24, 25]. The advantages and principles of this type of sensor will be studied in the following sections, highlighting them as an interesting alternative for developing low-cost sensors.

2.2. Into the electromagnetic interaction with matter

Electromagnetic (EM) sensing highly depends on the frequency range of the incident EM wave since it will define the nature of the physical interaction with the analyzed substance and reveal different characteristics accordingly [26]. For example, optical sensors operate with the visible or near-infrared spectrum, detecting energy transfer phenomena, such as changes in absorbance or fluorescence, or propagation effects, such as reflectance or refractive index variations [27]. In fact, among optical sensors, those based on fluorescence

techniques are the most popular, achieving a competitive performance similar to electrochemical biosensors, but mostly due to the extensive know-how acquired during decades of traditional laboratory practice [28]. In contrast, other optical sensing techniques, such as Raman Spectroscopy [29] or Surface Plasmon Resonance [30], are more sensitive and target-specific but at the cost of far more complex methodologies hard to implement in the industry.

On the other hand, at lower frequencies beyond the infrared, in the MW and RF spectrum, variations in the dielectric properties of matter can be appreciated. When an MW field interacts with the target sample, the internal charges are redistributed according to the orientation of the incident field [31]. This process is defined as polarization and is traced in terms of permittivity and conductivity. During the polarization, the charge rearrangement causes a permittivity change that reveals information about its chemical composition [32]. Moreover, "polarization" is not a unique phenomenon; indeed, it is the sum of different polarization effects (Figure 2.3,2.4), which contribute differently according to the EM frequency and the sample characteristics [26].

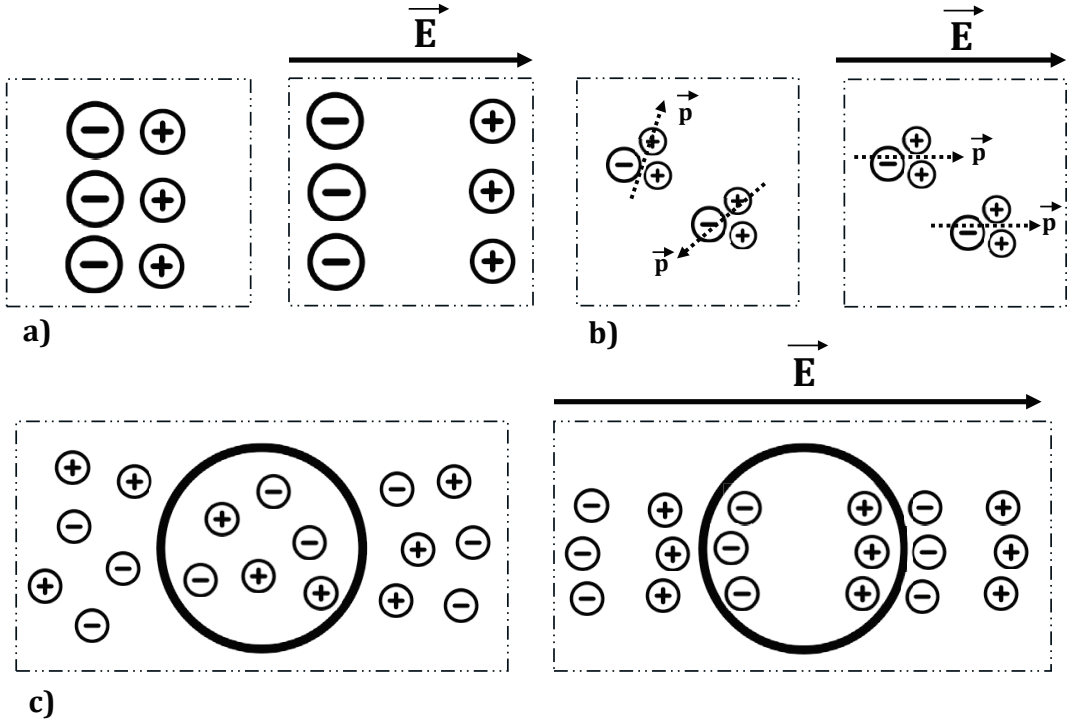

Figure 2.3: *Conceptual diagrams of some polarization effects (a) Ionic polarization displaces charges in suspension (b) Dipolar polarization rotates molecular dipoles (c) Interfacial polarization due to the accumulation of charges in a barrier as the cell membrane.*

The case of ionic polarization is due to the displacement of ions, which is very significant since this interaction generates ionic currents that also induce additional polarization effects in the surroundings [33]. Moreover, the movement of charged particles could be blocked by structural interfaces or barriers, leading to the accumulation of charges known as Interfacial polarization [34]. In contrast, dipolar polarization is due to the rotation of natural or induced molecular dipoles and mostly depends on the medium viscosity and dipole strength [35] (Figure 2.3b). Besides, temperature seriously affects this contribution since thermal energy is a key factor in the initial random dipole alignment [31].

On the other hand, electronic polarization is due to the shift of the electronic cloud in the E field direction [36], and atomic polarization is a consequence of the atom's relative displacement within a molecular structure [37] (Figure 2.4). However, atomic and electronic polarization are only possible at frequencies in the IR and Visible spectrum, respectively. Consequently, the contribution is significantly smaller than other polarizations [38]. In addition, the drift of these polarizations is opposite to the internal atom interactions, and therefore, a force acts to restore the original position, generating a resonator behavior in the atomic structure, which is characterized by a peak of permittivity at that specific resonance frequency and the electromagnetic losses [26] (Figure 2.5).

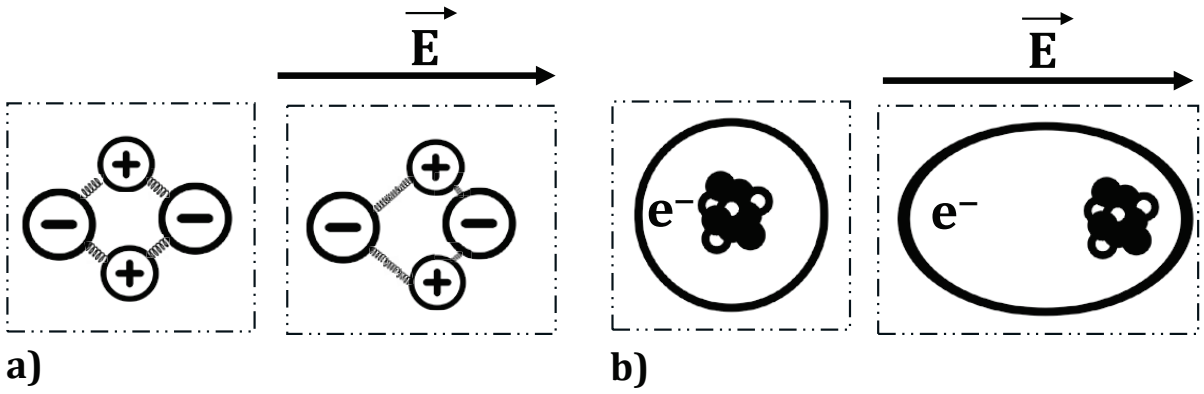

Figure 2.4: *Conceptual diagrams of distortion polarization (a) Atomic polarization displaces ions in crystalline structure (b) Electronic polarization changes the distribution of the atom electron cloud.*

Nevertheless, total polarization is highly related to the frequency of the incident field since the charges do not align instantly with the E field. Instead, they require a determined duration known as relaxation time [38]. Initially, the oriented dipoles must follow the field direction, but when this is reversed due to the nature of alternating fields, the dipoles must change again their orientation [31]. However, if the frequency is too high, demanding a faster reorientation than its relaxation time, then the charges will not follow up the E field [35]. This phenomenon is defined as dielectric relaxation (Figure 2.5) and is translated into a decrease in real permittivity called dispersion. In addition, electromagnetic losses of the sample increase during the dispersion while the polarization is failing [26]. The relaxation is complete when the incident frequency is beyond the dispersion frequency, and then electromagnetic losses are reduced to a minimum since the previous polarization contribution is too slow to initiate.

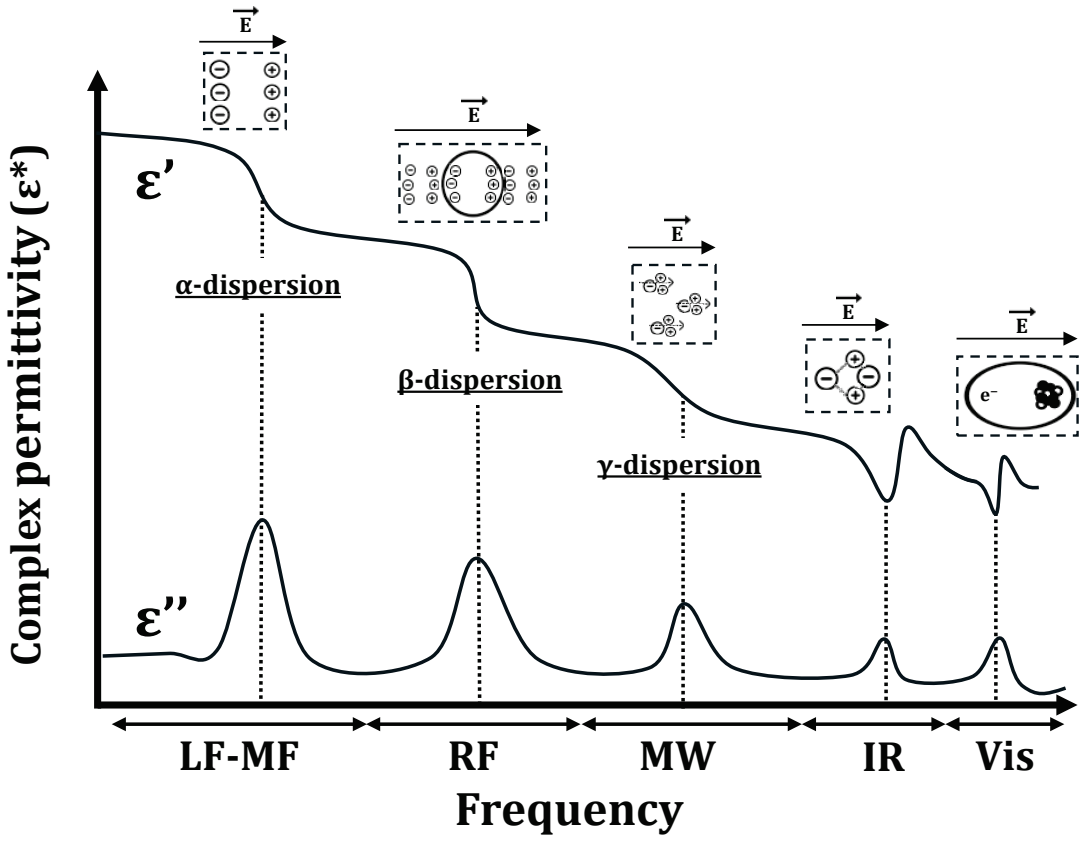

Figure 2.5: *When the frequency is increasing the dielectric relaxation is observed as a drop in the permittivity and as resonance in the loss factor.*

The effect of the EM frequency is not homogenous since some polarizations are more sensitive to the change of field direction. For example, ionic polarization is restricted to low frequencies before α-dispersion, which depends critically on the particle size and the diffusion constant [33]. Therefore, frequencies lower than α-dispersion are indicated to measure ionic concentrations in liquids. Similarly, the β-dispersion in the RF range should be considered to detect different types of cells since the interfacial relaxation is related to cellular components and membrane characteristics [34]. In contrast, the microwave (MW) region before γ-dispersion would be ideal for differentiating analytes in aqueous solutions according to dipolar relaxations [39]. Indeed, water is the ideal polar molecule with a well-defined behavior [40]. Therefore, the water dielectric signature is a perfect reference to detect dielectric variations and infer which molecules are dissolved [26]. Besides, since water is the main component of biological samples, understanding the MW range and γ-dispersion is also key to developing biosensors.

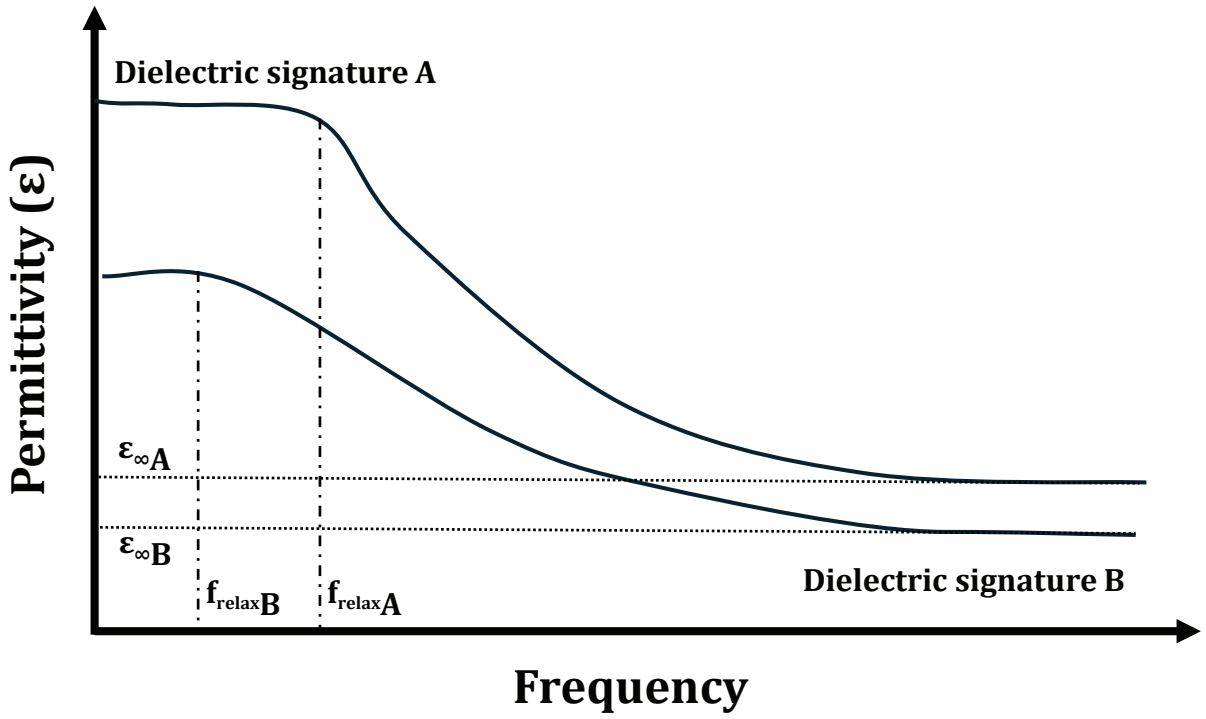

Figure 2.6: *Dielectric spectroscopy of two substances with their characteristic dielectric signatures. In this conceptual example, both samples show clear differences in the relaxation frequency* (f_{relax}) *and near optic permittivity* (ε_∞).

In summary, the relaxation behavior depends on the sample complexity since mixtures or complex molecular systems do not fit the ideal polarization shown by their single molecules [26]. Indeed, the interaction of multiple polar molecules can produce high-order polarization kinetics that can lead to specific dielectric signatures (Figure 2.5). For example, if the relaxation times of the molecular components are not well separated, then the dispersion region will be overlapped [33]. Besides, the influence of non-polar components is another factor to be considered since the permittivity of these materials is less affected by changes in frequency. Therefore, mixing substances leads to specific relaxation curves that could serve as a sensing mechanism (Figure 2.6). The main methodology to study these signals is by means of dielectric spectroscopy in a broadband frequency range [31, 32].

In the last decade, dielectric characterization has gained attention as a biosensing technique for analyzing cancerous tissues [41]. Biological matter is mostly made of water with ions and organic molecules in dissolution as well as insoluble matter; all of them form subcellular, cellular, and macroscopic structures [34]. Although dielectric spectroscopy is a common technique to characterize solid materials, its application for liquids or soft materials as biological samples is still challenging.

The open-ended probe is one of the most common methods and consists of submerging a coaxial probe into a liquid sample to record the reflection of an EM wave in a long range of frequencies [42]. Afterward, the permittivity can be estimated through the power scattering parameters and the probe-equivalent circuit. However, the accuracy and repeatability of the method are limited by experimental conditions such as probe dimensions and positioning, sample size, and frequency range [43]. Moreover, working with a wide range of frequencies requires complex and expensive electronic instrumentation, avoiding its application as a low-cost and portable sensor. These drawbacks lead to considering MW resonant sensors as an alternative approach.

2.3. Low-cost capacitive sensing with MW resonant structures

In contrast to broadband dielectric characterization, resonant methods measure changes in permittivity in a properly selected narrowband of frequencies [2]. These are more sensitive and accurate than non-resonant methods, although they do not allow a complete dielectric characterization [26]. Besides, resonant methods can be fully passive, avoiding the requirement of batteries to feed the sensor [44]. Another advantage of resonant methods (especially planar sensors) is their reduced size and cost, which simplify measuring protocols compared to other technologies [25]. Therefore, by enabling faster acquisition and reducing the sample volume, MW resonant methods are ideal alternatives to developing portable and low-cost sensors.

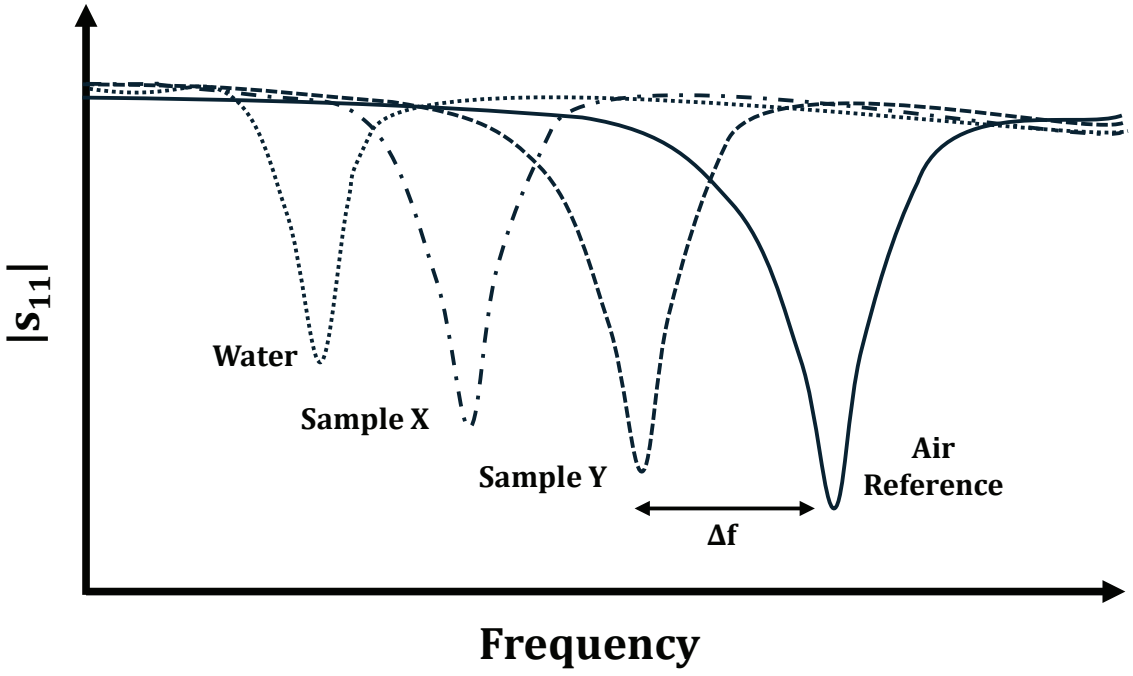

Figure 2.7: *Capacitive sensing is based on variations of the resonance frequency according to the permittivity of each sample. Besides, the loss tangent also can be inferred since it is related to the $|s_{11}|$ amplitude.*

Among resonant methods, there is a huge variety of technologies, designs, and operation modes. Independently of choice, MW resonators function as a notch filter with a high-quality factor modeled by an RLC resonant circuit [45]. The effective permittivity of the medium within the resonator near-field is

closely related to the resonator capacitance. Therefore, any medium change, such as the presence of the target sample, causes a capacitance change that is translated into a resonance frequency shift; this is the principle of capacitive sensing (Figure 2.7) [46].

Consequently, MW resonators operate as indirect detectors of any substance with a permittivity greater than the reference medium [24] (commonly air); thus, larger permittivity values would lead to larger frequency shifts. From this frequency variation framework, some modifications have been proposed, such as frequency splitting or differential-mode sensors that could lead to more specific applications [25].

The basic design of a planar MW resonant sensor consists of a microstrip transmission line loaded with a resonant element that can be either metallic or a slot etched to the ground plane [25]. Instead of an isolated resonator, the sensor performance can be improved through a symmetric configuration of several resonators [47]. Planar sensors allow high design flexibility due to the number of resonator topologies and dimensions that can employed (Figure 2.8) [26]. The resonance frequency depends on these parameters, and therefore, the sensor can be tuned to work for different applications at the desired narrowband [48]. For example, Split Ring Resonator (SRR) sensors are one of the most popular designs due to their small electrical dimensions [49, 50].

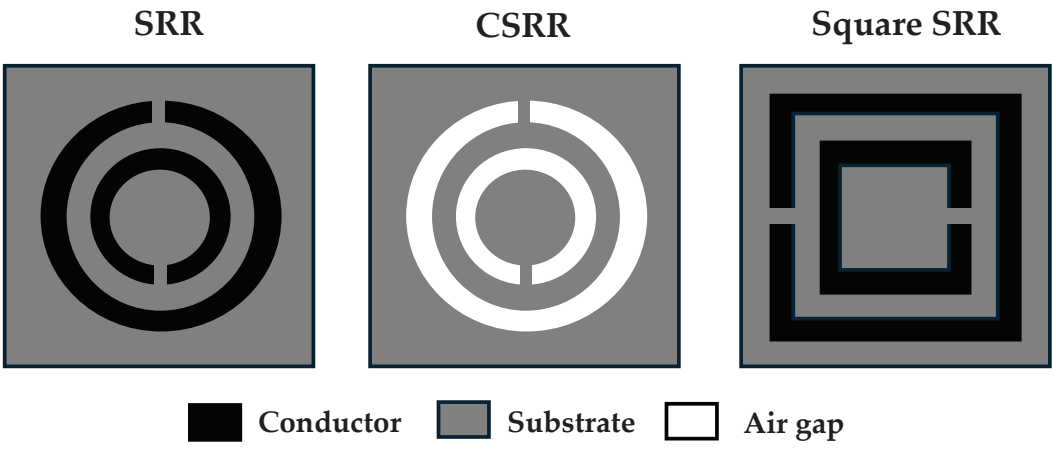

Figure 2.8: *Common topologies for MW resonant sensors.*

Planar sensors have been extensively applied for the dielectric characterization of thin layers of material [51, 52]. Besides, they can be applied for detecting analytes in liquids in combination with a microfluidic configuration but at the cost of increasing the complexity of the device [53]. Nevertheless, it must be noted that the sensing depth is limited since the EM field is confined just in the near space. In contrast, resonant cavity sensors are based on closed metallic structures able to achieve a strong confined electric field within a volume [2]. These methods are especially accurate and suitable for low-loss materials. However, the main drawback lies in the complex and expensive design and fabrication. As an alternative, resonant cavity sensors based on Dielectric Resonator (DR) have gained attention in recent years. These resonators made of low-loss dielectric materials, commonly used for microwave components, could satisfy the requirements of small portable devices for the Internet-of-Things applications [54]. Indeed, DRs are an ideal radiating device for high frequencies with minimum conduction losses and high radiation efficiency [55]. For this reason, several articles have explored the possibility of using DR for developing MW sensing devices [56, 57].

One of the main advantages of DR sensors is their easier and more flexible fabrication process since they generally consist of a bulk material with regular geometry. As well as planar sensors, the DR resonance behavior in a narrow band of frequencies is determined by the physical dimensions. Therefore, this geometrical flexibility can be modeled with analytical equations or different numerical methods to fit specific resonance frequency and/or impedance bandwidth [58]. Cylindrical DR is the most common device found in the literature due to its fabrication feasibility. The height and radius are the geometrical parameters to tune the resonance frequency (Figure 2.9 a-b); both are inversely proportional to the frequency. Consequently, these devices are very promising for MW sensing since their design can adapt to the target with a simple change of geometry. Moreover, the design flexibility provides numerous options, in-

cluding defining a larger or shorter range of sensing, fitting the impedance bandwidth to measure a smaller range of permittivity, and applying different types of feeding structures to excite different propagation modes [55].

Another relevant tuning parameter is the permittivity of the DR material (Figure 2.9 c) [59]. The most common materials for DR are oxide ceramics whose permittivity depends on the crystal chemistry and sintering process, including the starting powder purity, density, and heating/cooling mechanism [54]. However, if low permittivity is needed for a specific application, commercial polymers can be used for DR alone or in a ceramic composite [60]. This would allow the fabrication of MW sensors through 3D-printing techniques [61].

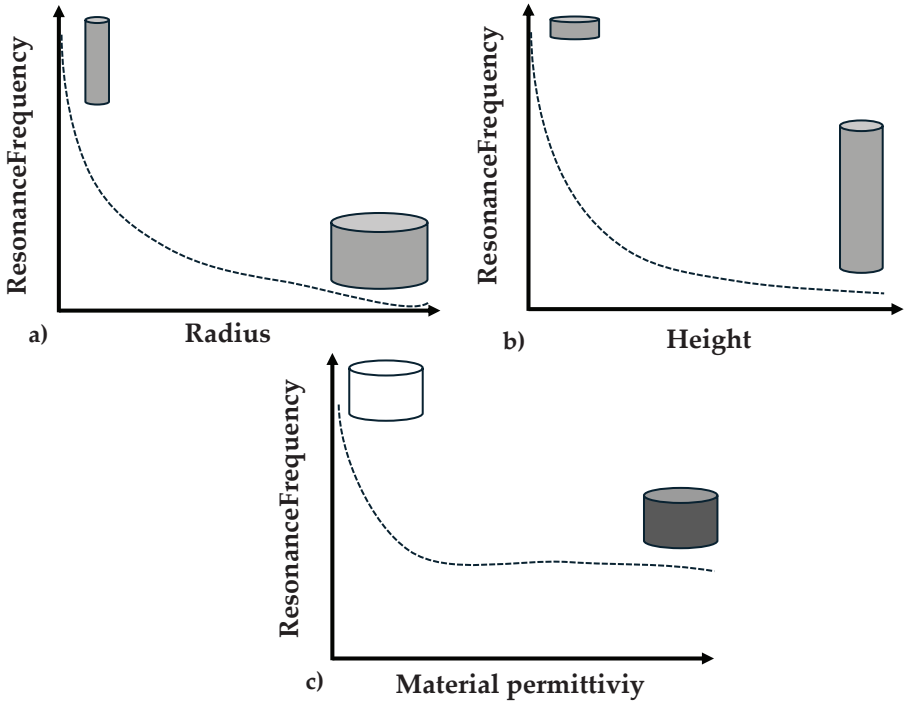

Figure 2.9: *Resonance frequency variation as a function of (a) DRA radius, (b) DRA height (c) DRA dielectric constant.*

In summary, RF-MW resonant sensors are a promising technology for characterizing and classifying substances due to their cost-effectiveness, low complexity, and versatility. Nevertheless, this technology lacks specificity, hindering the result interpretation and accuracy for complex applications with many analytes involved. This PhD proposes applying Machine Learning techniques to enhance the performance of this technology.

2.4. Enhancing sensor performance with Machine Learning

Artificial intelligence (AI) is the science that aims to develop computer systems able to perform tasks only doable by human intelligence [62]. Machine Learning (ML) is a subfield of AI focused on identifying complex patterns from data and thereby generalizing that knowledge to make predictions [63] (Figure 2.12). There is a multitude of ML algorithms grouped into two main styles of learning: supervised learning and unsupervised learning (Figure 2.10). In the first case, the model has prior knowledge about the target values; thus, the ML algorithm is trained with multiple examples in order to find the optimal function that best captures the relationship between the inputs and the target variable [64]. Whereas unsupervised learning does not have this information; instead, the model tries to infer the natural data structure for automatic class clustering [65] or feature extraction [66].

In comparison with linear regression models [67], ML models represent a non-parametric approach to resolving an optimization problem fitting the model architecture to the data. In a parametric model, there is a fixed number of parameters, and the optimization involves finding the best values for these parameters [68]. However, finding an effective parametric model can be challenging for non-linear relationships, especially with many features or independent variables, such as signal analysis problems [69]. For example, a parametric model with a limited number of features (such as resonance frequency in MW sensors) could be hindered since these parameters may not represent complete signal information; thus, it may introduce bias or variance, reducing the sensor's accuracy. In contrast, non-parametric ML models adjust their complexity and parameters according to the training data [70]. This adaptability allows ML models to automatically navigate more complex feature spaces by learning from the data structure. Moreover, ML training can be oriented to find a proper trade-off between variance and bias, applying complementary methods to avoid overfitting, such as Cross-Validation [71].

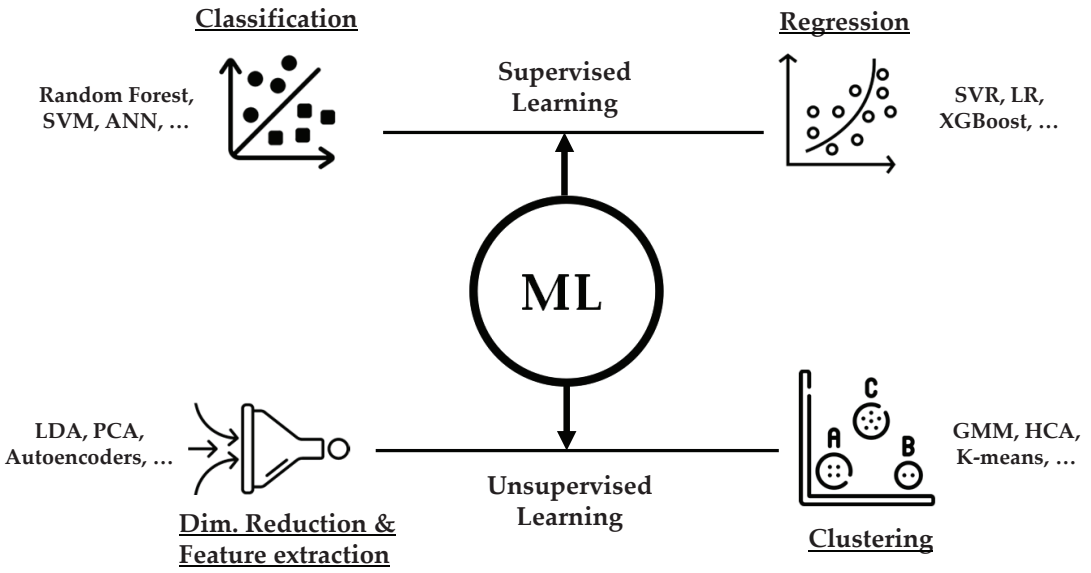

Figure 2.10: *Classification of ML models according to the main types of learning and its corresponding tasks.*

Improving sensor calibration is the main contribution of ML models for sensing applications, which is an essential task to achieve accurate and useful results [72]. The aim of calibration is to solve the basic analytical problem that the sensor signal (Figure 2.1) is not a direct measure of the target variable, and therefore, it must be transformed to give an analytical result [73]. Indeed, according to the IUPAC, calibration is the set of operations that determine or approximate the relationship between the sensor response and the expected measured value [74]. Calibrations can follow a model-driven approach based on the theoretical knowledge of the sensing element [75] or an empirical approach that adjusts the sensor response to fit known standard samples [73]. Nevertheless, both approaches present several limitations, a non-linear relationship between the analyzed process and the signal acquired [76].

In contrast, the data-driven approach is based on statistical methods and requires compiling a representative dataset of measures and selecting relevant features [75]. ML learning can be applied as the core of this approach, replacing other methods such as linear regression [76]. Thus, the calibration task to estimate analytical results correctly, concerning either the type or amount of a target variable, is equivalent to a regression or classification problem that

can be resolved by applying supervised ML [77]. Indeed, these type models (Figure 2.10) are the most appropriate solution for enhancing sensor accuracy since researchers know a priori which substance is under test and some of its characteristics. Whereas unsupervised methods such as clustering could be applied for exploratory analysis to group similar signals within an unknown sensing environment [75].

Another objective of calibration is to mitigate the effect of errors due to ambient or device imperfections [78]. This problem is especially relevant for the data collected by low-cost sensors that could be noisy or with a low resolution where the analyte information could be partially hidden and difficult to analyze [76]. Precisely, finding hidden correlations within the data is the main strength of ML models, and there lies their potential to enhance sensor performance [17]. Consequently, since the last decade, the potential of ML has been developed for numerous applications, and recently, ML models have been proposed as a powerful technology to improve (bio)sensors performance [79, 80, 81]. In particular, Feiyun Cui et al. provided a detailed review of recent ML model applications for both electrochemical and optical biosensors, analyzing the significant accuracy improvement [79]. More reviews, such as Kenneth E. et al. for label-free biosensors [77] or Singh et al. for electrochemical biosensors [17], reached the same conclusions.

However, in these reviews, there is a clear absence of RF-MW resonant sensors, which should be underlined as a research opportunity. In fact, other EM sensors were included, mainly Surface Enhanced Raman Scattering (SERS) and Surface Plasmon Resonance (SPR). Their results suggest that the combination of Principal Component Analysis (PCA) and Support Vector Machine (SVM) tends to have positive results with spectral data. Another possibility presented is the use of Convolutional Networks or Deep Neural Networks, but they require more complex programming and computational costs to obtain similar results. In any case, finding the best model architecture depends on the

sensing technology and each particular application. These positive insights are reflected in Figure 2.11, which displays how the attention toward ML models for (bio)sensors is increasing in the scientific community.

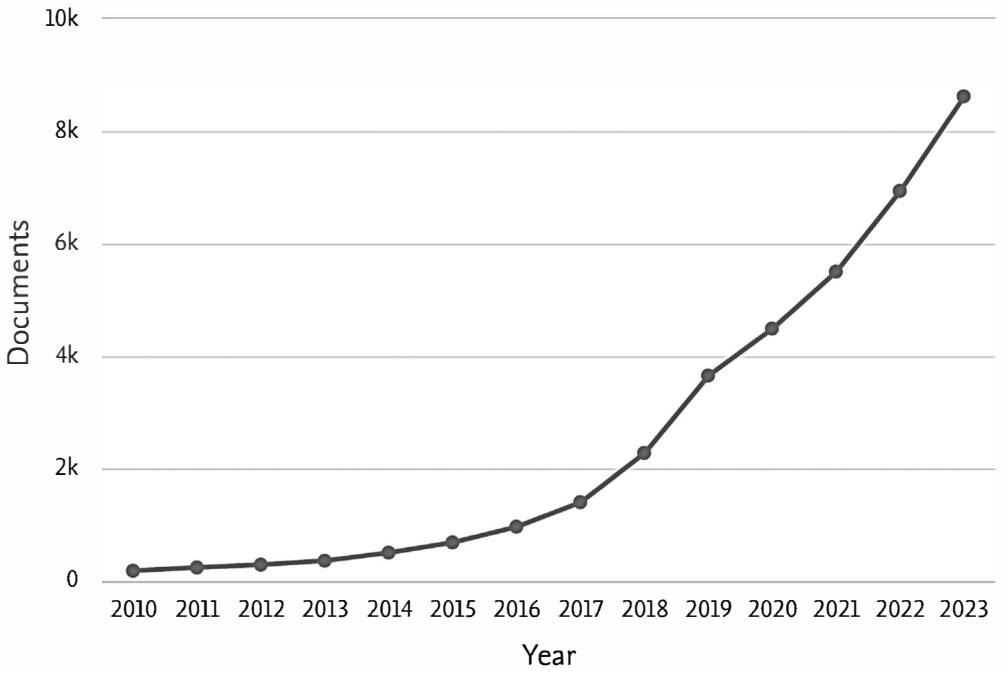

Figure 2.11: *Number of publications as the result form the search in Scopus for "Machine Learning" + "sensors".*

This exponential growth can be explained by considering that the advantages of combining sensor devices and ML models are not limited to improving calibration or sensor accuracy. Beyond signal analysis, ML workflow facilitates working with a large volume of data [79], complex data structures [82] and sensor networks [76]. Besides, the ML model's strength to detect and classify patterns can be employed for automatic anomaly detection in the case of sensor malfunction [83]. Moreover, ML models could be applied even before the sensor is fabricated by helping in the design to find optimized sensors [29]. Finally, one of the most promising applications is the generation of realistic synthetic data through Deep Learning techniques in order to build, enlarge, and improve datasets with fewer experiments and less economic cost [84].

2.5. Deep Learning for Data Augmentation

There are many definitions of Deep Learning (DL), but all of them concur that DL is based on the composition of several neural network layers able to automatically discover the intricate relationships within large datasets through multiple levels of representation [85]. Each architecture layer is a simple but non-linear module transforming the input at a higher abstract level; thus, the number of layers and the model complexity can be tuned according to the learning task [86]. Compared with traditional ML models, DL architectures can be fed with raw data such as images or sensor signals without applying any preprocessing to extract the relevant features and/or reduce its dimensionality. During the last decade, DL models have been applied in many areas, including natural language processing and computer vision [87]. Consequently, a vast selection of DL architectures have been developed following different learning approaches, which are continuously improving [88].

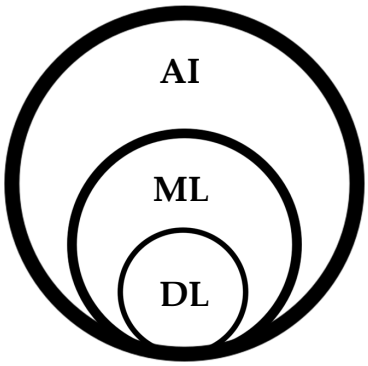

Figure 2.12: *Hierarchy of AI disciplines.*

Nevertheless, despite the recent advances, the dataset quality remains as the main condition to achieve a good learning performance. Dataset size and representativeness are critical factors that cannot be completely ensured for many applications [89]. Therefore, Data Augmentation (DA) techniques aim to improve small, imbalanced, or poorly diverse datasets by generating new samples [90]. For example, to enhance image datasets, the traditional methods consist of transformation operations over a subset of the original images, such

as mirroring or rotating, achieving optimal results for image classification or computer vision [91]. In contrast, the performance of transformative DA techniques for time series and sequential data, including sensor signals, is insufficient since the information within the original data distribution depends on the element order [92]. Therefore, techniques such as noise addition, time delay, or cut and paste can have a destructive effect on relevant features [90]. For example, Rahman et al., in a systematic review of DA techniques for electrocardiogram (ECG) signals, conclude that transformative DA tends to modify ECG features, increasing the noise in the augmented dataset [93]. Therefore, the best alternative is to generate synthetic samples, which preserves the statistical properties from the original dataset. Until recently, the main approaches for Synthetic Data Generation (SDG) were statistical algorithms or models based on domain expert knowledge [94]. However, nowadays Deep Generative Models (DGM) stand out as the most popular alternative [95]. Indeed, beyond class classification or forecasting tasks commonly performed by ML models, the abstract representation achieved by DL architectures allows more complex tasks, such as the generation of synthetic data based on the characteristics learned in the original dataset [96].

Several studies have shown the potential of DGM for the generation of sequential data. For example, Hennesy et al. used Generative Adversarial Networks (GAN) for synthetic hyperspectral vegetation data [97], while Demir et al. compared several architectures for the generation of electricity price signals [98]. In addition, deep synthetic data can ensure the privacy of sensitive information, since there is not a direct transformation from original data; this is the key to satisfy the ethical framework for using medical data in DL models. Consequently, DGMs are perfect to generate synthetic health records [99]. Likewise, many studies show that sensing devices for health applications would benefit from the privacy condition. For instance, Ehrhart et al. proposed a Conditional-GAN to enhance the signal dataset acquired by a wearable phy-

siological sensor for stress recognition [100], whereas Chang et al. suggested a Wasserstein GAN to generate synthetic pulse signals with relevant cardiovascular information [101].

Despite the promising results, the design and training of DGM is still challenging, and requires a further understanding on why a particular architecture is successful or not learning a particular data structure [96]. In order to resolve this problem, exploring the resultant latent space of these models is a critical task to control the generation of synthetic samples [102].

BIBLIOGRAPHY

[1] E. Hering, *Sensor Systems*, ch. 1, pp. 1–3. Wiesbaden: Springer Fachmedien Wiesbaden, 2022.

[2] F. Martin, P. Velez, J. Munoz-Enano, and L. Su, *Introduction to Planar Microwave Sensors*, ch. 1, pp. 1–64. Wiley-IEEE Press, 2023.

[3] R. Pallás-Areny and J. G. Webster, *Sensors and signal conditioning*. Wiley, 2001.

[4] B. W. An, J. H. Shin, S.-Y. Kim, J. Kim, S. Ji, J. Park, Y. Lee, J. Jang, Y.-G. Park, E. Cho, S. Jo, and J.-U. Park, "Smart sensor systems for wearable electronic devices," *Polymers*, vol. 9, no. 8, 2017.

[5] R. Narayan, *Encyclopedia of Sensors and Biosensors: Volume 1, First Edition*, vol. 1. Elsevier, 2022.

[6] J. Fraden, *Handbook of modern sensors: Physics, designs, and applications*. Springer International Publishing, 2016.

[7] J. S. Wilson, *Sensor technology handbook*, vol. 1. Newnes, 2005.

[8] R. Bogue, "Sensors for interfacing with consumer electronics," *Sensor Review*, vol. 31, no. 2, p. 106 – 110, 2011.

[9] B. Pradhan, S. Bhattacharyya, and K. Pal, "Iot-based applications in healthcare devices," *Journal of Healthcare Engineering*, vol. 2021, 2021.

[10] K. Chan, D. N. Schillereff, A. C. Baas, M. A. Chadwick, B. Main, M. Mulligan, F. T. O'Shea, R. Pearce, T. E. Smith, A. van Soesbergen, E. Tebbs, and J. Thompson, "Low-cost electronic sensors for environmental research: Pitfalls and opportunities," *Progress in Physical Geography: Earth and Environment*, vol. 45, no. 3, pp. 305–338, 2021.

[11] L. García, L. Parra, J. M. Jimenez, J. Lloret, and P. Lorenz, "Iot-based smart irrigation systems: An overview on the recent trends on sensors and iot systems for irrigation in precision agriculture," *Sensors (Switzerland)*, vol. 20, no. 4, 2020.

[12] K. K. Iniewski, *Smart sensors for industrial applications*. CRC Press, 2017.

[13] Y. Khan, A. E. Ostfeld, C. M. Lochner, A. Pierre, and A. C. Arias, "Monitoring of vital signs with flexible and wearable medical devices," *Advanced Materials*, vol. 28, no. 22, p. 4373 – 4395, 2016.

[14] S. Nayak, N. R. Blumenfeld, T. Laksanasopin, and S. K. Sia, "Point-of-care diagnostics: Recent developments in a connected age," *Analytical Chemistry*, vol. 89, no. 1, p. 102 – 123, 2017.

[15] R. Kobun, ed., *Biosensor technology to detect chemical contamination in food*, ch. 7, pp. 127–146. Academic Press, 2021.

[16] P. Mehrotra, "Biosensors and their applications - a review," *Journal of Oral Biology and Craniofacial Research*, vol. 6, no. 2, p. 153 – 159, 2016.

[17] A. Singh, A. Sharma, A. Ahmed, A. K. Sundramoorthy, H. Furukawa, S. Arya, and A. Khosla, "Recent advances in electrochemical biosensors: Applications, challenges, and future scope," *Biosensors*, vol. 11, no. 9, 2021.

[18] J. Wang, "Electrochemical glucose biosensors," *Chemical Reviews*, vol. 108, no. 2, p. 814 – 825, 2008.

[19] F. A. Mota, M. L. Passos, J. L. Santos, and M. M. Saraiva, "Comparative analysis of electrochemical and optical sensors for detection of chronic wounds biomarkers: A review," *Biosensors and Bioelectronics*, vol. 251, 2024.

[20] S. Campuzano, M. Pedrero, M. Gamella, V. Serafín, P. Yáñez-Sedeño, and J. M. Pingarrón, "Beyond sensitive and selective electrochemical biosensors: Towards continuous, real-time, antibiofouling and calibration-free devices," *Sensors (Switzerland)*, vol. 20, no. 12, p. 1 – 22, 2020.

[21] M. M. Shanbhag, G. Manasa, R. J. Mascarenhas, K. Mondal, and N. P. Shetti, "Fundamentals of bio-electrochemical sensing," *Chemical Engineering Journal Advances*, vol. 16, 2023.

[22] S. R. S. Pour, D. Calabria, A. Emamiamin, E. Lazzarini, A. Pace, M. Guardigli, M. Zangheri, and M. Mirasoli, "Electrochemical vs. optical biosensors for point-of-care applications: A critical review," *Chemosensors*, vol. 11, no. 10, 2023.

[23] C. Chen and J. Wang, "Optical biosensors: An exhaustive and comprehensive review," *Analyst*, vol. 145, no. 5, p. 1605 – 1628, 2020.

[24] M. G. Mayani, F. J. Herraiz-Martínez, J. M. Domingo, and R. Giannetti, "Resonator-based microwave metamaterial sensors for instrumentation: Survey, classification, and performance comparison," *IEEE Transactions on Instrumentation and Measurement*, vol. 70, pp. 1–14, 2021.

[25] J. Muñoz-Enano, P. Vélez, M. Gil, and F. Martín, "Planar microwave resonant sensors: A review and recent developments," *Applied Sciences*, vol. 10, no. 7, 2020.

[26] P. Mehrotra, B. Chatterjee, and S. Sen, "Em-wave biosensors: A review of rf, microwave, mm-wave and optical sensing," *Sensors (Switzerland)*, vol. 19, no. 5, 2019.

[27] M. Velasco-Garcia, "Optical biosensors for probing at the cellular level: A review of recent progress and future prospects," *Seminars in Cell and Developmental Biology*, vol. 20, no. 1, p. 27 – 33, 2009.

[28] K. P. Carter, A. M. Young, and A. E. Palmer, "Fluorescent sensors for measuring metal ions in living systems," *Chemical Reviews*, vol. 114, no. 8, p. 4564 – 4601, 2014.

[29] P. Li, F. Long, W. Chen, J. Chen, P. K. Chu, and H. Wang, "Fundamentals and applications of surface-enhanced raman spectroscopy–based biosensors," *Current Opinion in Biomedical Engineering*, vol. 13, p. 51 – 59, 2020.

[30] J.-F. Masson, "Surface plasmon resonance clinical biosensors for medical diagnostics," *ACS Sensors*, vol. 2, no. 1, p. 16 – 30, 2017.

[31] K. Deshmukh, S. Sankaran, B. Ahamed, K. K. Sadasivuni, K. S. Pasha, D. Ponnamma, P. Rama Sreekanth, and K. Chidambaram, *Dielectric Spectroscopy*, ch. 10, pp. 237–299. Micro and Nano Technologies, Elsevier, 2017.

[32] F. Artis, T. Chen, T. Chretiennot, J.-J. Fournie, M. Poupot, D. Dubuc, and K. Grenier, "Microwaving biological cells: Intracellular analysis with microwave dielectric spectroscopy," *IEEE Microwave Magazine*, vol. 16, no. 4, pp. 87–96, 2015.

[33] C. Gabriel and A. Peyman, "Electric and magnetic properties of biological materials," in *Bioengineering and Biophysical Aspects of Electromagnetic Fields, Fourth Edition*, ch. 4, pp. 101–159, CRC Press, 2018.

[34] K. Heileman, J. Daoud, and M. Tabrizian, "Dielectric spectroscopy as a viable biosensing tool for cell and tissue characterization and analysis," *Biosensors and Bioelectronics*, vol. 49, pp. 348–359, 2013.

[35] R. Blakey and A. Morales-Partera, "Microwave dielectric spectroscopy," *Engineering in Agriculture, Environment and Food*, vol. 9, no. 3, pp. 264–273, 2016.

[36] E. Duboué-Dijon, M. Javanainen, P. Delcroix, P. Jungwirth, and H. Martinez-Seara, "A practical guide to biologically relevant molecular simulations with charge scaling for electronic polarization," *Journal of Chemical Physics*, vol. 153, no. 5, 2020.

[37] J. Mitroy, M. Safronova, and C. W. Clark, "Theory and applications of atomic and ionic polarizabilities," *Journal of Physics B: Atomic, Molecular and Optical Physics*, vol. 43, no. 20, 2010.

[38] T. Dakin, "Conduction and polarization mechanisms and trends in dielectric," *IEEE Electrical Insulation Magazine*, vol. 22, no. 5, pp. 11–28, 2006.

[39] C. Grosse and A. Delgado, "Dielectric dispersion in aqueous colloidal systems," *Current Opinion in Colloid & Interface Science*, vol. 15, no. 3, pp. 145–159, 2010.

[40] R. Buchner, G. T. Hefter, and P. M. May, "Dielectric relaxation of aqueous nacl solutions," *Journal of Physical Chemistry A*, vol. 103, no. 1, p. 8 – 9, 1999.

[41] H. M. Fahmy, A. M. Hamad, F. A.-z. Sayed, Y. S. Abdelaziz, E. S. Abu Serea, A. B. E.-D. Mustafa, M. A. Mohammed, and A. M. Saadeldin, "Dielectric spectroscopy signature for cancer diagnosis: A review," *Microwave and Optical Technology Letters*, vol. 62, no. 12, pp. 3739–3753, 2020.

[42] M. A. Stuchly and S. S. Stuchly, "Coaxial line reflection methods for measuring dielectric properties of biological substances at radio and microwave frequencies-a review," *IEEE Transactions on Instrumentation and Measurement*, vol. 29, no. 3, pp. 176–183, 1980.

[43] M. Cavagnaro and G. Ruvio, "Numerical sensitivity analysis for dielectric characterization of biological samples by open-ended probe technique," *Sensors*, vol. 20, no. 13, 2020.

[44] S. Kananian, G. Alexopoulos, and A. Poon, *Coupling-Independent Sensing Systems with Fully Passive Sensors*, ch. 13, pp. 469–521. John Wiley & Sons, Ltd, 2021.

[45] D. Pozar, *Microwave resonators*, ch. 6. Wiley, 2021.

[46] F. Martin, P. Velez, J. Munoz-Enano, and L. Su, *Frequency-Variation Sensors*, pp. 65–118. Wiley-IEEE Press, 2023.

[47] M. Durán-Sindreu, J. Naqui, F. Paredes, J. Bonache, and F. Martín, "Electrically small resonators for planar metamaterial, microwave circuit and antenna design: A comparative analysis," *Applied Sciences*, vol. 2, no. 2, pp. 375–395, 2012.

[48] D. Prakash and N. Gupta, "Applications of metamaterial sensors: a review," *International Journal of Microwave and Wireless Technologies*, vol. 14, no. 1, p. 19 – 33, 2022.

[49] Rajni and A. Marwaha, "An accurate approach of mathematical modeling of srr and sr for metamaterials," *Journal of Engineering Science and Technology Review*, vol. 9, pp. 82–86, 2016.

[50] R. A. Alahnomi, Z. Zakaria, Z. M. Yussof, A. A. Althuwayb, A. Alhegazi, H. Alsariera, and N. A. Rahman, "Review of recent microwave planar resonator-based sensors: Techniques of complex permittivity extraction, applications, open challenges and future research directions," *Sensors*, vol. 21, no. 7, 2021.

[51] A. Vivek, K. Shambavi, and Z. C. Alex, "A review: metamaterial sensors for material characterization," *Sensor Review*, vol. 39, no. 3, p. 417 – 432, 2019.

[52] G. Galindo-Romera, F. Javier Herraiz-Martínez, M. Gil, J. J. Martínez-Martínez, and D. Segovia-Vargas, "Submersible printed split-ring resonator-based sensor for thin-film detection and permittivity characterization," *IEEE Sensors Journal*, vol. 16, no. 10, pp. 3587–3596, 2016.

[53] M. H. Zarifi, H. Sadabadi, S. H. Hejazi, M. Daneshmand, and A. Sanati-Nezhad, "Non-contact and nonintrusive microwave-microfluidic flow sensor for energy and biomedical engineering," *Scientific Reports*, vol. 8, no. 1, 2018.

[54] M. Sebastian, R. Ubic, and H. Jantunen, "Low-loss dielectric ceramic materials and their properties," *International Materials Reviews*, vol. 60, no. 7, p. 392 – 412, 2015.

[55] S. K. K. Dash, T. Khan, and Y. M. M. Antar, "A state-of-art review on performance improvement of dielectric resonator antennas," *International Journal of RF and Microwave Computer-Aided Engineering*, vol. 28, no. 6, 2018.

[56] A. Iqbal, A. Smida, O. A. Saraereh, Q. H. Alsafasfeh, N. K. Mallat, and B. M. Lee, "Cylindrical dielectric resonator antenna-based sensors for liquid chemical detection," *Sensors*, vol. 19, no. 5, 2019.

[57] M. G. Mayani, F. J. Herraiz-Martinez, J. M. Domingo, R. Giannetti, and C. R.-M. Garcia, "A novel dielectric resonator-based passive sensor for drop-volume binary mixtures classification," *IEEE Sensors Journal*, vol. 21, no. 18, p. 20156 – 20164, 2021.

[58] S. K. K. Dash, T. Khan, and A. De, "Modelling of dielectric resonator antennas using numerical methods: a review," *Journal of Microwave Power and Electromagnetic Energy*, vol. 50, no. 4, p. 269 – 293, 2016.

[59] S. Keyrouz and D. Caratelli, "Dielectric resonator antennas: Basic concepts, design guidelines, and recent developments at millimeter-wave frequencies," *International Journal of Antennas and Propagation*, vol. 2016, 2016.

[60] M. T. Sebastian and H. Jantunen, "Polymer–ceramic composites of 0–3 connectivity for circuits in electronics: A review," *International Journal of Applied Ceramic Technology*, vol. 7, no. 4, pp. 415–434, 2010.

[61] J. Ren and J. Y. Yin, "3d-printed low-cost dielectric-resonator-based ultra-broadband microwave absorber using carbon-loaded acrylonitrile butadiene styrene polymer," *Materials*, vol. 10, no. 7, 2018.

[62] W. Samek and K.-R. Müller, "Towards explainable artificial intelligence," *Lecture Notes in Computer Science (including subseries Lecture Notes in Artificial Intelligence and Lecture Notes in Bioinformatics)*, vol. 11700 LNCS, p. 5 – 22, 2019.

[63] K. P. Murphy, *Probabilistic Machine Learning: Advanced Topics*. MIT Press, 2023.

[64] A. E. Maxwell, T. A. Warner, and F. Fang, "Implementation of machine-learning classification in remote sensing: An applied review," *International Journal of Remote Sensing*, vol. 39, no. 9, p. 2784 – 2817, 2018.

[65] A. O. Ige and M. H. Mohd Noor, "A survey on unsupervised learning for wearable sensor-based activity recognition," *Applied Soft Computing*, vol. 127, p. 109363, 2022.

[66] A. Glielmo, B. E. Husic, A. Rodriguez, C. Clementi, F. Noé, and A. Laio, "Unsupervised learning methods for molecular simulation data," *Chemical Reviews*, vol. 121, no. 16, p. 9722 – 9758, 2021.

[67] N. Altman and M. Krzywinski, "Points of significance: Simple linear regression," *Nature Methods*, vol. 12, no. 11, p. 999 – 1000, 2015.

[68] M. I. Jordan and T. M. Mitchell, "Machine learning: Trends, perspectives, and prospects," *Science*, vol. 349, no. 6245, pp. 255–260, 2015.

[69] R. Jain, B. Jain, and M. Puri, *Learning Theory (Supervised/Unsupervised) for Signal Processing*, ch. 2, pp. 17–53. Chapman and Hall/CRC, 1st ed., 2021.

[70] Z. Ghahramani, "Probabilistic machine learning and artificial intelligence," *Nature*, vol. 521, no. 7553, p. 452 – 459, 2015.

[71] G. C. Cawley and N. L. Talbot, "On over-fitting in model selection and subsequent selection bias in performance evaluation," *The Journal of Machine Learning Research*, vol. 11, p. 2079–2107, 2010.

[72] Q. "Ma and G. S. Chirikjian, *"Sensor Calibration, Modeling, and Simulation"*, pp. "2007–2042". "Springer Netherlands", "2019".

[73] P. Kościelniak, *Calibration Fundamentals*, ch. 1, pp. 1–24. John Wiley & Sons, Ltd, 2023.

[74] K. Danzer and L. A. Currie, "Guidelines for calibration in analytical chemistry. part i. fundamentals and single component calibration (iupac recommendations 1998)," *Pure and Applied Chemistry*, vol. 70, no. 4, p. 993–1014, 1998.

[75] V. Shirmohammadli and B. Bahreyni, "Machine learning for sensing applications: A tutorial," *IEEE Sensors Journal*, vol. 22, no. 11, pp. 10183–10195, 2022.

[76] N. Zimmerman, A. A. Presto, S. P. N. Kumar, J. Gu, A. Hauryliuk, E. S. Robinson, and A. L. Robinson, "A machine learning calibration model using random forests to improve sensor performance for lower-cost air quality monitoring," *Atmospheric Measurement Techniques*, vol. 11, no. 1, p. 291–313, 2018.

[77] K. E. Schackart and J.-Y. Yoon, "Machine learning enhances the performance of bioreceptor-free biosensors," *Sensors*, vol. 21, no. 16, 2021.

[78] S. Koziel, A. Pietrenko-Dabrowska, M. Wojcikowski, and B. Pankiewicz, "Efficient calibration of cost-efficient particulate matter sensors using machine learning and time-series alignment," *Knowledge-Based Systems*, vol. 295, p. 111879, 2024.

[79] F. Cui, Y. Yue, Y. Zhang, Z. Zhang, and H. S. Zhou, "Advancing biosensors with machine learning," *ACS Sensors*, vol. 5, no. 11, p. 3346 – 3364, 2020.

[80] X. Jin, C. Liu, T. Xu, L. Su, and X. Zhang, "Artificial intelligence biosensors: Challenges and prospects," *Biosensors and Bioelectronics*, vol. 165, p. 112412, 2020.

[81] Y. Mekonnen, S. Namuduri, L. Burton, A. Sarwat, and S. Bhansali, "Review - machine learning techniques in wireless sensor network based precision agriculture," *Journal of the Electrochemical Society*, vol. 167, no. 3, 2020.

[82] E. Blasch, T. Pham, C.-Y. Chong, W. Koch, H. Leung, D. Braines, and T. Abdelzaher, "Machine learning/artificial intelligence for sensor data fusion-opportunities and challenges," *IEEE Aerospace and Electronic Systems Magazine*, vol. 36, no. 7, p. 80 – 93, 2021.

[83] X. Xu, H. Liu, and M. Yao, "Recent progress of anomaly detection," *Complexity*, vol. 2019, 2019.

[84] N. Patki, R. Wedge, and K. Veeramachaneni, "The synthetic data vault," p. 399 – 410, 2016.

[85] Y. Lecun, Y. Bengio, and G. Hinton, "Deep learning," *Nature*, vol. 521, no. 7553, p. 436 – 444, 2015.

[86] Y. Bengio, A. Courville, and P. Vincent, "Representation learning: A review and new perspectives," *IEEE Transactions on Pattern Analysis and Machine Intelligence*, vol. 35, no. 8, pp. 1798–1828, 2013.

[87] S. Dong, P. Wang, and K. Abbas, "A survey on deep learning and its applications," *Computer Science Review*, vol. 40, p. 100379, 2021.

[88] M. Z. Alom, T. M. Taha, C. Yakopcic, S. Westberg, P. Sidike, M. S. Nasrin, M. Hasan, B. C. Van Essen, A. A. S. Awwal, and V. K. Asari, "A state-of-the-art survey on deep learning theory and architectures," *Electronics (Switzerland)*, vol. 8, no. 3, 2019.

[89] A. Mumuni and F. Mumuni, "Data augmentation: A comprehensive survey of modern approaches," *Array*, vol. 16, p. 100258, 2022.

[90] B. K. Iwana and S. Uchida, "An empirical survey of data augmentation for time series classification with neural networks," *PLOS ONE*, vol. 16, pp. 1–32, 07 2021.

[91] C. Shorten and T. M. Khoshgoftaar, "A survey on image data augmentation for deep learning," *Journal of Big Data*, vol. 6, no. 1, 2019.

[92] Q. Wen, L. Sun, X. Song, J. Gao, X. Wang, and H. Xu, "Time series data augmentation for deep learning: A survey," *CoRR*, vol. abs/2002.12478, 2020.

[93] M. M. Rahman, M. W. Rivolta, F. Badilini, and R. Sassi, "A systematic survey of data augmentation of ecg signals for ai applications," *Sensors*, vol. 23, no. 11, 2023.

[94] A. Figueira and B. Vaz, "Survey on synthetic data generation, evaluation methods and gans," *Mathematics*, vol. 10, no. 15, 2022.

[95] P. Eigenschink, T. Reutterer, S. Vamosi, R. Vamosi, C. Sun, and K. Kalcher, "Deep generative models for synthetic data: A survey," *IEEE Access*, vol. 11, pp. 47304–47320, 2023.

[96] L. Ruthotto and E. Haber, "An introduction to deep generative modeling," *GAMM-Mitteilungen*, vol. 44, no. 2, p. e202100008, 2021.

[97] A. Hennessy, K. Clarke, and M. Lewis, "Generative adversarial network synthesis of hyperspectral vegetation data," *Remote Sensing*, vol. 13, no. 12, 2021.

[98] S. Demir, K. Mincev, K. Kok, and N. G. Paterakis, "Data augmentation for time series regression: Applying transformations, autoencoders and adversarial networks to electricity price forecasting," *Applied Energy*, vol. 304, p. 117695, 2021.

[99] H. Murtaza, M. Ahmed, N. F. Khan, G. Murtaza, S. Zafar, and A. Bano, "Synthetic data generation: State of the art in health care domain," *Comput. Sci. Rev.*, vol. 48, p. 100546, 2023.

[100] M. Ehrhart, B. Resch, C. Havas, and D. Niederseer, "A conditional gan for generating time series data for stress detection in wearable physiological sensor data," *Sensors*, vol. 22, no. 16, 2022.

[101] J. Chang, F. Hu, H. Xu, X. Mao, Y. Zhao, and L. Huang, "Towards generating realistic wrist pulse signals using enhanced one dimensional wasserstein gan," *Sensors*, vol. 23, no. 3, 2023.

[102] A. Asperti and V. Tonelli, "Comparing the latent space of generative models," *Neural Computing and Applications*, vol. 35, no. 4, p. 3155 – 3172, 2023.

CHAPTER 3

MEASURING SEDIMENTATION PROFILES FOR NANOPARTICLE CHARACTERIZATION THROUGH A SQUARE SPIRAL RESONATOR SENSOR

sensors

MDPI

Article

Measuring Sedimentation Profiles for Nanoparticle Characterization through a Square Spiral Resonator Sensor

Miguel Monteagudo Honrubia [1,†], Gianluca Caposciutti [2,†], Francisco Javier Herraiz-Martínez [1,†], Javier Matanza Domingo [1,†], Bernardo Tellini [2,†] and Romano Giannetti [1,†,*]

[1] Institute for Research in Technology, ICAI School of Engineering, Comillas Pontifical University, 28015 Madrid, Spain; mmonteagudo@comillas.edu (M.M.H.); fjherraiz@icai.comillas.edu (F.J.H-M.); jmatanza@comillas.edu (J.M.D.)

[2] Department of Energy, Systems, Territory and Construction Engineering, University of Pisa, 56122 Pisa, Italy; gianluca.caposciutti@unipi.it (G.C.); bernardo.tellini@unipi.it (B.T.)

* Correspondence: romano@comillas.edu; Tel.: +34-915406283

† These authors contributed equally to this work.

Abstract: Metallic nanoscale particles attract a growing interest in several fields, thanks to their unique bonding characteristics; applications are appearing in the literature in the fields of, for example, sensor coatings and biochemical compound detection. However, the controlled fabrication of such nanopowders is often cumbersome, especially because their characterization is normally slow, involving procedures such as electron microscopy. On the other hand, microwave sensors based on near-field effects on materials are being developed with high sensitivity and show promising characteristics. In this paper, the authors show how a microwave sensor based on a Square Spiral Resonator can be used to characterize paraffin dispersions of nanoparticles conveniently and cost-effectively.

Keywords: microwave sensors; permittivity; metallic nanoparticles; sedimentation

Citation: Monteagudo Honrubia, M.; Caposciutti, G; Herraiz-Martínez, F.J.; Matanza Domingo, J.; Tellini, B.; Giannetti, R. Measuring Sedimentation Profiles for Nanoparticle Characterization through a Square Spiral Resonator Sensor. *Sensors* **2024**, *24*, 2735. https://doi.org/10.3390/s24092735

Academic Editor: Antonio Lázaro

Received: 5 March 2024
Revised: 15 April 2024
Accepted: 22 April 2024
Published: 25 April 2024

1. Introduction

1.1. The Challenge of Nanoparticle Characterization

Nanoparticles (NPs) are ultrafine particles with an equivalent size in the order of 10^{-9} m. More concretely, particles ranging from 1 to 100 nm are usually referred to as nanoparticles. Powders of such dimensions show easy bonding with the contacting materials, large surface area, low melting point, and peculiar electromagnetic and optical properties. For these reasons, NPs are appealing for use as a sensing element and for controlling the characteristics of the materials once deposited or dispersed [1].

For example, metal nanopowders find significant utility as sensing elements in biomedical sensors, leveraging phenomena such as surface plasmon resonance [2,3]. In particular, metal NPs can selectively form bonds with enzymes, antibodies, or proteins of different structures. These bonds alter the surface light-absorption properties, enabling the precise measurement of the characteristics of the bound material with heightened sensitivity and specificity [4,5]. Metal NPs are also utilized in the thermal and photo-thermal treatment of cells [3]. For instance, the deposition of stable NPs over a specific target improves the local irradiation capability and allows for better control over laser treatments [6]. Furthermore, these particles can be exploited as coating agents for their antimicrobial properties [7] and, more broadly, enhance the mechanical characteristics and chemical resistance of surfaces [8,9]. More recently, nano-sized $LiMn_2O_4$ was utilized for the realization of the battery's cathodes [10]. Specifically, using such nanoparticles increases the mechanical flexibility of the system and its electrical capacity due to the extensive surface area provided by the NPs.

The characteristics of the particles are mainly determined during their fabrication. In general, these processes can be divided into bottom-up and top-down ones. In the former,

single or small clusters of molecules are utilized as the building block for producing NPs with controlled shape and size. For example, the chemical vapor deposition method is widely used for this purpose [11]. Generally, a gas reactant passes through a substrate where the nanoparticles layers are formed due to heterogenous reactions [12]. Although the bottom-up methods can provide fine control of the process outcome, these are generally energy- and cost-demanding, producing environmentally harmful by-products. Other techniques can produce small particles from a bulk material (i.e., top-down approaches). For example, laser ablation allows for the production of metal NPs with sizes in the order of tens of nanometers, employing high-power laser pulses with nanosecond duration [13]. Similar approaches, such as mechanical milling, sputtering, or thermal evaporation [14], take advantage of the lower cost and hardware complexity but are ineffective for the precise control of particle shapes and dimensions or for the manufacture of extremely small elements. Other methods, such as exploding wire [15], enable a reduction in thermal losses through localized power dissipation, possibly enhancing productivity and energy efficiency, and the ability to produce multicomponent nanostructures, even when immiscible with standard techniques [16,17].

In this framework, nanoparticle characterization is of paramount importance in evaluating the outcome of production processes in a timely and convenient way, adjusting the fabrication parameters in a tight loop to obtain the desired characteristics. However, exploring the nanoscale to determine properties such as particle size, size distribution, surface charge, or shape is not a trivial task [18]. In an extensive review, Mourdikoudis et al. summarized the whole toolbox of techniques to characterize nanoparticles [19]. For example, the determination of key size parameters is commonly achieved through microscopy techniques, such as scanning electron microscopy (SEM) or transmission electron microscopy (TEM). These methods reconstruct images of the particles, enabling the assessment of dimensional distributions, including circularity and equivalent diameter via image analysis methods. In contrast, spectroscopy techniques, such as dynamic laser scattering, rely on the interaction between a laser beam and the Brownian motion of the particles to obtain information on the equivalent diameter of particles [20]. In addition, other techniques, such as energy-dispersive X-ray spectroscopy (EDS), can be employed to identify the chemical elements present in products. An alternative approach involves the analysis of NP sedimentation in liquid dispersions, where the interplay of diffusion and gravity forces determines the behavior and characteristics of NPs. Thus, by studying the dynamic of the dispersed NP, their size and density can be estimated, e.g., in combination with digital imagery techniques [21] and proper modeling approaches.

Unfortunately, these characterization methods require either time-consuming protocols or complex instrumentation, with a significant share of manual interventions, causing long delays among runs of the fabrication process. Therefore, new analysis procedures are required to assess the NPs' features with lower costs. This article proposes a Microwave (MW) sensor based on Spiral Square Resonators (SSR) to measure the dynamic changes in the dielectric properties of NP dispersions due to sedimentation. This novel approach enables a fast and straightforward measuring protocol that requires low volumes, simplifying the characterization of NPs with minimal waste of fabricated samples. This research shows the potential of low-cost SSR sensors to monitor the sedimentation process of NPs with diverse chemical compositions and initial solution concentrations.

1.2. Microwave Sensor

MW sensors, particularly Split-Ring Resonator (SRR) sensors, provide a flexible and cost-effective method for characterizing materials. Regardless of the design, the sensor operates as a notch filter represented by a high-frequency RLC resonant circuit with a high-quality factor. Since the resonator capacitance is related to the medium permittivity, any medium change, such as the presence of the target material, would lead to a shift in the resonance frequency [22]. The variation in the resonance frequency depends on the dielectric characteristic of the target material; larger permittivity would lead to larger

frequency shifts. On the other hand, the topology and dimensions of the SRR define the resonance frequency; therefore, the sensor design can be tuned to work for different applications in a specific range of frequencies [23]. Spiral resonator design allows smaller electrical dimensions, enhancing the quality factor and the sensitivity [24].

Moreover, the number of resonators is not limited to one, and several resonators in a symmetric configuration can improve the resonance. These sensors have proven potential for numerous applications, including the dielectric characterization of thin layers since the miniaturizing resonators will confine the electric field in the near space surrounding [25]. This paper proposes a Square Spiral Resonator sensor in the microwave regime to measure nanoparticle sedimentation. The deposition of nanoparticles will create a uniform layer in the sensor surface, modifying the capacitance of the equivalent resonant circuit, thereby changing the resonance frequency along the sedimentation time (Figure 1). The maximum frequency shift and the convergence time to the "layer" resonance frequency are related to the dispersion concentration and the sedimentation dynamics of different nanoparticles.

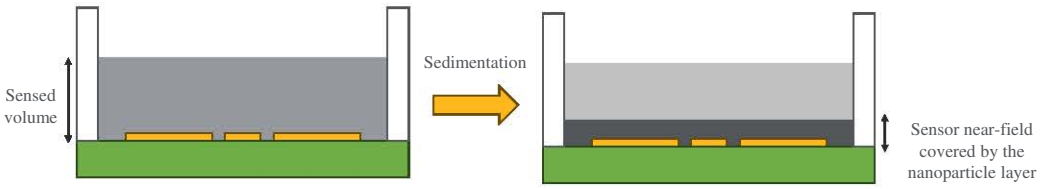

Figure 1. Sedimentation process in the sensor.

2. Methods

2.1. Sedimentation of Nanoparticles

The sedimentation of solid particles in a liquid medium mainly depends on the density and shape of the solid elements and on the viscosity, density, and temperature of the liquid. With the purpose of providing a simple but reliable description of the sedimentation and of introducing the method exploited for NPs study, we consider the contribution of the Brownian and the gravitational forces in a mono-dimensional system (i.e., along the x-axis) over time t. Therefore, the concentration c of the disperse phase of solid particles behaves according to the Mason–Weaver Equation (1) [21,26].

$$\frac{\partial c}{\partial t} = D\frac{\partial^2 c}{\partial x^2} + v\frac{\partial c}{\partial x} \tag{1}$$

where D and v are experimental coefficients depending on the particle size, density, and liquid physical characteristics. In particular, $D = k_b T/F$ is the diffusion coefficient depending on the fluid temperature T, the Boltzman constant k_b, and the frictional coefficient F. Moreover, $v = m_b g/F$ is the sedimentation velocity that depends on the buoyancy mass, m_b; on the gravitational acceleration g; and on F. For spherical particles with radius r and density ρ, and a liquid with viscosity η and density ρ_L, $F = 6\pi\eta r$ and $m_b = \frac{4}{3}\pi r^3(\rho - \rho_L)$ [21]. We further assume that $\frac{\partial c}{\partial x} + \frac{v}{D}c = 0$ at $x = 0$ and $x = x_{max}$, and $c(t = 0, x) = c_0$, where x_{max} is the maximum system length and c_0 is the initial concentration). The solution of Equation (1) shows that c changes with t, finally achieving an equilibrium distribution for $t \to \infty$ [21]. This result can be interpreted as the growth of a particles layer on the sensor surface, thus increasing the average permittivity in the sensitive volume of the sensor and hence decreasing the value of the measured resonance frequency f. The evolution of f vs. t depends on the sedimentation dynamic, and it is peculiar to the particle's material, dimension, and initial concentration. Therefore, by monitoring such behavior we can carry out information on the properties of the solid dispersed phase. Although the model in Equation (1) does not consider particle clustering processes, which could influence the sedimentation dynamic and hence the attended readout [27], it offers a proof-of-concept of the operating principle of the sensor and can be used as a basis for a discussion about the obtained results.

2.2. Nanoparticle Production

Copper- and iron-based nanoparticles were produced at the facility of the University of Pisa. We adopted a wire explosion method for NPs fabrication, and we used a microscopy-based technique to assess the main size characteristics of the products. The NPs are produced by flowing a current in the order of 1×10^7 A/m^2 to 1×10^9 A/m^2 through a cylindrical copper or iron wire with a diameter of 1 mm and 30 mm length. The current is provided by a 765 µF capacitor, with a voltage limit of 10 kV, loaded through a High Voltage (HV) power supply. Voltage and current are monitored during the process by utilizing a 1:1000 dedicated voltage probe, a calibrated Rogowski coil, and an oscilloscope (Lecroy W wave Pro 725Zi, Teledyne LeCroy, Italy) with four 8-bit boards and 2.5 GHz bandwidth. Due to the high current density, the process enables adiabatic heating of the sample, which rapidly vaporizes to form small clusters of molecules, further condensing in contact with the surrounding medium, thus producing the NPs. To collect the product and control the explosion environment, we utilized distilled water as a medium surrounding the exploding wire. A picture and a scheme of the utilized setup are shown in Figure 2.

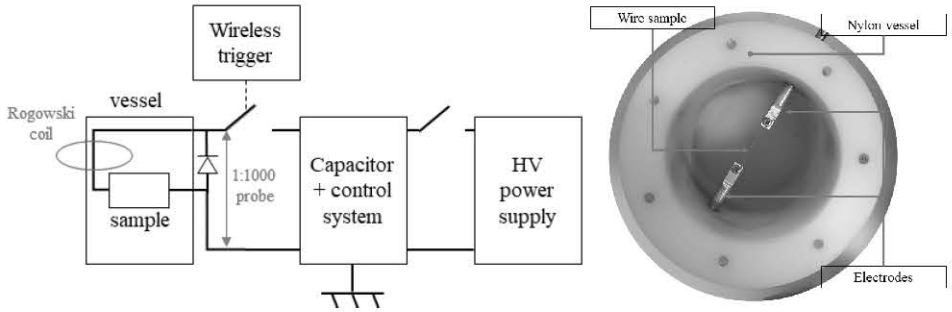

(**a**) (**b**)

Figure 2. The scheme of the exploding wire setup (**a**) and a picture of the vessel (**b**) utilized for NPs fabrication.

We produced the copper-based NPs (Cu-NPs) and iron-based NPs (Fe-NPs) separately. A single sample was subjected to explosion, and the resulting water containing the nanoparticles was collected in a larger container. Subsequently, the explosion vessel and electrodes were accurately cleaned with deionized water to minimize any contamination between the test runs. This procedure was iterated ten times to ensure the fabrication of an average representative sample. The nanoparticles were ultimately extracted from the liquid via a low-temperature evaporation process. Therefore, they were diluted in deionized water, deposited on dedicated samples, and prepared for microscopy analyses (Figure 3).

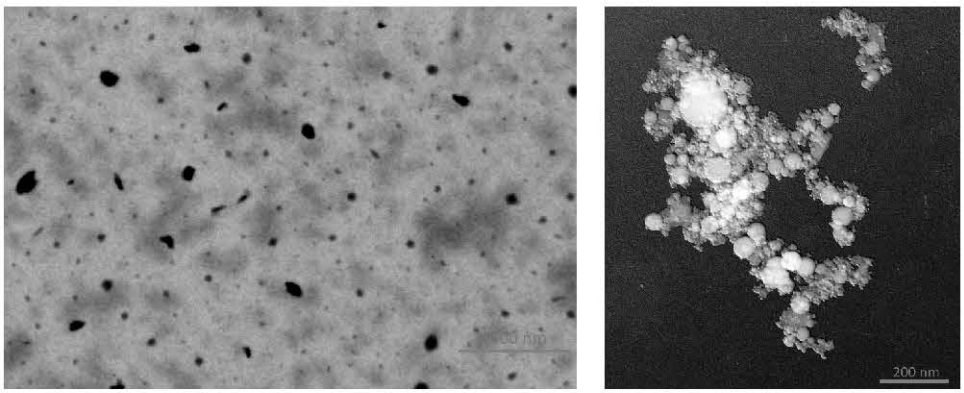

(**a**) (**b**)

Figure 3. Sample images of Cu-NPs at 160,000×magnification obtained with a bright field STEM detector (**a**) and of Fe-NPs at 200,000× magnification obtained with a STEM detector (**b**).

To provide an indication regarding the dimensions of the smaller synthesized elements, we examined the images at a magnification of 160,000× and 200,000× via a particle counting.

The copper-based NPs were analyzed using the FEG-SEM (FEI QUANTA 450 ESEM-FEG, Thermo Fisher Scientific, Hillsboro, OR, USA), and the HR FEG-TEM (JEOL JEM-F200, Jeol Ltd., Tokyo, Japan) was used for the iron-based NPs. These instruments are available at the Center for Instrument Sharing of the University of Pisa (CISUP). The results regarding the particle size distribution (evaluated as probability density functions, pdf, of d_{eq}) are shown in Figure 4. Finally, the minimum, average, median, and maximum equivalent diameter of the sampled NPs, analyzed at a magnification within 160,000× and 200,000×, are reported in Table 1.

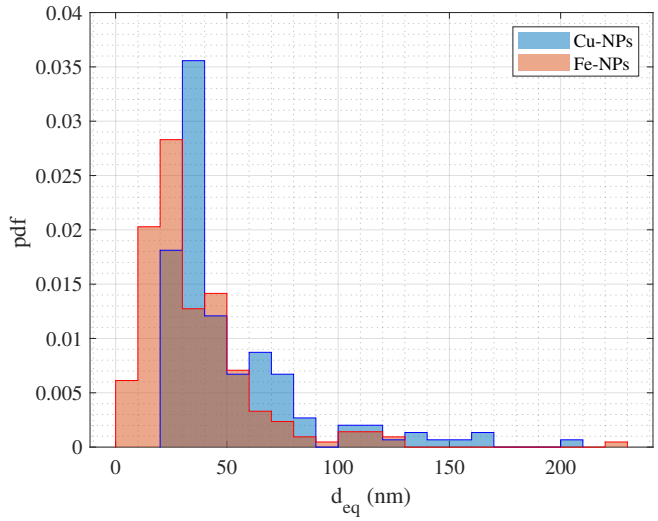

Figure 4. Dimensional distribution of the equivalent diameter, d_{eq}, of the NPs analyzed samples.

The EDS analysis was also performed, confirming the production of Cu-based and Fe-based nanoparticles. However, the presence of oxygen, along with copper and iron, respectively, possibly indicates an oxidized state of the products. Metallic impurities, mainly aluminum, are present in minor proportion due to the electrodes erosion.

Table 1. Main parameters of the dimensional distribution of the analyzed samples.

	Minimum d_{eq}	**Median d_{eq}**	**Average d_{eq}**	**Maximum d_{eq}**	
Cu-NPs	29	35	52	204	(nm)
Fe-NPs	6	28	36	228	(nm)

2.3. Sensor Structure

The SSR sensor designed for this paper (Figure 5) has two copper square spirals separated by a microstrip transmission line (TL), which excites both resonators through the incident microwave signal. The TL and the spiral resonators are located in the same plane (the top layer of the PCB). As the propagating mode of the microstrip TL is a quasi-TEM mode, there is a magnetic field perpendicular to the spirals surface that excites both resonators. The spirals produce a notch in the reflection coefficient of the TL at their resonant frequency. Two spiral resonators instead of one are coupled to the TL because it produces a deeper notch in the reflection coefficient. The copper TL and the spirals are etched in a copper-grounded PCB ($l_c = 25\,\text{mm}$, $w_c = 20\,\text{mm}$) made of FR-4 substrate with a relative permittivity $\varepsilon_{\text{sub}} = 4.5$ and a thickness of $h_{\text{sub}} = 1.5\,\text{mm}$. The TL crosses the whole PCB with a width of $w_{TL} = 2.82\,\text{mm}$ and a thickness of $h_{TL} = 0.35\,\text{mm}$. The width was selected to adjust the characteristic impedance of the TL to 50 Ω, while the length of the TL was set to achieve good impedance matching at the resonant frequency of the spiral resonators. The center of both spirals is at the middle of the TL, and each spiral is separated from the TL with a distance of $d = 0.44\,\text{mm}$. The same gap distance (d) is the width of each spiral arc as well as the gap between them. The spiral dimensions ($l_{sp} = w_{sp} = 5.06\,\text{mm}$) set the sensor resonance frequency at the vacuum reference.

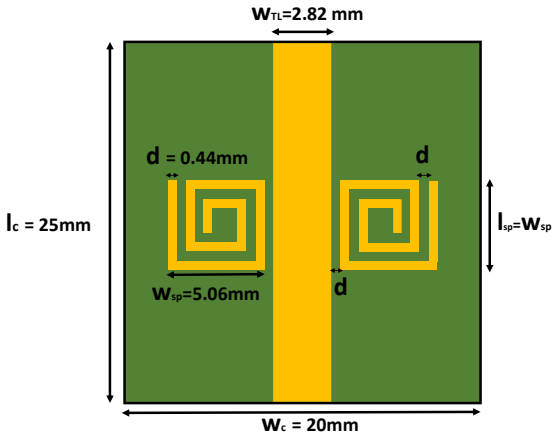

Figure 5. PCB layout of the sensor.

The sensor was simulated by using the EM transient solver of CST Studio Suite (Dassault Systemes, Paris, France). Figure 6 shows the result of the EM simulations. The resonance frequency of the SSR-based sensor in vacuum is 2.444 GHz. The simulations also show the operation principle of the sensor. When the SSRs are covered with a material, there is a shift in the notch frequency related to the relative permittivity of the covering material. In the simulations, the SSRs were covered with paraffin oil (relative permittivity $\varepsilon_{\text{par}} = 2.13$ [28]) to show how the resonance frequency is shifted towards lower frequencies. In particular, the notch is shifted from 2.444 to 2.247 GHz when covering the sensor with paraffin oil.

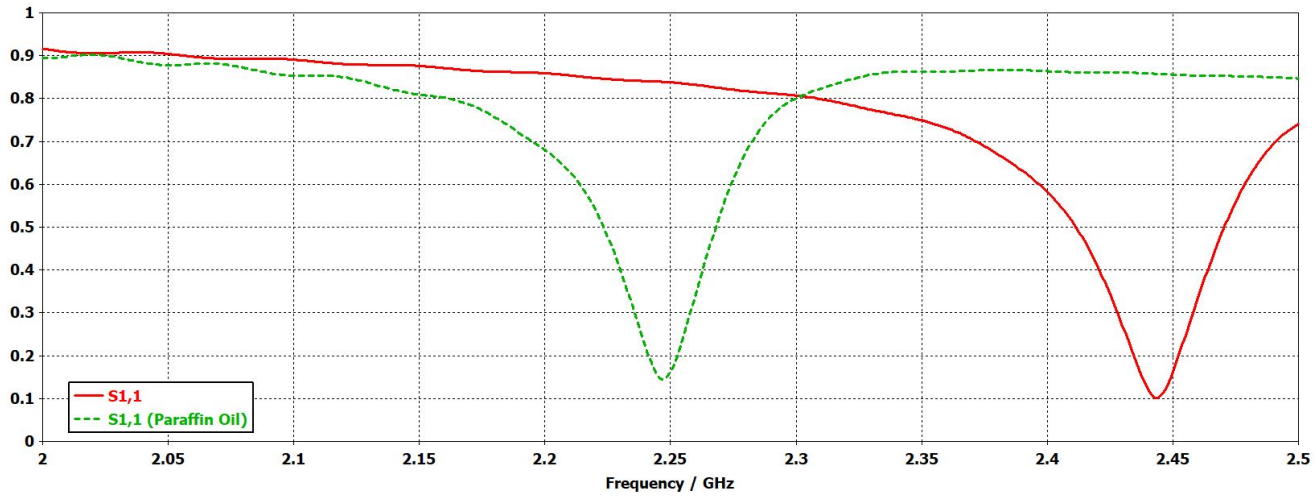

Figure 6. Simulated reflection coefficient ($|s_{11}|$) of the sensor in vacuum (solid red) and covered with paraffin oil (dashed green).

The sensor TL is welded to an SMA (SubMiniature A, RS Pro) connector, which is the interface for a vector network analyzer (VNA). The VNA (MS46122B, Anritsu, Atsugi, Japan) operates in the 1-port mode configuration to collect the reflection coefficient of the SSR, `|s11|`, in the frequency domain. The VNA was calibrated in the 2.23 GHz to 2.46 GHz range to acquire the measurements, with a sampling buffer of 7000 points every 15 s. The SRR sensor presents a drift of 3 MHz around the resonance frequency due to the connection with the VNA port and experimental variability. In order to perform the measurements, a 3D-printed polylactic acid (PLA) container was glued with cyanoacrylate to the substrate to keep the dispersion of NPs in place (see Figure 7). The container was fabricated with a fused deposition modeling (FMD) 3-D printer (i3 Mega, Anycubic, Hong Kong, P. R. China). This container was not considered in EM simulations for simplicity. Thus, a small frequency shift is expected in the experimental results due to this fact and tolerances in the manufacturing process.

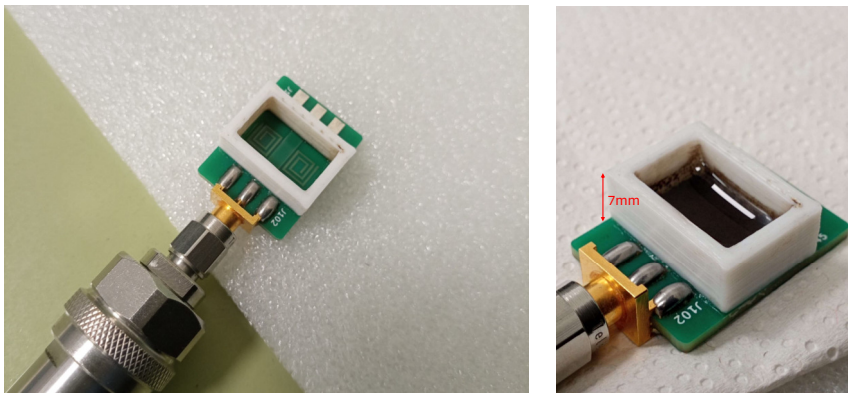

(**a**) (**b**)

Figure 7. SRR sensor with the glued PLA pool: unloaded (**a**) loaded with a paraffin dispersion (**b**).

2.4. Measurement Protocol

We prepared nanoparticle dispersions by mixing Cu-NPs and Fe-NPs with liquid paraffin, a mineral oil mainly used for medical and cosmetical applications, with a low relative permittivity ($\varepsilon_{\text{par}} = 2.13$) [28]. Paraffin is a non-polar liquid that does not interact electrically with the nanoparticles, leaving gravity as the only acting force during sedimentation. In particular, the samples were prepared using a sonicator (Branston Digital Sonifier Model 450), which applied sound energy to agitate particles, resulting in homogeneous dispersions. The sonication was performed using a 50 % tip amplitude for 15 min in pulsed mode, with a cycle of 15 s of activation and 5 s of rest. During this process, the tube containing the dispersion was submerged in water with ice to keep the nanoparticles' temperature under control. Thus, each measurement is performed at a similar temperature in order to evaluate only how the nanoparticle type or concentration affects the sedimentation. After the sonication, a volume of 500 µL was placed inside the sensor PLA container for characterization. For comparison purposes, the measurements were performed for iron and copper nanoparticle dispersion at different concentrations. We expect that the sedimentation will assure a reproducible layer of nanoparticles directly proportional to the dispersion concentration.

The samples used for measurements started from a very saturated dispersion, around 20 mg/mL for Cu-NP and 15 mg/mL for Fe-NP. Afterward, the concentrations tested were reduced in steps of 5 mg/mL until a concentration near the paraffin reference signal was reached. On the other hand, all the fabricated Cu-NP mass (440 mg) was loaded in the sensor to characterize the dry nanopowder and compare its dielectric properties with the paraffin dispersion. In contrast, just half of the fabricated Fe-NP mass (170 mg) was analyzed due to its strong loss tangent. Nevertheless, a quantitative comparison of powder masses could not be achieved without a method to standardize compaction. Although the powder mass is a parameter directly proportional to the frequency shift, the critical factor is the compaction, which defines the internal volume of air and, consequently, the relative permittivity. For this reason, a direct permittivity measure of powder substances is hard to obtain, especially for resonant methods. However, additional solvents (500 µL) with known relative permittivity and loss tangent were measured to establish bounds for the NP dispersions dielectric properties (Table 2).

Table 2. Dielectric properties of several solvents at microwave frequencies.

	ε_r	$\tan\delta$	Reference
Paraffin oil	2.13	0.001	[28]
Hexane	1.83	0.0022	[29]
Olive oil	2.92	0.046	[30]
Ethyl Ether	4.24	0.026	[31]

3. Results and Discussion

3.1. Dielectric Characterization of Nanopowders

Figure 8 shows the resonance frequency shift and the amplitude reduction for several solvents, Cu-NPs paraffin dispersions, and air as the unloaded sensor reference. Moreover, the dry Cu nanopowder was also characterized before being dispersed in paraffin oil. This manually compacted sample shows a significant reduction in the resonance amplitude, which is an indicator of electromagnetic loss ($\tan\delta$), close to the amplitude measured for ethyl ether ($\tan\delta_{ETHER}$). In addition, its relative permittivity is bounded in the range between the values of paraffin oil [28] and hexane [29] (1.83 to 2.13 GHz). Indeed, paraffin oil has a larger relative permittivity but lower losses since the amplitude barely changes from the air reference or the hexane signal.

These insights show that Cu nanoparticles' permittivity ($\varepsilon_{\text{nanoCu}}$) is lower than paraffin permittivity ($\varepsilon_{\text{paraffin}}$); therefore, the expected resonance frequency of the Cu dispersion before sedimentation (t = 0) should be slightly higher than liquid paraffin. Through sedimentation, the resonance frequency should increase, approaching the peak value of the dry Cu nanopowder sample. However, Figure 8 shows the opposite behavior: first, the Cu dispersion before sedimentation (t = 0) presents a resonance frequency lower than pure paraffin, and afterward, the sedimentation (t = 1.5 h) reduces the resonance frequency even more. Contrary to what was expected, these frequency shifts indicate that $\varepsilon_{\text{nanoCu}}$ should be larger than $\varepsilon_{\text{paraffin}}$.

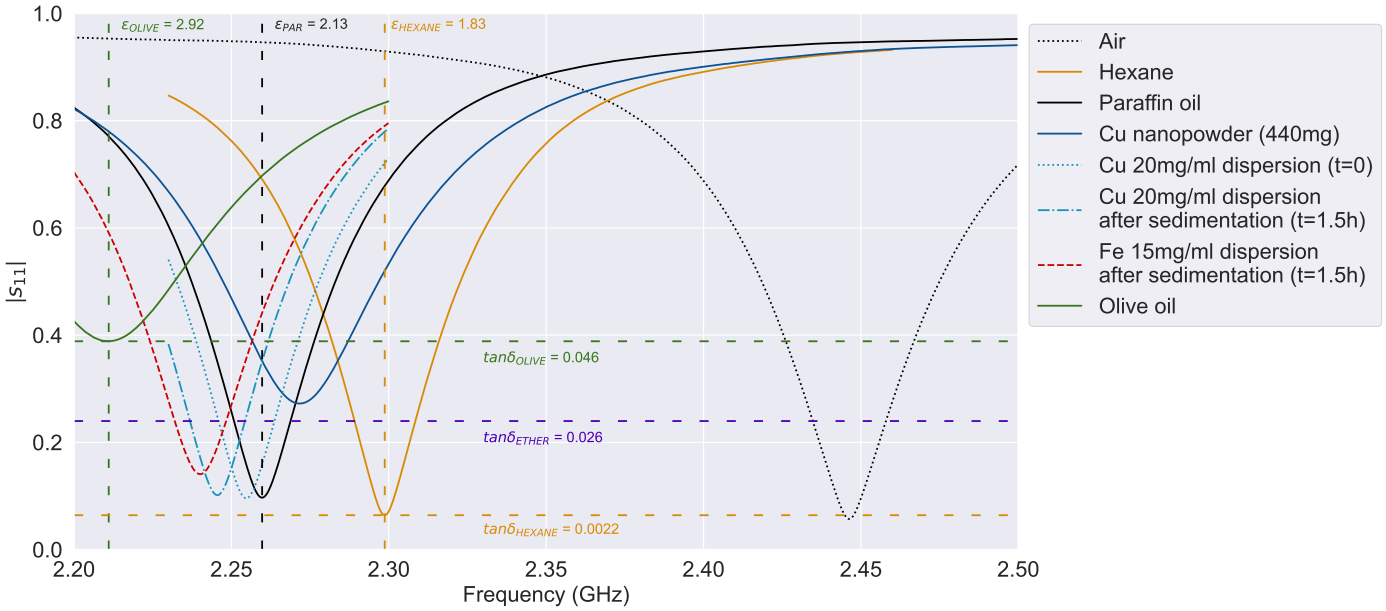

Figure 8. Sensor resonance curves for Cu nanopowders.

The explanation for this behavior is that the Cu nanopowder is indeed a mixture of nanoparticles and air so that its effective permittivity is a weighted average between NPs and air permittivity. Since air permittivity is approximately equal to vacuum permittivity, the powder's effective permittivity would be lower bound for the Cu-NP actual permittivity. Thus, depending on the apparent density of the powder, the effective permittivity would be a better approximation of the actual nanoparticle permittivity ($\varepsilon_{\text{nanoCu}}$). The same rule is applied for the paraffin dispersion, but the medium relative permittivity is now 2.13 instead of 1. In this case, since $\varepsilon_{\text{paraffin}}$ is closer to $\varepsilon_{\text{nanoCu}}$ than ε_{air}, the dispersion effective permittivity is closer from the actual $\varepsilon_{\text{nanoCu}}$. Therefore, through sedimentation, the dispersion effective permittivity approaches this value when the layer of nanoparticles is formed on the sensor surface, and the volume of paraffin is reduced in the near-field sensed volume.

The effect of compaction can explain the permittivity of Cu-NP powder, and this explanation can also be extended to Fe-NP. Nevertheless, as is depicted in Figure 9, both the

relative permittivity and the loss tangent are significantly greater than dry Cu nanopowder (Figure 8). In addition, this acute amplitude loss could be related to the ferromagnetic properties of Fe-NP. Thus, the dry Fe nanopowder response is also a lower-bound estimation, but due to its dielectric properties, it is measured beyond the paraffin response and does not seem contradictory, as happened with the Cu nanopowder lower-bound. On the other hand, as expected, the frequency response of Fe-NP dispersion is relatively close to Cu-NP dispersion since the main component of both is the liquid paraffin (Figure 9). However, the slight differences between both dispersions are due to the dielectric properties of each NP. Indeed, even if the concentration of Fe-NP (15 mg/mL) is lower than the Cu-NP concentration, the frequency shift is more pronounced for NP-Fe. It must be noted that the Fe-NP 20 mg/mL concentration was over-saturated, and it was diluted to 15 mg/mL for this comparison analysis.

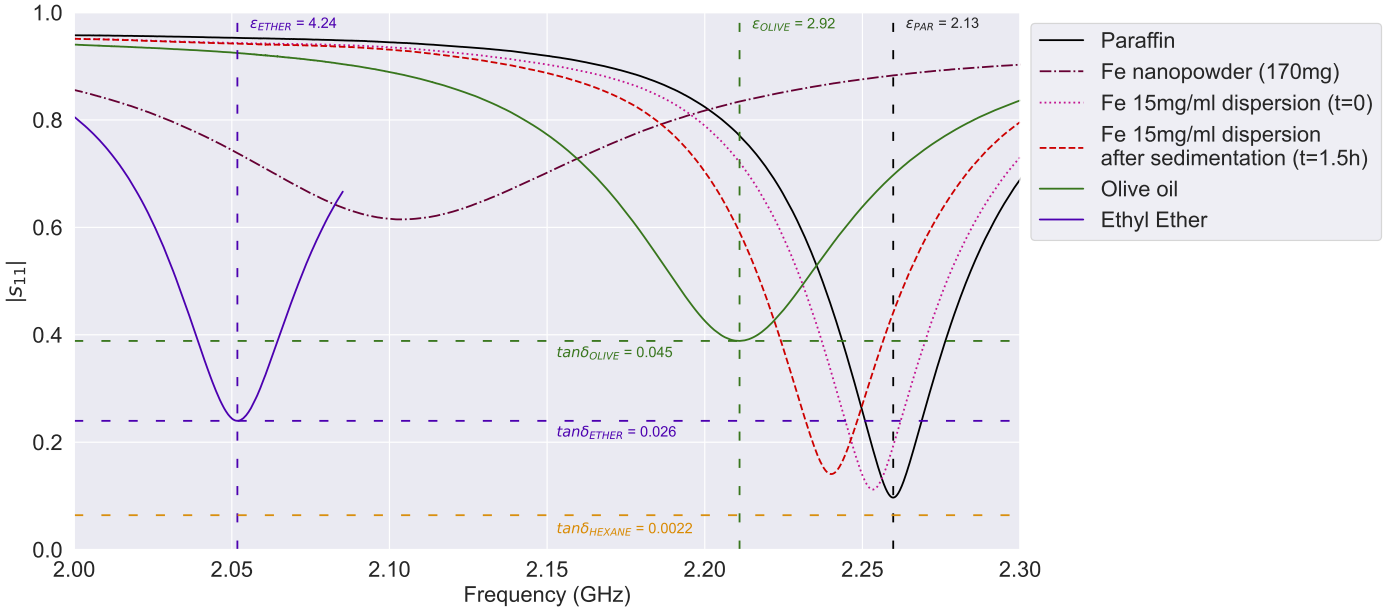

Figure 9. Sensor resonance curves for Fe nanopowder.

Despite these differences between paraffin dispersions, their dielectric response is within the boundaries of the reference solvents. While the relative permittivity varies between the values of paraffin oil [28] and olive oil [30] ($\varepsilon_r = 2.13$ to 2.92), the loss tangent is limited by the hexane [29] and ethyl ether [31] electromagnetic losses ($\tan\delta = 0.0022$ to 0.026). Likewise, the dielectric studies performed by Mergos et al. show similar slight permittivity differences between paraffin dispersions [28].

3.2. The Effect of Concentration on the Nanoparticle Sedimentation

Figure 10 shows that the resonance frequency for paraffin remains constant over time; consequently, its value can be taken as a baseline for comparison purposes, which reveals a negligible sensor drift around 3 MHz. All Cu-NPs dispersions show a steep decrease in the resonance frequency during the first hour; afterward, the effect of sedimentation on the sensor is asymptotically reduced up to a steady state value. When the concentration of the Cu dispersion is lower, e.g., see the cases considering 5 and 10 mg/mL concentrations, the initial resonance frequency is within the range of liquid paraffin signals, proving that the dielectric effect of nanoparticles in the bulk liquid is minimal. Indeed, after 3 h the Cu 5 mg/mL layer value is almost below the detection limit of the sensor. Therefore, for lower concentrations, we expect that the formed NPs layer would not have enough impact on the permittivity measured by the sensor. However, the variation of resonance frequency due to the sedimentation is still noticeable even though the resonance frequencies for both dispersions overlap with the paraffin one.

The sedimentation curve is steeper for higher concentrations, such as Cu 15 or 20 mg/mL, in comparison to Cu 5 or 10 mg/mL. Moreover, the agglomeration between the particles, which is not studied within this paper, could play a relevant role in determining a quicker sedimentation at higher NPs concentrations. It should be noted that Cu 30 mg/mL was over-saturated after sonication, and sedimented particles were observed at the bottom of the tube. For this reason, the Cu 30 mg/mL signal is quite similar to Cu 20 mg/mL, which is very close to saturation.

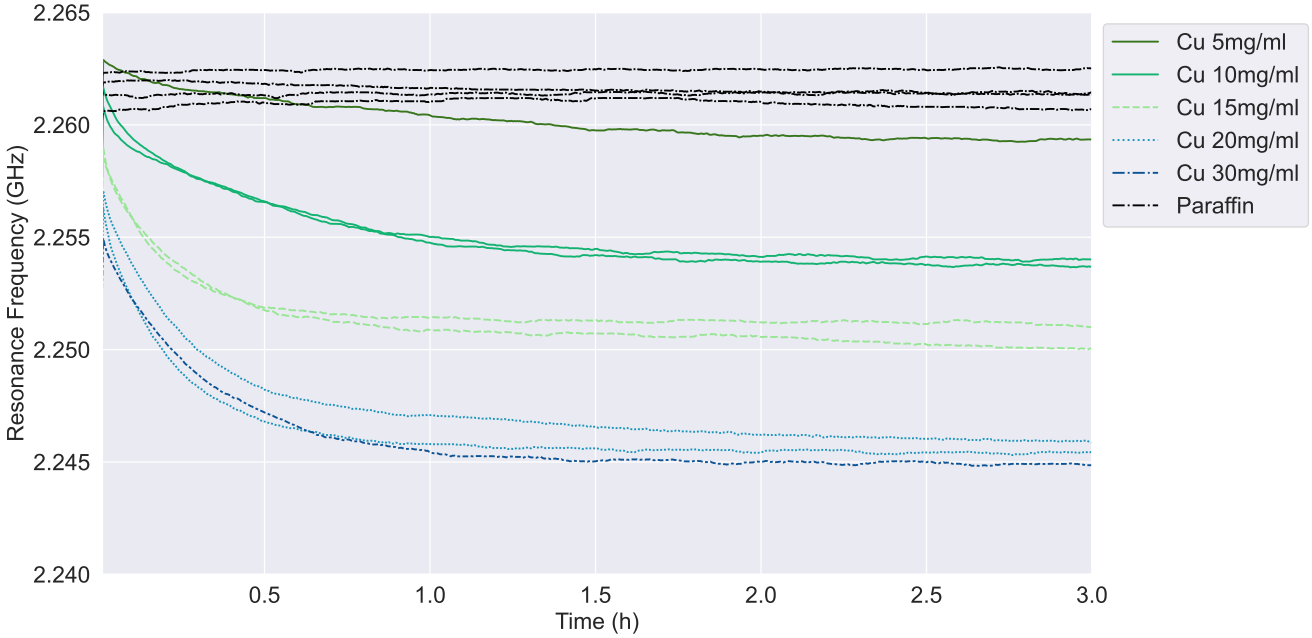

Figure 10. Resonance frequency versus time in the case of different concentrations of Cu nanopowder.

In contrast, the Cu-NP sedimentation within the sonication tubes shows less noticeable changes in the 3-h interval (Figure 11). Indeed, the complete sedimentation time is considerably longer; even after 6 h, most of the NP are still dispersed in the paraffin. This long operation time has been the main drawback of sedimentation techniques for NP characterization, such as measuring the bulk fluid with absorption spectroscopy [32]. However, the measured sedimentation profiles indicate that the SRR sensor can achieve a faster detection time since it aims to measure only the bottom thin layer made by the first NP sedimented. In combination with the high sensitivity in the near-field from the SRR surface, the sensor does not require waiting until the sedimentation is finally complete.

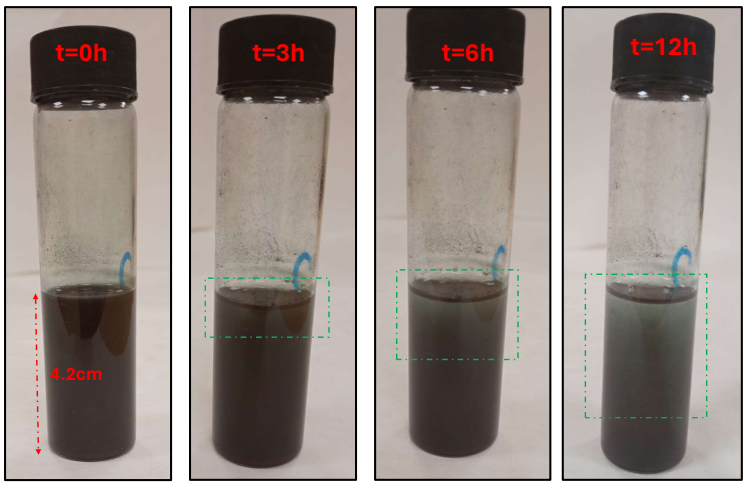

Figure 11. Cu-NP dispersion (15 mg/mL) at different times after sonication; the green boxes show the liquid volume that is starting to become transparent due to sedimentation.

On the other hand, Figure 12 shows a similar sedimentation dynamic in the case of Fe dispersion samples. The main difference is that Fe dispersion requires a lower concentration to achieve a resonance frequency similar to Cu sedimentation curves. These results match with the dielectric characterization of nanopowders. For example, Fe 10 mg/mL dispersion has a similar resonance frequency to Cu 15 mg/mL, and the previous detection limit is reduced from Cu 5 mg/mL to Fe 2.2 mg/mL. In addition, Fe 15 mg/mL achieves a higher frequency than Cu 20 mg/mL, with both concentrations being the saturation limit of each nanopowder. This difference in solubility is directly related to the properties and can be determined with the SSR sensor.

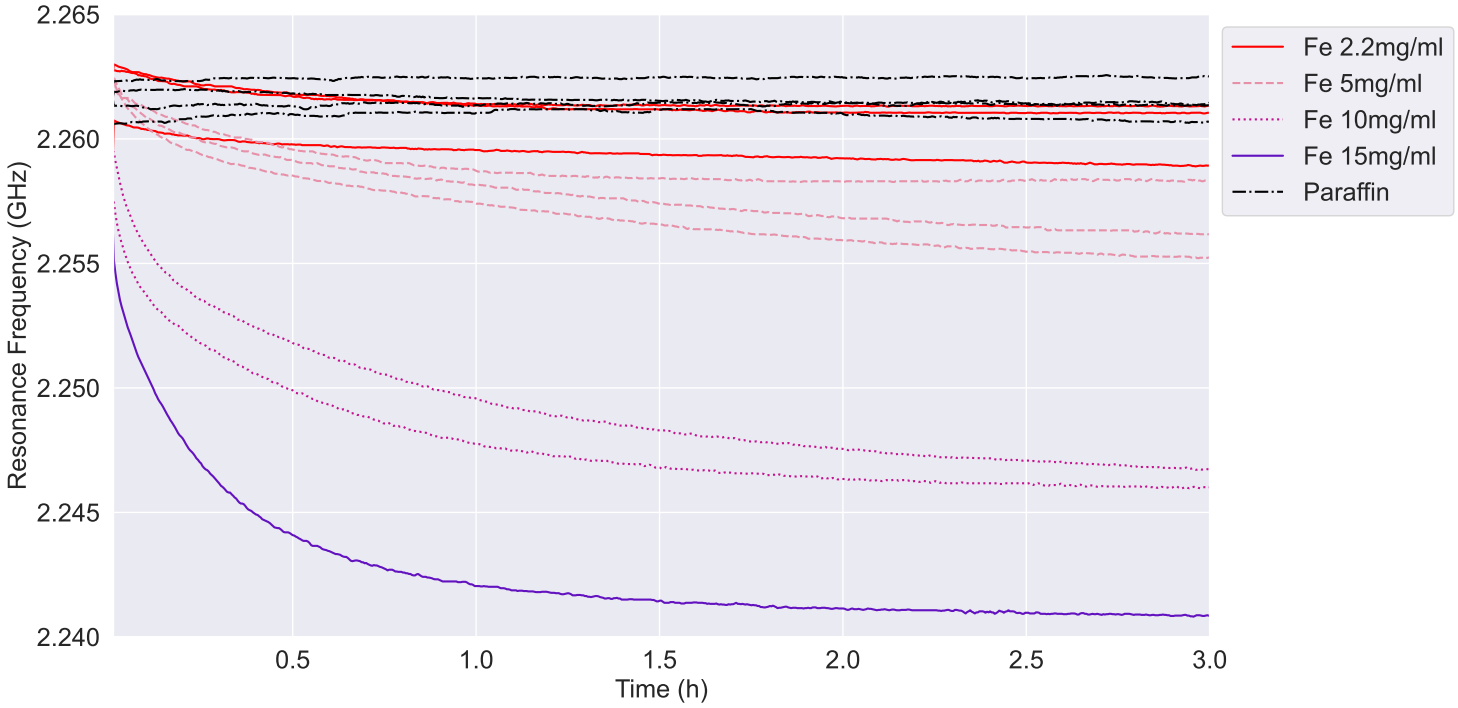

Figure 12. Resonance frequency versus time in the case of different concentrations of Fe nanopowder.

Both Figures 10 and 12 show a decay of the resonance frequency measured by the SSR sensor as a function of the time, which is consistent with the conceptional principle described in Section 2.1. We recall that, according to Equation (1), c changes vs. t, finally reaching an equilibrium distribution for $t \to \infty$. We interpret this occurrence as the deposition of NPs to form a growing layer on the sensor surface. As the layer grows, the average relative permittivity in the sensor sensitive region increases too, thus decreasing the value of the measured resonance frequency. Looking at Figures 10 and 12, we can observe a qualitative agreement vs. t between f and $1/c$, presented in Figure 13.

In particular, the higher is the initial concentration, the lower the equilibrium resonance frequency is obtained. However, experimental results indicate a faster frequency decay right from the onset of the process as a function of the initial NPs concentration. We also notice that a faster decay appears by simulating larger particles utilizing the Mason–Weaver model (see Figure 13). Hence, we infer that such a decay could arise due to particle clustering, which is likely influenced by the solid phase concentration [33]. Although Equation (1) model is not able to take into account such a phenomenon, it offers a simple yet reliable basis for discussion, substantially contributing to the validation of our results. In this context, the SSR sensor has demonstrated the capability of carrying out relevant information on the sedimentation dynamic, and hence of the NPs properties and their concentration, through the analysis of the medium resonance frequency, thus highlighting the potential of the proposed technique for characterizing metallic nanopowders.

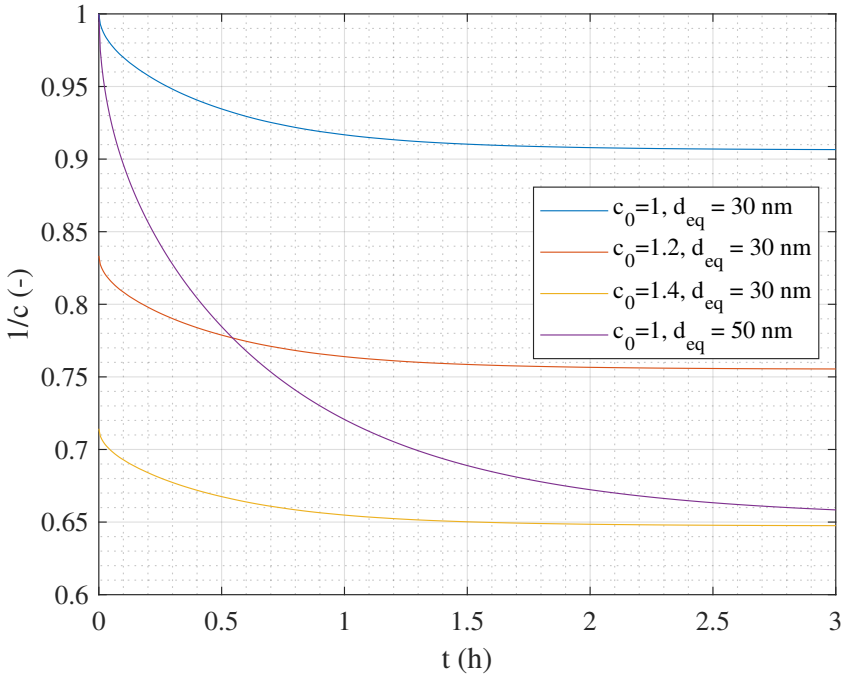

Figure 13. Example of $1/c$ calculated at $x = 0.1$ mm. $c(t)$ is obtained by solving the Mason–Weaver equation with $T = 300$ K, and various initial concentration and particle diameters.

4. Conclusions

We studied the effect of sedimentation of NPs in a viscous media through the measurement of the electrical characteristics of the paraffin-NPs dispersion over time through an MW sensor. The sensor is based on two SSRs coupled to a printed TL, and it operates in the MW regime. A resonant notch is observed in the reflection coefficient of the sensor. The resonant frequency depends on the materials deposited over the sensor surface. In particular, several dispersed solution samples were prepared by employing Cu- and Fe-based nanoparticles and paraffin oil. The NPs used in the experiments have been produced via a wire explosion process. During the experiments, we observed a reduction in resonance frequency and signal reflection over time, both attributed to the impact of sedimentation on the dispersed solution properties. Moreover, all the sedimentation profiles converge after 3 h, suggesting that the nanoparticle layer measurable by the SRR is completed at that time. Therefore, the methodology proposed in this research is a relative fast technique to characterize nanoparticles. Indeed, our investigation enabled the differentiation of distinct patterns arising from varied types and concentrations of nanopowders within the solution. Therefore, we used the Mason–Weaver model as a basis for the discussion of the results. These insights point to the possibility of using MW sensors to characterize the outcome of nanopowders production. Although the results are indeed quite tied to the structure of the specific sensor and require a uniform preparation of the sample, the repeatability is high, and the differences between different types or concentrations of NPs are clearly detectable with few parameters like time constant and final steady-state value of the resonance frequency evolution.

The results of this research also suggest that a concentration around 10 mg/mL is the most optimal for characterizing Fe-NP and Cu-NP due to a compromise between dielectric response and product waste. Moreover, measuring the sedimentation with the SRR sensor could reveal other NP characteristics beyond dispersion concentration or chemical composition. For example, the particle size could be estimated since the sedimentation time depends on the gravitational pull, which will be stronger for larger particles. In addition, the microwave sensor technology could be improved by implementing low-cost electronics and machine learning techniques [34], thus reinforcing its suitability as a characterization method. In conclusion, the methodology proposed in this research is a solid and faster alternative for characterizing nanoparticles and avoiding complex instrumentation.

Author Contributions: Conceptualization, F.J.H.-M. and B.T.; methodology, R.G. and J.M.D.; software, M.M.H.; validation, M.M.H., G.C. and R.G.; formal analysis, M.M.H.; investigation, M.M.H. and G.C.; resources, B.T., J.M.D. and F.J.H.-M.; data curation, M.M.H.; writing—original draft preparation, M.M.H. and G.C.; writing—review and editing, B.T., R.G. and J.M.D.; visualization, M.M.H. and G.C.; supervision, R.G., F.J.H.-M., J.M.D. and B.T.; project administration, R.G. and B.T.; and funding acquisition, B.T. and J.M.D. All authors have read and agreed to the published version of the manuscript.

Funding: This work has been partially funded by "IIT Strategic PhD Research Grants" and "Proyectos de Investigacion Propia" programs from Universidad Pontificia Comillas.

Data Availability Statement: The raw data supporting the conclusions of this article will be made available by the authors on request.

Acknowledgments: The authors would like to express their gratitude to Christopher Michael Turner for proofreading and suggesting valuable insights about the writing and to Randa Ishak for her valuable suggestions and support for microscopy analyses.

Conflicts of Interest: The authors declare no conflicts of interest.

References

1. Naito, M.; Yokoyama, T.; Hosokawa, K.; Nogi, K. *Nanoparticle Technology Handbook*, 3rd ed.; Naito, M., Yokoyama, T., Hosokawa, K., Nogi, K., Eds.; Elsevier: Amsterdam, The Netherlands, 2018. [CrossRef]
2. Rygula, A.; Majzner, K.; Marzec, K.M.; Kaczor, A.; Pilarczyk, M.; Baranska, M. Raman spectroscopy of proteins: A review. *J. Raman Spectrosc.* **2013**, *44*, 1061–1076. [CrossRef]
3. Wojnarowska, R.; Polit, J.; Broda, D.; Gonchar, M.; Sheregii, E.M. Surface enhanced Raman scattering as a probe of the cholesterol oxidase enzyme. *Appl. Phys. Lett.* **2015**, *106*, 103701. [CrossRef]
4. Starowicz, Z.; Wojnarowska-Nowak, R.; Ozga, P.; Sheregii, E.M. The tuning of the plasmon resonance of the metal nanoparticles in terms of the SERS effect. *Colloid Polym. Sci.* **2018**, *296*, 1029–1037. [CrossRef]
5. Kong, K.; Kendall, C.; Stone, N.; Notingher, I. Raman spectroscopy for medical diagnostics—From in-vitro biofluid assays to in-vivo cancer detection. *Adv. Drug Deliv. Rev.* **2015**, *89*, 121–134. [CrossRef]
6. Rosh Abarbanel, M.; Bianchi, L.; Korganbayev, S.; Pacheco Tobo, A.L.; Ashkenazi, S.; Saccomandi, P.; Weitz, I.S. Thermal response of CuO/polydopamine nanospheres under NIR laser irradiation. *Ceram. Int.* **2023**, *49*, 24302–24311. [CrossRef]
7. Singh, A.K. Nanostructured coatings based on metallic nanoparticles as viral entry inhibitor to combat COVID-19. *Sustain. Mater. Technol.* **2023**, *35*, e00544. [CrossRef]
8. Kumar, R.; Pulikanti, G.R.; Shankar, K.R.; Rambabu, D.; Mangili, V.; Kumbam, L.R.; Sagara, P.S.; Nakka, N.; Yogesh, M. 9-Surface coating and functionalization of metal and metal oxide nanoparticles for biomedical applications. In *Metal Oxides for Biomedical and Biosensor Applications*; Mondal, K., Ed.; Metal Oxides; Elsevier: Amsterdam, The Netherlands, 2022; pp. 205–231. [CrossRef]
9. Sun, Q.; Liu, T.; Wen, T.; Yu, J. Optimization of particle size, dispersity, and conductivity of 8 mol% Y2O3 doped tetragonal zirconia polycrystalline nanopowder prepared by modified sol-gel method via activated carbon absorption. *J. Eur. Ceram. Soc.* **2022**, *42*, 5831–5841. [CrossRef]
10. Heo, K.; Im, J.; Kim, S.; Lee, C.K.; Chang, D.R.; Kim, J.; Lee, J.W.; Lim, J. Effect of nanoparticles in cathode materials for flexible Li-ion batteries. *J. Ind. Eng. Chem.* **2020**, *81*, 278–286. [CrossRef]
11. Sayago, I.; Hontañón, E.; Aleixandre, M. 9 - Preparation of tin oxide nanostructures by chemical vapor deposition. In *Tin Oxide Materials*; Orlandi, M.O., Ed.; Metal Oxides ; Elsevier: Amsterdam, The Netherlands, 2020; pp. 247–280. [CrossRef]
12. Yan, K.; Fu, L.; Peng, H.; Liu, Z. Designed CVD Growth of Graphene via Process Engineering. *Acc. Chem. Res.* **2013**, *46*, 2263–2274. [CrossRef]
13. Balachandran, A.; Sreenilayam, S.P.; Madanan, K.; Thomas, S.; Brabazon, D. Nanoparticle production via laser ablation synthesis in solution method and printed electronic application—A brief review. *Results Eng.* **2022**, *16*, 100646. [CrossRef]
14. Abid, N.; Khan, A.M.; Shujait, S.; Chaudhary, K.; Ikram, M.; Imran, M.; Haider, J.; Khan, M.; Khan, Q.; Maqbool, M. Synthesis of nanomaterials using various top-down and bottom-up approaches, influencing factors, advantages, and disadvantages: A review. *Adv. Colloid Interface Sci.* **2022**, *300*, 102597. [CrossRef] [PubMed]
15. Caposciutti, G.; Tellini, B.; Saccomandi, P.; Cigada, A. Experimental analysis on the exploding wire process for nanopowder production: Influence of initial energy and exploding atmosphere. *Acta IMEKO* **2023**, *12* , 1–9. [CrossRef]
16. Liu, B.; Wang, D.; Guo, Y. Effect of Circuit Parameters and Environment on Shock Waves Generated by Underwater Electrical Wire Explosion. *IEEE Trans. Plasma Sci.* **2017**, *45*, 2519–2526. [CrossRef]
17. Suliz, K.; Kolosov, A.; Myasnichenko, V.; Nepsha, N.; Sdobnyakov, N.; Pervikov, A. Control of cluster coalescence during formation of bimetallic nanoparticles and nanoalloys obtained via electric explosion of two wires. *Adv. Powder Technol.* **2022**, *33*, 103518. [CrossRef]
18. Modena, M.M.; Rühle, B.; Burg, T.P.; Wuttke, S. Nanoparticle Characterization: What to Measure? *Adv. Mater.* **2019**, *31*, 1901556. [CrossRef]

19. Mourdikoudis, S.; Pallares, R.M.; Thanh, N.T.K. Characterization techniques for nanoparticles: Comparison and complementarity upon studying nanoparticle properties. *Nanoscale* **2018**, *10*, 12871–12934. [CrossRef] [PubMed]
20. Zimbone, M.; Calcagno, L.; Baeri, P.; Messina, G.; Compagnini, G. Dynamic light scattering in gold colloids prepared by laser ablation in water. *Appl. Surf. Sci.* **2012**, *258*, 9246–9249. EMRS 2011 Spring Symp J: Laser Materials Processing for Micro and Nano Applications. [CrossRef]
21. Midelet, J.; El-Sagheer, A.H.; Brown, T.; Kanaras, A.G.; Werts, M.H.V. The Sedimentation of Colloidal Nanoparticles in Solution and Its Study Using Quantitative Digital Photography. *Part. Part. Syst. Charact.* **2017**, *34*, 1700095. [CrossRef]
22. Mayani, M.G.; Herraiz Martínez, F.J.; Matanza Domingo, J.; Giannetti, R. Resonator-based Microwave Metamaterial Sensors for Instrumentation: Survey, Classification and Performance Comparison. *IEEE Trans. Instrum. Meas.* **2020**, *70*, 9503414. [CrossRef]
23. Prakash, D.; Gupta, N. Applications of metamaterial sensors: A review. *Int. J. Microw. Wirel. Technol.* **2022**, *14*, 19–33. [CrossRef]
24. Rajni.; Marwaha, A. An Accurate Approach of Mathematical Modeling of SRR and SR for Metamaterials. *J. Eng. Sci. Technol. Rev.* **2016**, *9*, 82–86. [CrossRef]
25. Vivek, A.; Shambavi, K.; Alex, Z.C. A review: Metamaterial sensors for material characterization. *Sens. Rev.* **2019**, *39*, 417–432. [CrossRef]
26. Mason, M.; Weaver, W. The Settling of Small Particles in a Fluid. *Phys. Rev.* **1924**, *23*, 412–426. [CrossRef]
27. Giorgi, F.; Macko, P.; Curran, J.M.; Whelan, M.; Worth, A.; Patterson, E.A. Settling dynamics of nanoparticles in simple and biological media. *R. Soc. Open Sci.* **2021**, *8*, 210068. [CrossRef]
28. Mergos, J.A.; Athanassopoulou, M.D.; Argyropoulos, T.G.; Dervos, C.T. Dielectric properties of nanopowder dispersions in paraffin oil. *IEEE Trans. Dielectr. Electr. Insul.* **2012**, *19*, 1502–1507. [CrossRef]
29. Wei, Z.; Huang, J.; Li, J.; Xu, G.; Ju, Z.; Liu, X.; Ni, X. A High-Sensitivity Microfluidic Sensor Based on a Substrate Integrated Waveguide Re-Entrant Cavity for Complex Permittivity Measurement of Liquids. *Sensors* **2018**, *18*, 4005. [CrossRef]
30. Peñaloza-Delgado, R.; Olvera-Cervantes, J.L.; Sosa-Morales, M.E.; Kataria, T.K.; Corona-Chávez, A. Dielectric characterization of vegetable oils during a heating cycle. *J. Food Sci. Technol.* **2021**, *58*, 1480–1487. [CrossRef] [PubMed]
31. Buckley, F.; Maryott, A.A. *Tables of Dielectric Dispersion Data for Pure Liquids and Dilute Solutions*; US Department of Commerce, National Bureau of Standards: Gaithersburg, MD, USA, 1958; Volume 589.
32. Alexander, C.M.; Dabrowiak, J.C.; Goodisman, J. Gravitational sedimentation of gold nanoparticles. *J. Colloid Interface Sci.* **2013**, *396*, 53–62. [CrossRef]
33. Utomo, A.; Alderman, N.J.; Padron, G.A.; Özcan Taşkın, N. Effects of particle concentration and dispersion rheology on the breakup of nanoparticle clusters through ultrasonication. *Chem. Eng. Res. Des.* **2023**, *191*, 301–312. [CrossRef]
34. Honrubia, M.M.; Domingo, J.M.; Herraiz-Martínez, F.J.; Giannetti, R. Low-Cost Electronics for Automatic Classification and Permittivity Estimation of Glycerin Solutions Using a Dielectric Resonator Sensor and Machine Learning Techniques. *Sensors* **2023**, *23*, 3940. [CrossRef]

CHAPTER 4

LOW-COST ELECTRONICS FOR AUTOMATIC CLASSIFICATION AND PERMITTIVITY ESTIMATION OF GLYCERIN SOLUTIONS USING A DIELECTRIC RESONATOR SENSOR AND MACHINE LEARNING TECHNIQUES

sensors

MDPI

Article

Low-Cost Electronics for Automatic Classification and Permittivity Estimation of Glycerin Solutions Using a Dielectric Resonator Sensor and Machine Learning Techniques

Miguel Monteagudo Honrubia *, Javier Matanza Domingo, Francisco Javier Herraiz-Martínez and Romano Giannetti *

Institute for Research in Technology, ICAI School of Engineering, Comillas Pontifical University, 28049 Madrid, Spain; jmatanza@iit.comillas.edu (J.M.D.); fjherraiz@icai.comillas.edu (F.J.H.-M.)
* Correspondence: mmonteagudo@comillas.edu (M.M.H.); romano.giannetti@iit.comillas.edu (R.G.)

Simple Summary: Glycerin is an organic substance used as an ingredient for many industries, including pharmaceuticals and cosmetics, but also, glycerin is an important product during biodiesel refining. Accurate and real-time sensors are needed to improve the industrial process; therefore, we proposed a workflow to measure concentrations of glycerin using a microwave sensor enhanced by machine learning models. We tested this methodology with complex electronic instrumentation and a designed low-cost portable electronic reader. As a result, we found that both devices achieved excellent and similar performance. These findings are valuable since monitoring the glycerin concentration may help to increase efficiency and reduce costs in the industry. In addition, the methodology proposed in this study could be applied to any sensor, making it a valuable contribution to liquid analysis with microwave sensors.

Abstract: Glycerin is a versatile organic molecule widely used in the pharmaceutical, food, and cosmetic industries, but it also has a central role in biodiesel refining. This research proposes a dielectric resonator (DR) sensor with a small cavity to classify glycerin solutions. A commercial VNA and a novel low-cost portable electronic reader were tested and compared to evaluate the sensor performance. Within a relative permittivity range of 1 to 78.3, measurements of air and nine distinct glycerin concentrations were taken. Both devices achieved excellent accuracy (98–100%) using Principal Component Analysis (PCA) and Support Vector Machine (SVM). In addition, permittivity estimation using Support Vector Regressor (SVR) achieved low RMSE values, around 0.6 for the VNA dataset and between 1.2 for the electronic reader. These findings prove that low-cost electronics can match the results of commercial instrumentation using machine learning techniques.

Keywords: dielectric resonator; microwave sensor; machine learning; dielectric characterization; glycerin purification; low-cost electronics; arduino

Citation: Monteagudo Honrubia, M.; Matanza Domingo, J.; Herraiz-Martínez, F.J.; Giannetti, R. Low-Cost Electronics for Automatic Classification and Permittivity Estimation of Glycerin Solutions Using a Dielectric Resonator Sensor and Machine Learning Techniques. *Sensors* **2023**, *23*, 3940. https://doi.org/10.3390/s23083940

Academic Editors: Cunjun Ruan, Tanveer Ul Haq and Bashar Ali Fraea Esmail

Received: 24 February 2023
Revised: 25 March 2023
Accepted: 4 April 2023
Published: 12 April 2023

1. Introduction

Pure glycerol, a colorless, odorless, viscous liquid with unique physical and chemical characteristics, is one of the most versatile organic molecules [1]. Glycerol can work as a humectant, sweetener, or even a solvent, and consequently, it is widely used in the pharmaceutical, food, and cosmetic industries. Moreover, glycerol is commonly used as a constituent or reactive element in synthesis reactions for the chemical industry [2,3]. In addition, glycerol is a crucial part of the structure of organic matter as the molecular base of fats or triglycerides, the main energy reservoir for animals and vegetables. However, pure glycerol is hard to extract and is usually diluted in water in a solution called glycerin, which is also soluble in alcohols. In contrast, it is insoluble in hydrocarbons and only partially soluble in many organic solvents.

On the other hand, crude glycerin (80%) is a primary by-product of biodiesel production from refined vegetable oils. Indeed, nowadays, this process is the principal source of pure glycerin (95–99%). However, the glycerin extracted must be separated and purified before being used for industrial applications [4]. Similarly, low-quality biodiesel due to inadequate purification involves some risk of critical engine issues, such as filter clogging or injector coking [5]. In conclusion, products with glycerin and biodiesel demand accurate and real-time sensing tools to characterize glycerin purity during refining. This paper aims to present a system for measuring glycerin solution permittivity with a Dielectric Resonator (DR) sensor excited by microwave signals created with off-the-shelf electronic components.

Microwave (MW) sensors are a cost-effective and adaptable solution for identifying and measuring substances. From an electronic point of view, MW sensors can be modeled as an RLC high-frequency circuit that functions as a notch filter with a high Q factor. These sensors are sensitive to changes in capacitance, leading to a shift in the resonance frequency [6]. The effective permittivity of the medium surrounding the DR is intimately related to the resonator capacitance. In sum, the DR is an indirect detector for substances with permittivity values greater than air, which is usually the reference medium [7]. This study aimed to detect changes in glycerin concentration by observing the effect on the DR resonance frequency, as each solution has a distinct complex permittivity value.

One of the main advantages of DR sensors is their straightforward fabrication, as they are usually made of a bulk dielectric material with a regular geometry, most commonly cylindrical. The material's physical dimensions and relative permittivity tune its resonance behavior over a narrow frequency range [8]. In addition, a DR is an ideal MW radiating device with minimum conduction losses and high radiation efficiency on a 3D surface [9]. Moreover, DR sensors are an attractive choice for developing low-cost detection devices since they could be fully passive, avoiding the requirement of batteries to feed the sensor [10]. Other resonant technologies have been proposed for sensing liquids in the microwave region. In particular, split-ring resonators are the most popular sensors, as reported in several reviews in the last few years [7,11,12]. However, these technologies are primarily planar designs generally oriented for microfluidic or submersion applications since managing fluids demands a specific configuration. Therefore, a cylindrical DR with a small cavity for drop measurements could be a solid and practical alternative for liquid analysis.

Sensor calibration is crucial for obtaining accurate and valuable results. This process establishes a correlation between the DR sensor signal and the expected measurement value. Conventional calibration, which involves compiling a measurement dataset, selecting relevant variables, and performing statistical analysis [13], presents challenges and drawbacks that machine learning (ML) can address [14]. ML, a subfield of artificial intelligence, focuses on identifying complex patterns within data and then applying that knowledge to make predictions. The power of ML models to detect correlations inside these data has the potential to enhance sensor performance, especially in cases with a nonlinear relationship between the analyzed process and the signal acquired [15]. For example, in this research study, the permittivity of binary mixtures follows a double Debye model since each solution component has a unique dielectric relaxation [16]. In addition, the calibration based on fixed parameters, such as resonance frequency, is less optimal and may introduce bias or variance, reducing the sensor's performance since these parameters are not the complete signal information. In contrast, machine learning models pursue a balanced trade-off between variance and bias by considering the complete signal information. Our objective is to improve the sensitivity of DR sensors by applying ML techniques. We also aim to create a real-time sensing system capable of automatically detecting slight variations in permittivity, enabling us to determine the composition of the glycerin solution.

However, all the advantages of DR sensors are strongly reduced due to the electronic instrumentation systems for high-frequency measurements. For example, a Vector Network Analyzer (VNA) requires a high economic investment but also demands qualified

personnel and complex calibration, and its bulky size hinders its use for automatic real-time measurements in industrial environments. In addition, the cost and complexity of high-end equipment diminish the market penetration of on-site analytical devices in other fields, such as environmental research [17] or diagnostic devices for point-of-care strategies [18], where DR sensors could be the base of numerous applications. It must be noted that these limitations have a more severe impact on low-income countries, where the need for low-cost sensors is more acute [19]. Therefore, it is necessary to reduce the cost and increase the portability of the electronic equipment to interface with DR sensors. In recent years, the development of the Internet of Things and the enthusiasm for open-source hardware and software have opened many possibilities for developing low-cost electronics using microcontrollers or microcomputers such as Arduino or Raspberry Pi [20]. These boards allow I/O control of signals within an embedded system. While commercial devices give strict specifications, open-hardware designs have the inherent advantage of customization, allowing the device to adapt to the needs of the analytical objective. We propose using an Arduino microcontroller and economic MW components to replace the VNA measurements at a more reasonable price but with comparable performance.

2. Materials and Methods

This section provides a comprehensive description of each step of the DR sensor workflow (Figure 1). First, the DR overview and the experimental setup are presented, with a specific subsection explaining our novel electronic reader components and their functioning. Afterward, the data collection is described, including the measurement protocol and sample selection process. Finally, this section briefly introduces the ML learning techniques employed, with their respective parameters.

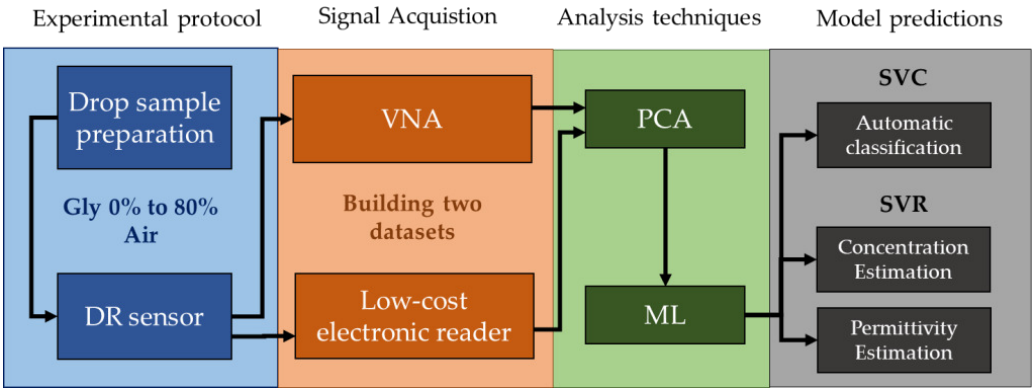

Figure 1. Summary of the experimental workflow.

2.1. DR Sensor Overview

The authors presented the DR sensor used in these experiments in a previous study involving the liquid characterization of water-ethanol binary mixtures [6]. As depicted in Figure 2, the DR design has a cylindrical structure with a radius d_{dr} = 34 mm and height h = 8 mm, fabricated using zirconia, a ceramic material with high relative permittivity, ε_r = 29, and minimal conduction losses. A small cylindrical analysis chamber is placed on the DR top for drop measurements. The sensor is fed through a microstrip transmission line (TL) adjusted to 50 Ω and connected to an SMA port. An optimized rectangular slot was etched on the ground plane to maximize energy transmission and achieve excellent coupling efficiency.

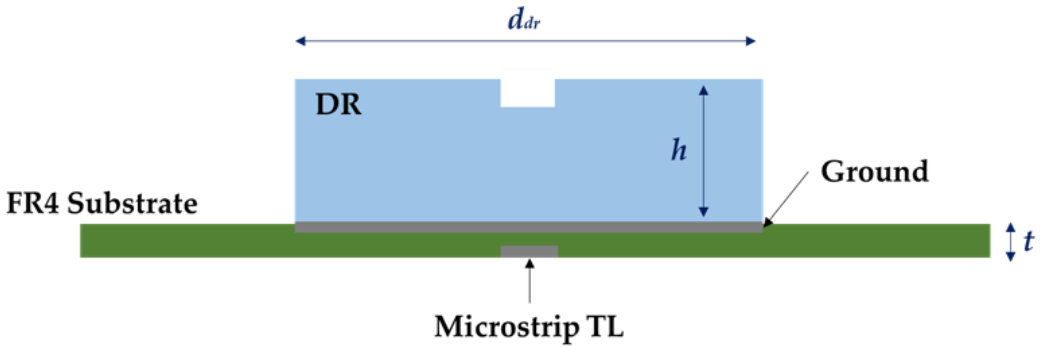

Figure 2. DR sensor scheme showing the sensor placement on the ground to achieve the coupling between the DR and the Microstrip TL.

Additionally, a polycarbonate frame was used to fix the DR to the FR4 fiberglass substrate (ε_r = 4.4, t = 1.55 mm) to enable coupling stability and measurement reproducibility (Figure 3). The fundamental HEM_{110} mode is excited inside the DR with a theoretical resonance frequency related to the physical dimensions and material permittivity (1) [6]. Simulation results and experimental observations determined that the DR resonance frequency on air is 2.473 GHz. The frequency shift is due to the interaction between the electromagnetic fields inside the DR and the liquid sample inside the analysis chamber, as defined by the perturbation theory [21].

$$(f_r)_{110} = \frac{c}{2r_{dr}\pi\sqrt{\epsilon_r}}\left(1.71 + \frac{r_{dr}}{h} + 1.578\left(\frac{r_{dr}}{2h}\right)^2\right) \quad (1)$$

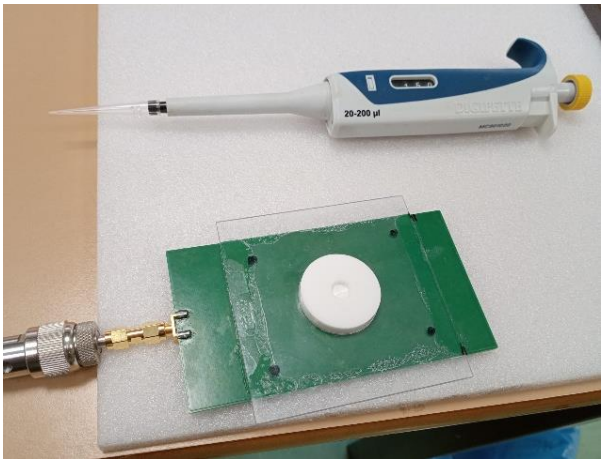

Figure 3. Experimental setup for the DR sensor with a polycarbonate supporting frame and the SMA connection to the VNA port.

2.2. Electronic Instrumentation: From Vector Network Analyzer to Low-Cost Detection Devices

The main objective of this research study was to compare the DR sensor performance of an electronic instrumentation device and a novel electronic reader made with low-cost components. First, the spectra were obtained using the Anritsu MS46122B VNA calibrated in the frequency range of 2.25–2.55 GHz and with a sampling buffer of 5000 points. The 1-port mode configuration was employed to obtain the reflection coefficient |s11| and frequency values for the ML analysis. The VNA measures established a results baseline to compare with our designed portable electronic reader and validate its performance. The electronic reader is an improved design from previous research [22]. Figure 4 shows the electric circuit with the control, conditioning, and MW sensing modules. An Arduino MKR WiFi 1010 is the base for the control module for signal generation and acquisition.

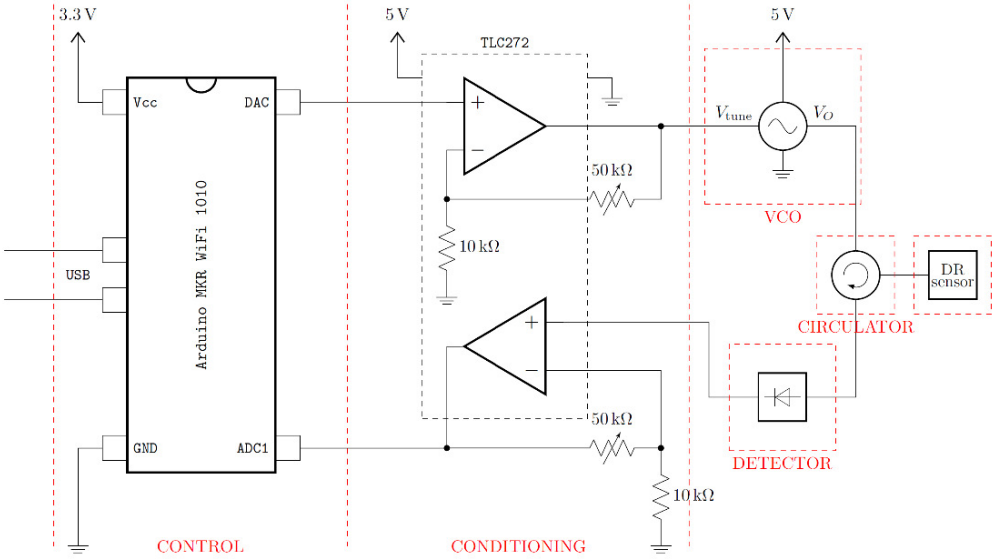

Figure 4. Electric circuit diagram of the electronic reader with all the components involved in the signal acquisition. This design is divided into three parts: control, conditioning, and MW sensing.

The Arduino DAC generates a sweeping triangular signal (v_1 in Figure 5), which is transmitted to the VCO (Minicircuits ZX95-2536C-S+) through a reconditioning circuit to adapt the input voltage for tuning the output MW signal within the 2.25–2.55 GHz range (v_2 in Figure 5). The VCO is connected to a circulator (UiY CC2528A2400T2500SF) to manage the signal direction. Afterward, the MW signal is transmitted to the DR sensor by the SMA port. Similar to the VNA acquisition, the DR sensor works in reflection: the circulator receives back the reflected MW signal (v_3 in Figure 5) and then transmits the signal to the amplification circuit to increase voltage resolution. Finally, the measured signal is transmitted to the power detector and then to the Arduino, which digitalizes the signal converting the power values into voltage units by timestamp (v_4 in Figure 5). It must be noted that the VNA acquires a unique frequency sweep, while the electronic reader records a signal with several sweeps in the time domain. In addition, each electronic reader signal for the same glycerine concentration will be desynchronized, adding variance to the dataset.

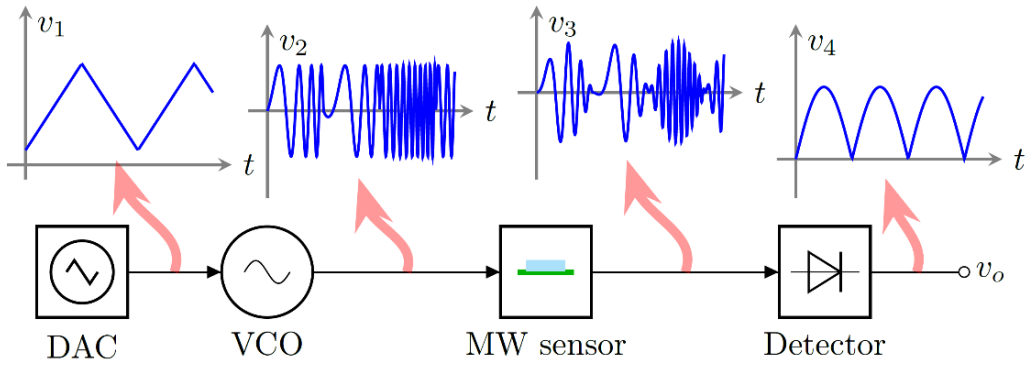

Figure 5. Signal transformation along the electronic reader workflow: v_1 triangular signal from the DAC, v_2 frequency sweep from the VCO, v_3 reflected signal by the MW sensor, v_4 acquired signal by the Arduino ADC.

2.3. Measurement Protocol

The experiments were performed with air and glycerin solutions that varied from 0% to 80% in 10% intervals (Table 1). Higher concentrations, such as 90% or pure glycerin (99%), were not included in the dataset as they were too viscous to ensure the accurate volume with a micropipette. The measurements were obtained by filling the resonator cavity with a 150 µL volume sample. The resulting VNA dataset includes 100 spectra

acquired for each solution, while the electronic reader dataset contains 180 signals for every solution obtained from 35 drop samples with five-six repetitions each, with six seconds of delay in between. All signals acquired are available in a GitHub public repository (https://github.com/MigMH/VNA_ER_GlycerinSolutions accessed on 3 April 2023).

Table 1. List of glycerin solutions tested with their relative permittivity values at 20–21 °C.

	ε_r Maxwell–Garnett Mixing Rule	ε_r Literature
Air	1	1
Gly80%	11.17	17.00
Gly70%	13.72	27.45
Gly60%	16.83	39.00
Gly50%	20.72	51.55
Gly40%	25.71	58.78
Gly30%	32.34	65.25
Gly20%	41.61	69.23
Gly10%	55.43	74.32
Water	78.30	78.30

The relative permittivity values for the selected glycerin concentration were extracted from [23] in the 2.25–2.55 GHz frequency range at 21 °C, varying from 17 to 74.32. In contrast, the permittivity value for pure water is 78.3 at 20 °C [24]. In order to validate these experimental results, the permittivity of each solution was estimated using the Maxwell–Garnett Mixing Rule (2), where ε_{sol} and ε_{wat} are the dielectric constants of solvent and water, respectively, and |m| is the volumetric fraction of the solvent solution in water [25]. Both permittivity values are drastically different (Table 1); a priori, it is not feasible to determine if the formula fits these experimental data or if this data is accurate. Unfortunately, to the author's knowledge, there are no more references for this glycerin concentration in the frequency working range. Moreover, other authors [26] measured the same concentrations with a differential microwave sensor using the same reference permittivity values but at 1.56 GHz. Therefore, as a side objective, this article aims to use the VNA and our low-cost electronic reader to test which permittivity values fit better with the ML models.

$$\epsilon_{eff} = \epsilon_{sol} + 3|m|\epsilon_{sol}\frac{\epsilon_{wat} - \epsilon_{sol}}{\epsilon_{wat} + 2\epsilon_{sol} - |m|(\epsilon_{wat} - \epsilon_{sol})} \rightarrow |m| = \frac{V_{sol}}{V_{wat}} \quad (2)$$

2.4. Analysis Techniques

Implementing ML models demands feature reduction methods due to the high dimensionality of the obtained spectral data. For this reason, Principal Component Analysis (PCA) is employed, a statistical algorithm that identifies the directions of maximum variability within the data structure and generates a new mathematical space where each spectrum is projected while retaining essential information [27]. Each spectrum is defined by a vector in the principal components obtained from PCA [28], and this vector serves as the input feature for an ML model. The next step was labeling these data with their corresponding class to perform supervised learning; several models were tested in a preliminary study, such as Random Forest or XGBoost, but Support Vector Machine (SVM) achieved slightly better performance. This algorithm traces a hyperplane in the data space to classify each sample, and it is calculated to maximize the separation between classes [29]. The support vectors are the closest data points of each class to the decision boundary, and since SVM only requires a small number of support vectors to define the hyperplane, it is a reliable method for working with small datasets [30]. This is a considerable advantage since acquiring a huge dataset is significantly time-consuming. In addition, SVM is a versatile model, and it can be used for regression as well as classification; in this case, the model prediction is an estimate of permittivity. The SVM hyperparameters were chosen using Bayesian optimization: C, which defines the hyperplane exclusion margin, and γ, which regulates the influence distance of a single training point (Table 2). Finally, in or-

der to prevent overfitting, the dataset was divided into a training set (70%) and a test set (30%). The K-fold Cross-Validation method was applied during the model training with k = 5 folds [31].

Table 2. ML models hyperparameters for the VNA and the electronic reader (ER).

Model	C	γ
VNA Classification	2620	0.00087
VNA Regression glycerin (%)	4000	0.01224
VNA Regression mixing rule values	4000	0.01362
VNA Regression literature values	4540	0.01243
ER Classification	4197	0.00100
ER Regression glycerin (%)	10,000	0.00323
ER Regression mixing rule values	9357	0.00623
ER Regression literature values	8247	0.00288

3. Results and Discussion

The main purpose of this section is to compare the ML performance comparison between the datasets acquired by the VNA and by our low-cost electronic reader. Firstly, we analyze the signal characterization of each device, with different glycerin solutions. Secondly, we show how the information within these signals is condensed and projected using PCA to improve the interpretation. Thirdly, we evaluate and compare the performance of ML models for the automatic classification of each glycerin concentration. Finally, we estimate the solution permittivity and validate the results with two different sources: the experimental data from [23] and the Maxwell–Garnett mixing rule.

3.1. Signal Characterization

The average spectra of each solution in Figure 6 indicate drastic resonance frequency changes. Lower glycerin concentrations result in a reduction in the resonance frequency since the higher volume of water increases the solution permittivity. As glycerin concentration increases, the maximum $|s_{11}|$ amplitude rises until Gly40%, which approaches the value of air. Beyond this concentration, the $|s_{11}|$ amplitude gradually decreases. This change could be related to the complex interaction between the dielectric relaxation of glycerol and water. Given that the loss factor affects the resonance amplitude, the DR sensor might actually be measuring complex permittivity. Further research using alternative dielectric characterization methods would help to acquire a reliable reference to compare with our sensor results.

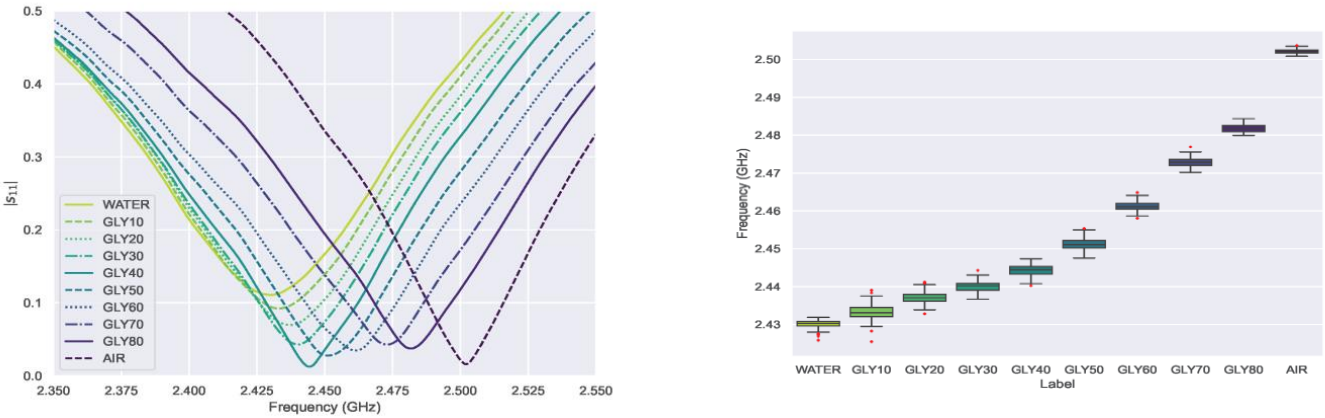

Figure 6. VNA average signals (**left**) and boxplot of the resonance peak distribution (**right**) for each glycerin concentration.

The resonance peak distribution was analyzed with a boxplot, where the average value and the dispersion for each concentration can be easily compared. Figure 6 shows a

minor overlap between the low glycerin concentrations, which diminishes as the water volume fraction decreases. Indeed, with concentrations of 40% glycerin and above, each class peak distribution is entirely isolated. Compared to the previous study of this DR design with water-ethanol solutions [6], the variance in the concentration has been drastically reduced thanks to improvements in the setup and the measurement protocol. According to these findings, neither the solution permittivity nor the frequency shift (Figure 7) evolves linearly, in accordance with both the Maxwell–Garnett Mixing Rule and the data extracted from [23] (Table 1). The resonance behavior of the sensor itself is another factor that helps to explain this resonance peak distribution; since the resonance frequency shift is a non-linear function of permittivity. As shown in Figure 7, the frequency shift is more pronounced when the solution permittivity is closer to the reference ($\varepsilon_r = 1$); in other words, the shift increment reduces as the glycerin concentration rises. Both factors seem to impact the frequency shift significantly and must be considered for future research, especially with low glycerin concentrations. These effects are far less significant in high concentrations, such as crude glycerin from biodiesel refining. Other authors in [26] propose a differential microwave sensor for the same glycerin concentrations, but their results are hardly comparable since the sensor design is entirely different and relies on a microfluidic channel with a pumping system. Although they achieve good sensitivity, their measurements are based solely on one parameter, the amplitude change in differential signal $|s^{DC}{}_{11}|$. The purpose of this paper is not to limit the sensor sensitivity analysis to a single parameter, the resonance peak shift, but to apply ML to study how the whole signal is affected. Given that the sensitivity is not a constant since it depends on the resonators' non-linear behavior, the accuracy of the ML models would represent a more useful indicator of the DR sensing capability.

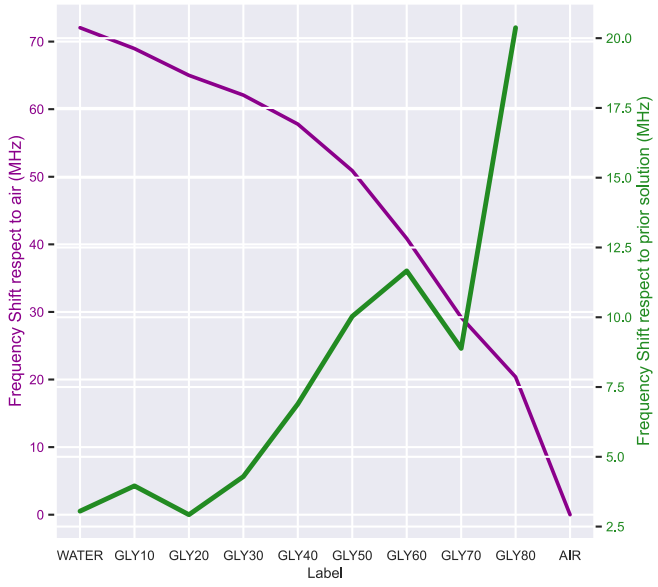

Figure 7. Frequency shift variation with respect to the air reference value (purple) and with respect to the previous glycerin concentration (green). The trend is non-linear since the frequency shift is more significant for values close to air and more uniform for values close to water.

The periodic signal by the electronic reader resembles a rectified sum of two sinusoidal waves. It shows clear differences when the glycerin concentration changes (Figure 8), but the interpretation is less intuitive than the case of VNA spectra, where the concentration can be guessed by looking at the peak frequency shift. Nevertheless, it is possible to spot a pattern; one of the waves has practically vanished in the air signal but is increasing with the glycerin concentration, reaching the maximum for water. Therefore, this wave corresponds to lower frequencies closer to the 2.25 GHz margin detected by the reader (Figure 6). The second wave diminishes from its maximum in the air until remaining steady around Gly 40%; thus, this wave corresponds to higher frequencies around the

2.55 GHz margin. However, all the voltage amplitude changes are particularly subtle between glycerin solutions with similar concentrations. Consequently, the electronic reader signals would be less helpful in analyzing glycerin solutions without applying PCA or ML.

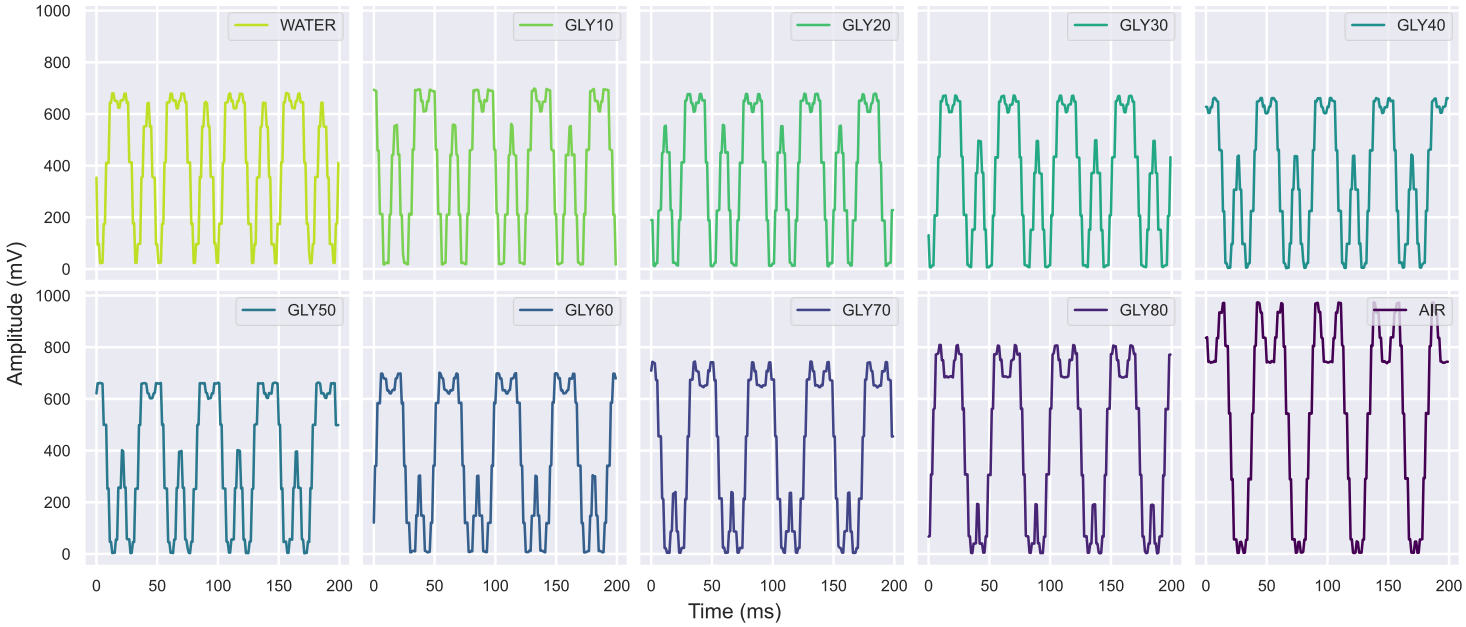

Figure 8. The electronic reader signals examples for each glycerin concentration and air.

3.2. Principal Component Analysis (PCA)

Only two principal components were required for the PCA to condense 99% of the information within the VNA spectra data. Since the PCA projects the signals into an abstract space, its explainability is typically low. However, in this case, the PCA plot for the VNA reveals discrete and separate clusters in what seems to be a concentration curve (Figure 9). When using PCA, the whole signal is considered rather than just the resonance peak. Therefore, it is simple to distinguish between each glycerin solution without the minor overlap mentioned before in the boxplot analysis (Figure 6). In conclusion, the PCA increases the class separability of these spectral data by reducing data dimensions.

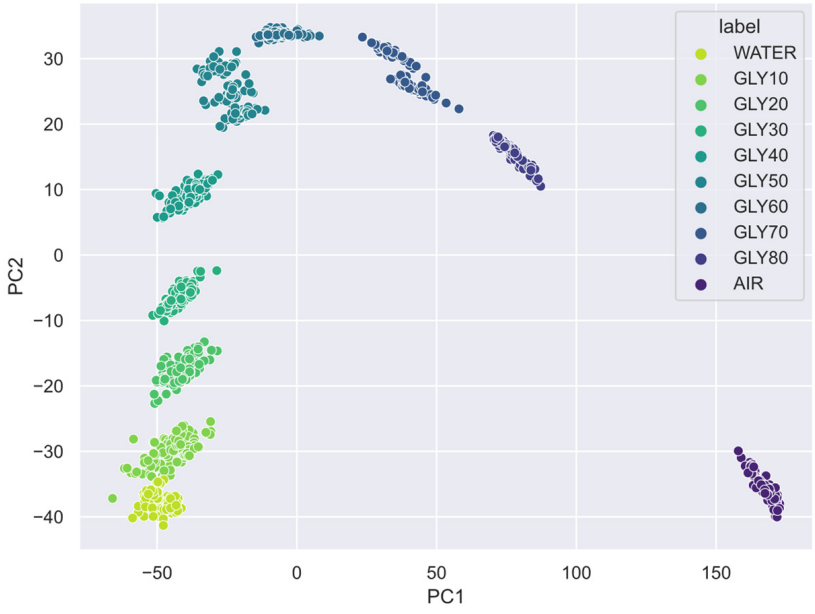

Figure 9. PCA scatter plot of the VNA spectra.

Because the electronic reader generates desynchronized periodic signals, the PCA demands seven principal components to reach 97% of the explained variance, as opposed to the PC required by the VNA. VNA projections show clear and distinct clusters (Figure 9), while the electronic reader projects circular patterns (Figure 10). In particular, the PC1-PC2 plot shows a projection grouped in concentric circles, each corresponding to a glycerin concentration, in what appears to be a graduation of permittivity. It must be noted that the class separability reaches its maximum when considering all the dimensions at once. For example, the PC1-PC7 plot extends the graduation in another dimension where the solution differences are incremented. In summary, both acquisition methods show good class separability in the PCA plots that anticipate positive results in the ML models. For this reason, the lack of synchronization is very useful to add variability in the model learning since it reduces bias, but at the cost of increasing the complexity of the SVM model.

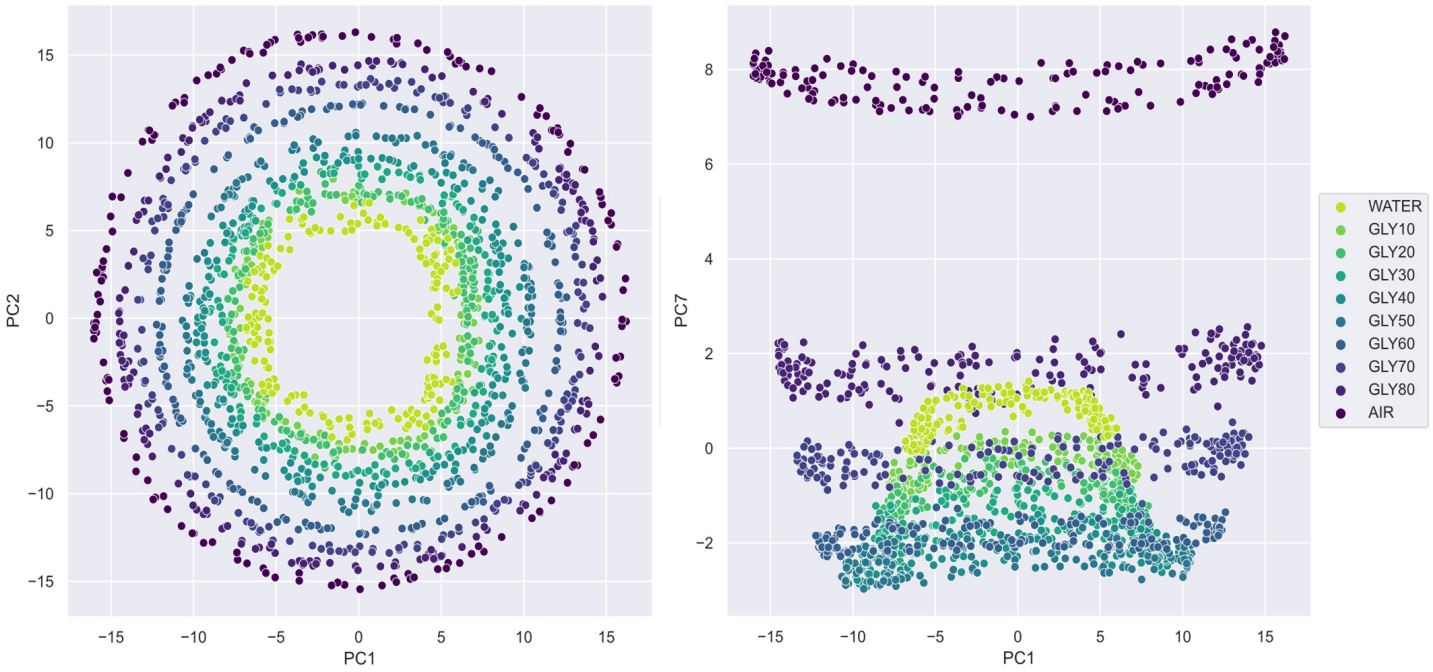

Figure 10. PCA scatter plots of ER signals.

3.3. Glycerin Classification

The SVM classification model achieved excellent accuracy (around 97–99%) for both the VNA and the electronic reader (Table 3), in accordance with the insights from the PCA. The confusion matrixes in Figure 11 show barely any contamination between classes. In contrast, the regression models show some performance differences between both acquisition methods; the Root Mean Squared Error (RMSE) for the electronic reader is between two and three times bigger than the VNA (Table 3). To the author's knowledge, there are no similar experiments measuring glycerin concentration with dielectric resonators or automatic classification of substances with microwave sensors. However, recent ML applications for electrochemical and optical biosensors using PCA and SVM have shown results in accordance with this research [14]. Therefore, these findings reinforce the value of DR sensors and ML models for classifying glycerin solutions.

3.4. Permittivity Estimation

The glycerin concentrations are labeled as discrete values for the SVM classification model. However, the Support Vector Regressor (SVR) can be employed to estimate the glycerin as a continuous variable after relabeling the training dataset and removing the air samples. The model performance is almost perfect for the VNA with an RMSE of 0.70% and highly favorable for the electronic reader with an RMSE of 1.93% (Table 3). The boxplot comparison between both devices in Figure 12 shows that the VNA permittivity es-

timations fit the real concentration almost perfectly: the box is almost a flat line, and the primary source of RMSE is some outliers. In contrast, the electronic reader estimations are more scattered around the original value since the variance is greater, especially with glycerin concentrations from 10% to 40%. This result concurs with the PCA plots from the electronic reader (Figures 9 and 10), where the distance between these concentrations is minimal. As previously stated, the DR sensor's non-linear response could reduce sensitivity when the permittivity sample is significantly higher than air permittivity, as occurs with low glycerin concentrations. However, for concentrations greater than 40%, the electronic reader performance is more precise and similar to the VNA performance.

Table 3. ML performance results.

Models	VNA Accuracy	ER Accuracy
SVM	99.33%	97.41%
	VNA RMSE	**ER RMSE**
SVR Glycerin (%)	0.70%	1.93%
SVR mixing rule values	0.629	2.091
SVR literature values	0.599	1.119

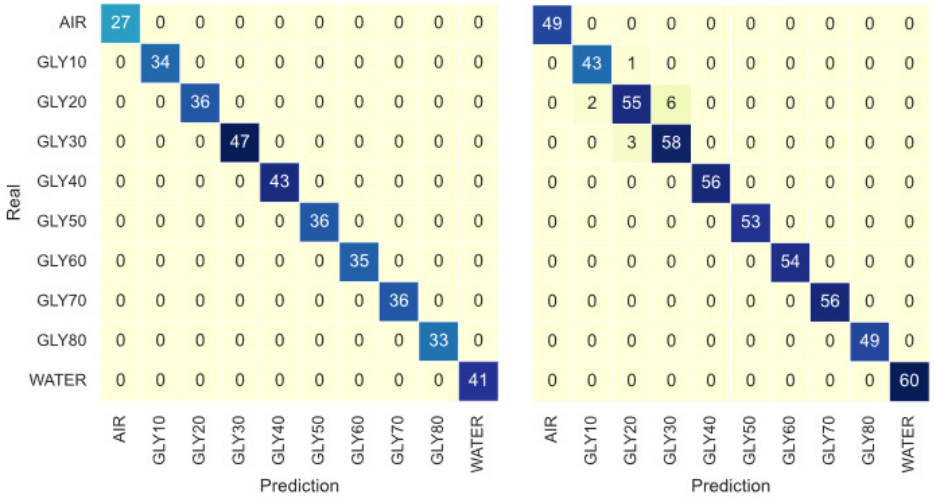

Figure 11. Confusion Matrix for the SVM classification model for the VNA signals (**left**) and Electronic Reader signal (**right**).

Additionally, two further SVR models were trained to estimate solution permittivity rather than glycerin concentration. Each model was trained with two permittivity sources: the Maxwell–Garnett Mixing Rule [25] and the values acquired by dielectric spectroscopy from the literature [23] (Table 1). The VNA achieved excellent and identical performance with an RMSE close to 0.60 (Table 3) for both permittivity sources (Figures 13 and 14). However, the VNA dataset hinders the evaluation of the reliability of both permittivity sources since the excellent class separability helps the SVR models estimate the solution permittivity independently of the value distribution.

On the other hand, the electronic reader is less precise and more sensitive to perturbations; therefore, both SVR models show distinct estimation patterns. First, the estimations based on the Maxwell–Garnett mixing rule are almost perfect for low permittivity values, while for high permittivity, the error is drastically increased (Figure 13). This contrasts clearly with the SVR model trained with the permittivity values from [23] since these estimations have a more uniform error distribution by class (Figure 14), which are comparable to the VNAs in all the permittivity ranges. This difference is reflected in the RMSE, 1.119 for the literature SVR model and 2.091 for the Maxwell–Garnett mixing rule SVR model. In sum, the experimental values seem correct but may be affected by minor experimental errors. In contrast, the Maxwell–Garnett mixing rule, which is commonly used to estimate

the permittivity of composite materials with inclusions [32], is probably not optimal for liquid mixtures. This result indicates that the combination of the electronic reader and SVR models is a good method to evaluate the reliability of mixing formulas or experimental dielectric characterization.

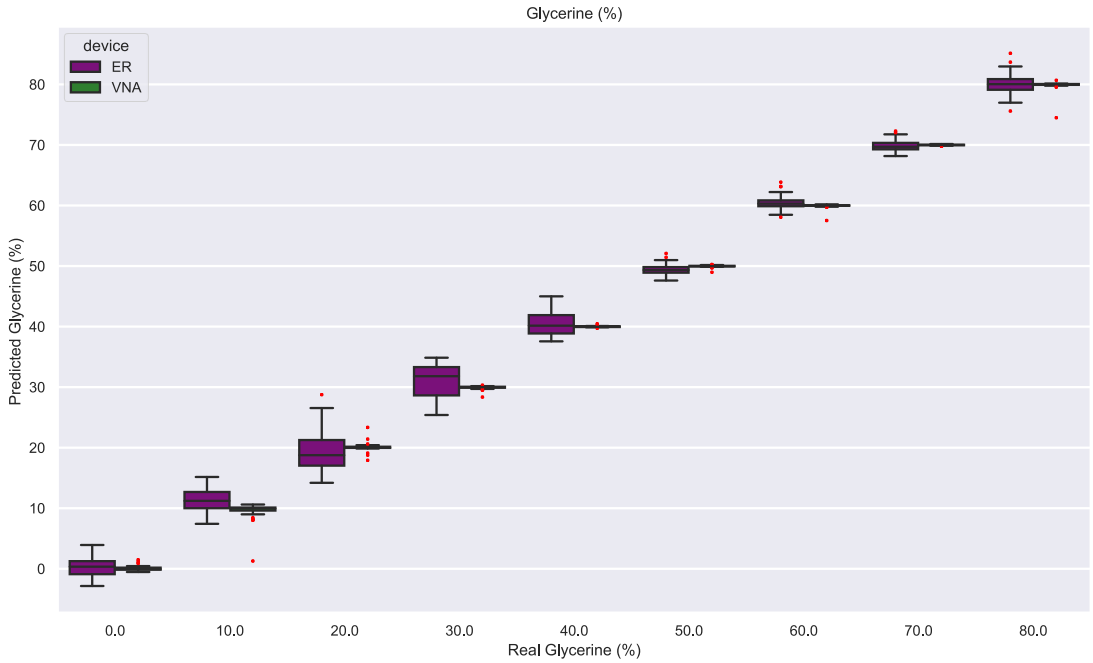

Figure 12. Regression model predictions for glycerin (%).

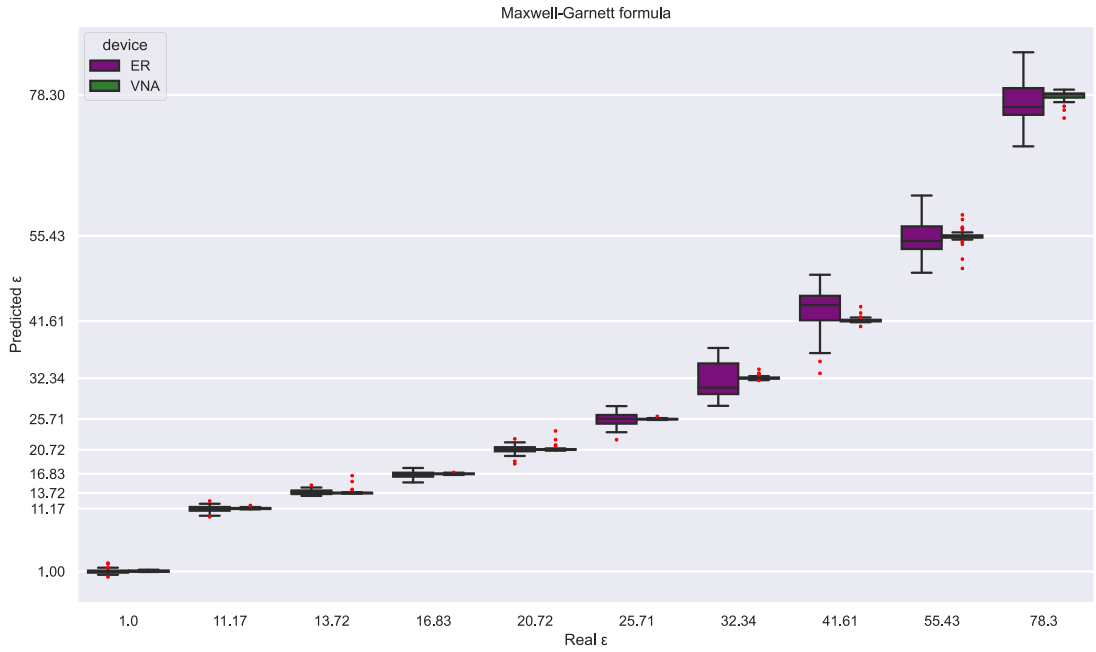

Figure 13. Permittivity estimations for both devices from an SVR model trained with the permittivity values from the Maxwell–Garnett mixing rule.

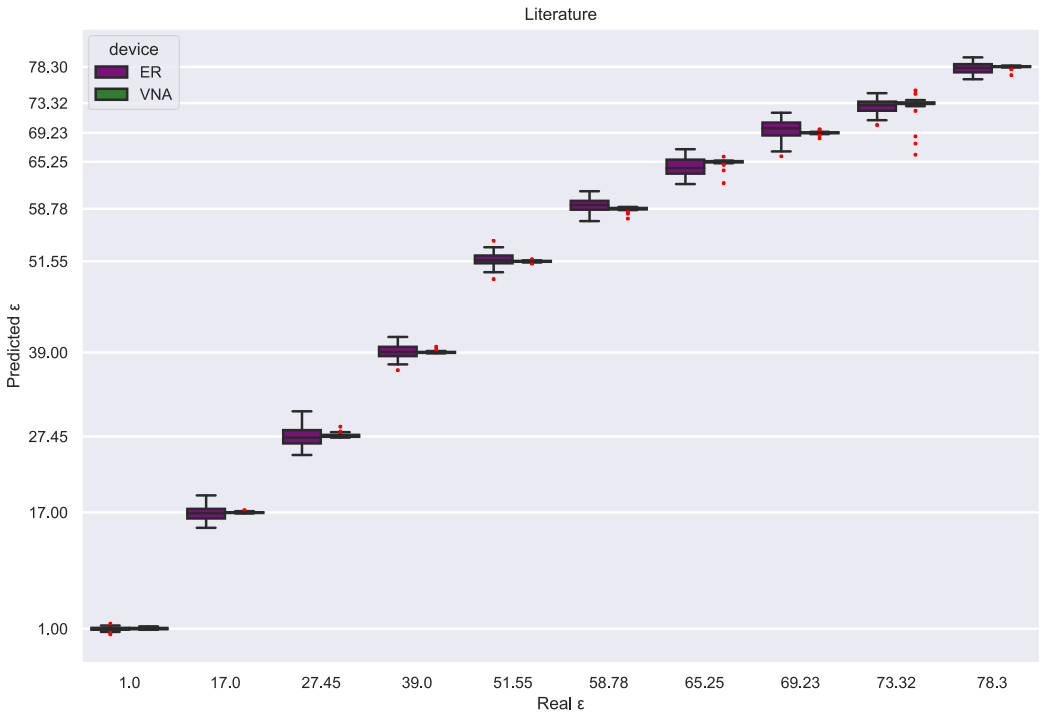

Figure 14. Permittivity estimations for both devices from an SVR model trained with the permittivity values found in the literature [23].

4. Conclusions

This study proposed using a dielectric resonator (DR) sensor to determine glycerin solution concentration. A commercial VNA was used to establish a benchmark for the sensor performance and, thus, validate our designed electronic device. Measurements of air and nine different glycerin concentrations were taken within a relative permittivity range of 1 to 78.3. Using Support Vector Machine (SVM) and Principal Component Analysis (PCA), both devices obtained outstanding accuracy (98–100%). Additionally, permittivity estimation using the Support Vector Regressor (SVR) accomplished low RMSE values between 0.6 and 1.2. These results prove that by applying ML with the proposed workflow (Figure 1), low-cost portable electronics can achieve comparable results to complex electronic instrumentation equipment. This significant contribution opens many opportunities for future developments since this workflow is not limited to our DR design and could be applied to any sensor. These findings also emphasize the DR sensor's capacity to generate accurate permittivity estimations. Consequently, if the SVM model is trained with the correct permittivity data, it could estimate the permittivity of any liquid inside its cavity chamber. Moreover, this methodology is able to validate any permittivity characterization, including mixing formulas, which we consider critical since there is a lack of dielectric characterization data for many sensing applications, especially if the sensor work in a narrow frequency range. In conclusion, the designed DR sensor and the workflow proposed is a promising combination for crude glycerin analysis in all sectors where glycerin is required. ML models offer a precise method for analyzing the sensor inputs, making them the ideal support technology for the DR sensor. In future works, this methodology will be adapted to new analytical targets and expanded to reach the full potential of this technology.

Author Contributions: Conceptualization, M.M.H., F.J.H.-M., J.M.D. and R.G.; Methodology, M.M.H.; Formal analysis, M.M.H.; Investigation, M.M.H.; Writing—original draft, M.M.H.; Writing—review & editing, F.J.H.-M., J.M.D. and R.G.; Supervision, F.J.H.-M., J.M.D. and R.G.; Project administration, F.J.H.-M., J.M.D. and R.G.; All authors have read and agreed to the published version of the manuscript.

Funding: This work has been funded by "IIT Strategic PhD Research Grants" by Comillas Pontifical University, Madrid, Spain.

Institutional Review Board Statement: Not applicable.

Informed Consent Statement: Not applicable.

Data Availability Statement: All signals acquired are available in a GitHub public repository (https://github.com/MigMH/VNA_ER_GlycerinSolutions accessed on 3 April 2023).

Acknowledgments: The authors would like to express their thanks to Christopher Michael Turner for proofreading and suggesting valuable insights about the writing.

Conflicts of Interest: The authors declare no conflict of interest.

References

1. Pagliaro, M.; Rossi, M. Chapter 1 Glycerol: Properties and Production. In *The Future of Glycerol (2)*; The Royal Society of Chemistry: London, UK, 2010; pp. 1–28. ISBN 978-1-84973-046-4.
2. Reck, R.A. Other Applications of Glycerine. In *Glycerine*; CRC Press: Boca Raton, FL, USA, 2018; pp. 435–442.
3. Mast, R. Functions of Glycerine in Cosmetics. In *Glycerine*; CRC Press: Boca Raton, FL, USA, 2018; pp. 223–275.
4. Maquirriain, M.A.; Tonutti, L.G.; Querini, C.A.; Pisarello, M.L. Crude Glycerine Characterization: Analysis of Free Fatty Acids, Fatty Acid Methyl Esters, and Acylglycerides. *Biomass. Convers. Biorefin.* **2022**, *12*, 4889–4899. [CrossRef]
5. Bateni, H.; Saraeian, A.; Able, C.; Karimi, K. *Biodiesel Purification and Upgrading Technologies*; Springer: Cham, Switzerland, 2019; pp. 57–100.
6. Mayani, M.G.; Herraiz-Martinez, F.J.; Domingo, J.M.; Giannetti, R.; Garcia, C.R.M. A Novel Dielectric Resonator-Based Passive Sensor for Drop-Volume Binary Mixtures Classification. *IEEE Sens. J.* **2021**, *21*, 20156–20164. [CrossRef]
7. Mayani, M.G.; Herraiz-Martinez, F.J.; Domingo, J.M.; Giannetti, R. Resonator-Based Microwave Metamaterial Sensors for Instrumentation: Survey, Classification, and Performance Comparison. *IEEE Trans. Instrum. Meas.* **2021**, *70*, 1–14. [CrossRef]
8. Keyrouz, S.; Caratelli, D. Dielectric Resonator Antennas: Basic Concepts, Design Guidelines, and Recent Developments at Millimeter-Wave Frequencies. *Int. J. Antennas. Propag.* **2016**, *2016*, 6075680. [CrossRef]
9. Dash, S.K.K.; Khan, T.; Antar, Y.M.M. A State-of-Art Review on Performance Improvement of Dielectric Resonator Antennas. *Int. J. RF Microw. Comput.-Aided Eng.* **2018**, *28*, e21270. [CrossRef]
10. Mehrotra, P.; Chatterjee, B.; Sen, S. EM-Wave Biosensors: A Review of RF, Microwave, Mm-Wave and Optical Sensing. *Sensors* **2019**, *19*, 1013. [CrossRef] [PubMed]
11. Muñoz-Enano, J.; Vélez, P.; Gil, M.; Martín, F. Planar Microwave Resonant Sensors: A Review and Recent Developments. *Appl. Sci.* **2020**, *10*, 2615. [CrossRef]
12. Alahnomi, R.A.; Zakaria, Z.; Yussof, Z.M.; Althuwayb, A.A.; Alhegazi, A.; Alsariera, H.; Rahman, N.A. Review of Recent Microwave Planar Resonator-Based Sensors: Techniques of Complex Permittivity Extraction, Applications, Open Challenges and Future Research Directions. *Sensors* **2021**, *21*, 2267. [CrossRef]
13. Tanwar, S.; Nayyar, A.; Rameshwar, R. *Machine Learning in Signal Processing : Applications, Challenges, and the Road Ahead*; Chapman and Hall/CRC: New York, NY, USA, 2021.
14. Cui, F.; Yue, Y.; Zhang, Y.; Zhang, Z.; Zhou, H.S. Advancing Biosensors with Machine Learning. *ACS Sens.* **2020**, *5*, 3346–3364. [CrossRef]
15. Singh, A.; Sharma, A.; Ahmed, A.; Sundramoorthy, A.K.; Furukawa, H.; Arya, S.; Khosla, A. Recent Advances in Electrochemical Biosensors: Applications, Challenges, and Future Scope. *Biosensors* **2021**, *11*, 336. [CrossRef] [PubMed]
16. Havelka, D.; Krivosudský, O.; Průša, J.; Cifra, M. Rational Design of Sensor for Broadband Dielectric Spectroscopy of Biomolecules. *Sens. Actuators B Chem.* **2018**, *273*, 62–69. [CrossRef]
17. Chan, K.; Schillereff, D.N.; Baas, A.C.W.; Chadwick, M.A.; Main, B.; Mulligan, M.; O'Shea, F.T.; Pearce, R.; Smith, T.E.L.; van Soesbergen, A.; et al. Low-Cost Electronic Sensors for Environmental Research: Pitfalls and Opportunities. *Prog. Phys. Geogr.* **2021**, *45*, 305–338. [CrossRef]
18. Heidt, B.; Siqueira, W.F.; Eersels, K.; Diliën, H.; van Grinsven, B.; Fujiwara, R.T.; Cleij, T.J. Point of Care Diagnostics in Resource-Limited Settings: A Review of the Present and Future of PoC in Its Most Needed Environment. *Biosensors* **2020**, *10*, 133. [CrossRef] [PubMed]
19. Pai, N.P.; Vadnais, C.; Denkinger, C.; Engel, N.; Pai, M. Point-of-Care Testing for Infectious Diseases: Diversity, Complexity, and Barriers in Low- And Middle-Income Countries. *PLoS Med.* **2012**, *9*, e1001306. [CrossRef]
20. Kondaveeti, H.K.; Kumaravelu, N.K.; Vanambathina, S.D.; Mathe, S.E.; Vappangi, S. A Systematic Literature Review on Prototyping with Arduino: Applications, Challenges, Advantages, and Limitations. *Comput. Sci. Rev.* **2021**, *40*, 100364. [CrossRef]
21. Gajera, H.; Guha, D.; Kumar, C. New Technique of Dielectric Perturbation in Dielectric Resonator Antenna to Control the Higher Mode Leading to Reduced Cross-Polar Radiations. *IEEE Antennas Wirel. Propag. Lett.* **2017**, *16*, 445–448. [CrossRef]
22. Galindo-Romera, G.; Carnerero-Cano, J.; Martínez-Martínez, J.J.; Herraiz-Martínez, F.J. An IoT Reader for Wireless Passive Electromagnetic Sensors. *Sensors* **2017**, *17*, 693. [CrossRef]
23. Meaney, P.M.; Fox, C.J.; Geimer, S.D.; Paulsen, K.D. Electrical Characterization of Glycerin: Water Mixtures: Implications for Use as a Coupling Medium in Microwave Tomography. *IEEE Trans. Microw. Theory Tech.* **2017**, *65*, 1471–1478. [CrossRef]

24. Ellison, W.J.; Lamkaouchi, K.; Moreau, J.-M. LIQUIDS Water: A Dielectric Reference Water: A Dielectric Reference Chapter I. *J. Mol. Liq.* **1996**, *68*, 171–279. [CrossRef]
25. Sihvola, A. Mixing Rules with Complex Dielectric Coefficients. *Subsurf. Sens. Technol. Appl.* **2000**, *1*, 393–415. [CrossRef]
26. Ebrahimi, A.; Tovar-Lopez, F.J.; Scott, J.; Ghorbani, K. Differential Microwave Sensor for Characterization of Glycerol–Water Solutions. *Sens. Actuators B Chem.* **2020**, *321*, 128561. [CrossRef]
27. Li, M.; Wibowo, S.; Li, W.; Li, L.D. Quantitative Spectral Data Analysis Using Extreme Learning Machines Algorithm Incorporated with PCA. *Algorithms* **2021**, *14*, 18. [CrossRef]
28. Lever, J.; Krzywinski, M.; Altman, N. Points of Significance: Principal Component Analysis. *Nat. Methods* **2017**, *14*, 641–642. [CrossRef]
29. Bzdok, D.; Krzywinski, M.; Altman, N. Points of Significance: Machine Learning: Supervised Methods. *Nat. Methods* **2018**, *15*, 5–6. [CrossRef] [PubMed]
30. Nello, C.; John, S.-T. *An Introduction to Support Vector Machines: And Other Kernel-Based Learning Methods*; Cambridge University Press: Cambridge, UK, 2000; ISBN 9780521780193.
31. Cawley, G.C.; Talbot, N.L.C. On Over-Fitting in Model Selection and Subsequent Selection Bias in Performance Evaluation. *J. Mach. Learn. Res.* **2010**, *11*, 2079–2107.
32. Markel, V.A. Introduction to the Maxwell Garnett Approximation: Tutorial. *J. Opt. Soc. Am. A* **2016**, *33*, 1244. [CrossRef] [PubMed]

CHAPTER 5

A MACHINE LEARNING APPROACH FOR ENHANCING PERMITTIVITY MIXING RULES OF BINARY LIQUIDS WITH A GAUSSIAN MODIFICATION AND A NEW INTERACTION FACTOR ESTIMATION

Journal of Molecular Liquids 399 (2024) 124290

Contents lists available at ScienceDirect

Journal of Molecular Liquids

journal homepage: www.elsevier.com/locate/molliq

A Machine Learning approach for enhancing permittivity mixing rules of binary liquids with a Gaussian modification and a new interaction factor estimation

Miguel Monteagudo Honrubia *, Francisco Javier Herraiz-Martínez, Javier Matanza Domingo

Instituto de Investigación Tecnológica (I.I.T.), Universidad Pontificia Comillas, Calle de Santa Cruz de Marcenado, 26, Madrid, 28015, Spain

ARTICLE INFO

Keywords:
Binary mixture
Dielectric characterization
Machine Learning
Mixing rules
Permittivity

ABSTRACT

The microstructure and solvation mechanics of binary liquids are key for predicting mixture permittivity. However, since traditional mixing rules do not consider this complexity, they must be modified to address the mixture characteristics through an interaction factor (k_{int}). This paper evaluates this parameter for several mixing rules, applying Support Vector Regressor models trained with glycerin-water reflective signals acquired with a Dielectric Resonator sensor. The regression error of these models indicates both the optimal interaction factor and the mixing rule that fits the most with experimental permittivity values. Kraszewski and Hashin-Shtrikman mixing rules achieved the best performance with an RMSE of around 1. In addition, this paper suggests that the interaction factor can be estimated through the molar volume and the dielectric contrast between liquids ($k_{int} = 2.67$) without acquiring experimental data. Moreover, after analyzing the physical limitations of a linear modification formula, this paper proposes an alternative based on a Gaussian function that avoids unrealistic volume fractions. Both contributions enhance mixing rule accuracy and improve the flexibility to model mixture dielectric behavior.

1. Introduction

Any heterogeneous material is a complex physical-chemical system with inclusions of another material or different phases of the same material. The structural characteristics of these materials such as size, shape, spatial distribution, or the mutual interaction of the heterogeneities, are critical to understanding the macroscopic properties. This paper focuses on dielectric permittivity, which can reveal information about the intramolecular interaction of mixture components, helping to characterize liquid solutions as well as composite materials [1]. It also has particular relevance for designing and validating microwave sensors that measure permittivity changes as a detection method for chemical or biological samples [2].

Nevertheless, estimating the dielectric permittivity in binary mixtures is still challenging, and so far, the best alternative is performing a direct measurement of the mixture of interest. The open-ended probe is the most popular dielectric spectroscopy technique for liquid characterization. Connected to a Vector Network Analyzer (VNA), the coaxial probe is submerged in the liquid sample to measure the reflective wave's scattering parameters in a long range of frequencies [3]. However, the relationship between the scattering parameters and the medium permittivity relies on algorithms and the probe equivalent circuit. Depending on these models, the measured permittivity could present variations [4]. Moreover, the experimental setup imposes constraints in terms of probe dimensions and positioning, sample size, and frequency range, which affect the method accuracy [5]. The lack of dielectric data for many binary mixtures hinders the validation of the measurements. Therefore, a theoretical permittivity estimation would be useful to contrast any experimental results and detect possible systematic errors. In addition, this methodology requires expensive equipment, which is not always available, and developing an accurate mixing rule would be faster and cost-saving to estimate the permittivity of binary solutions.

First, Section 2 discusses the state-of-the-art of permittivity estimations with mixing rules and their limitations in modeling the dielectric behavior of binary mixtures. Therefore, this section also introduces a novel Machine Learning approach for validating and optimizing mixing rules through an interaction parameter. Section 3 details the data and

* Corresponding author.
E-mail address: mmonteagudo@comillas.edu (M. Monteagudo Honrubia).

https://doi.org/10.1016/j.molliq.2024.124290
Received 14 November 2023; Received in revised form 31 January 2024; Accepted 17 February 2024
Available online 23 February 2024

the algorithms employed and discusses two contributions to improve mixing rules: a formula to estimate the interaction factor through pure liquid properties and a new Gaussian modification formula. Finally, Section 4 shows our approach results for the glycerine-water mixture and discusses the effect of both contributions to improve permittivity estimation.

2. Theory

2.1. The search for a general solution

In an extensive review, Brosseau [6] summarized the historical approaches addressing the permittivity estimation of binary mixtures, from theoretical formulations, using Maxwell's electromagnetic (EM) theory, to relatively recent electromagnetic simulations of these materials. As a result, many formulas have been proposed to estimate the permittivity of heterostructures from the permittivity value of the pure compounds without performing experimental measurements [7]; however, none of them has been proved as a general solution. Indeed, one of the critical issues detected by Brosseau is the excessive number of formulas with uneven estimations that hinder their interpretation and validation.

In general, the formulas aim to calculate the permittivity of an effective homogeneous medium, which conceptually replaces the heterogeneous medium while keeping the same dielectric properties. It should be noted that this approximation is only valid when the incident electromagnetic (EM) waves have a wavelength significantly greater than the dimensions of the inhomogeneities. Besides, many of these formulas are constructed under the assumption of isotropy, which is rarely the case for complex materials. However, regardless of their theoretical grounding, all these formulas have limited success fitting the experimental data, thus giving poor permittivity estimations. In contrast, other formulas follow an empirical approach, and although they allow adjusting experimental data, they are limited to specific systems and cannot be generalized.

As has been observed, most theoretical formulas only work adequately for a minimal fraction of heterogeneities, while for larger volumes of inclusions, the formula's error becomes excessive [6]. It has been suggested that these formulas only consider volume fraction or molar fraction as unique parameters, without indicating the structure of the mixture or the possible interaction between components. In addition to the bibliography examined by Brosseau, later works comparing mixing rules also demonstrate these discrepancies between experimental data and permittivity estimation [7][8]. However, it should be noted that the lack of experimental data limits this mixing rule validation, and the existing data have been extracted with different methods, many of which lack an estimate of the error.

Qin et al. [9] conducted an extensive review of the calculation of the electromagnetic properties of composites based on their structural parameters at the microscopic (atoms and dipoles), mesoscopic (phases, inclusions, agglomerates), and macroscopic (sample volume) scales. Knowing the relationship between scales is essential for understanding the propagation of EM waves in these materials and, therefore, for designing tailored composites for different technological applications. The importance of the mixture structure is strongly related to the very definition of permittivity: a physical parameter that indicates the polarization capability of the material and, therefore, how easily its internal charges can be aligned to the incident electric field [10]. Permittivity depends on the density and the separation of charges; therefore, the heterogeneities in a material cause a non-uniform polarization, which depends not only on the position and distribution of the inclusions, but also on the electric interaction between them and the solvent matrix containing them [9]. In conclusion, there is an effective permittivity, but this can only be accurately calculated by knowing the microstructure of the mixture and the set of electrical interactions between the phases. However, even knowing the geometry, the permittivity calculation is a high-complexity problem and relies on EM simulation as the only feasible method.

This problem is particularly complex in the case of liquid solutions since the fluid microstructure cannot be observed as easily as a solid material. Tang et al. [11] analyze the severe difficulties in observing and determining cluster structures in aqueous solutions, even when spectral techniques or computational simulations are used. The formation of solute clusters in the primary solvent in aqueous solution defines the mesostructure and microstructure. This solvation process is determined by the network of hydrogen bonds and Coulombic forces, which largely depends on parameters such as chain length and solute concentration, but also on solution thermodynamic properties [11]. The rearrangement process can generate different geometries of clusters: spheres, cubes and chains [12]. The studies reviewed by Tang et al. indicate that conformational changes occur at critical concentrations [11]. Therefore, the microstructure changes (structural transition) should be observed through trend changes in the permittivity-volume fraction function. These insights can be extended to other polar solvents as shown by Pradhan et al. in a review of molecular interactions of non-aqueous solutions [13]. Moreover, if the solute is also a polar substance, the system will undergo a competition between solute-solute, solvent-solute, and solvent-solvent interactions. In that case, the solvation process will be too specific to extract a general rule [14].

In summary, defining the exact dielectric behavior of a solution is a high-complexity problem that has not yet been solved. For this reason, despite the drawbacks discussed in this section, mixing rules seem the only feasible method for estimating the effective permittivity of binary liquids. Therefore, new approaches are required to improve mixing rules, including other parameters to approximate molecular interaction or microstructure.

2.2. Improving mixture rules, from the thermodynamic approach to Puranik modification

The works of Reis et al. [15] and Iglesias et al. [1] propose a thermodynamic approach to define the ideal dielectric behavior of a mixture. The electric polarization results in the reorientation of the sample dipoles and is therefore equivalent to an energy change of the system, allowing the application of thermodynamic formulation. According to this approach, the ideal permittivity of the mixture is the volume-fraction weighted average of each component permittivity (1) [15], being ϕ_{A-B} and V_{A-B} the respective volume fraction and volume of each liquid.

$$\varepsilon_{Ideal} = \varepsilon_A \phi_A + \varepsilon_A \phi_A$$
$$\phi_A = \frac{V_A}{V_B + V_A} = 1 - \phi_B \tag{1}$$

The ideal value assumes a linear, isotropic, and homogeneous medium between the parallel plates of a capacitor [16]. The excess between the ideal and the measured permittivity is strongly related to the deviation from the ideal thermodynamic behavior. Peon Iglesias [1] proposed a method to estimate this excess and concluded that it is mainly attributable to the dielectric contrast ($\varepsilon_A/\varepsilon_B$) and the effect of the molecular interaction through electrostatic bonds and induced dipoles, which none of the traditional formulas consider. The excess due to variations in the void volume of the mixture is apparently less significant. Every binary mixture is indeed the mixture of each substance and the free space between them. This volume can vary due to the rearrangement of the molecules and interactions upon mixing. If the void volume increases, the dipole density is sparser; if it decreases, the dipoles condense. These findings support the idea of modifying the mixing formulas to model somehow the excess. For example, Puranik et al. [17] proposed a modification formula (2) to replace the solvent volume fraction (ϕ_A) by an effective volume fraction ($\phi_{A_{eff}}$) through an interaction parameter (k_{int}).

$$\phi_{A_eff} = [k_{int} * (1 - \phi_A) + \phi_A] * \phi_A$$
$$\phi_{B_eff} = 1 - \phi_{A_eff} \quad (2)$$

The interaction parameter k_{int} aims to synthesize how the intramolecular interactions rearrange the molecules in the mixture structure, changing the volume fraction. Moreover, this effect should be practically null in non-polar liquids, giving a k_{int} value close to 1 [17]. This is consistent with the insights from the bibliography introduced so far, which question the suitability of the volume fraction as a parameter to estimate the mixture permittivity beyond isotropic, ideal, or homogeneous liquids [15]. The modification formula was tested to fit the predictions of Bruggeman's formula to the permittivity measurements of water-alcohol mixtures. Unfortunately, the authors did not provide a deeper theoretical justification for this modification. However, it has been tested by Amooey et al. [7] and Sarami et al. [8] applying the modification to compare an extensive list of mixing rules, with positive results: all the formulas fit their experimental data better. Nevertheless, this methodology has two drawbacks. Firstly, the parameter k_{int} is calculated with an optimization algorithm in order to reduce the error between the experimental and mixing rules values. Therefore, the reliability of this estimation depends on the quality of the data and the number of data points measured for each concentration. If data are scarce, there is a risk of overfitting, and if the data contain systematic errors, the adjustment will also be wrong. Secondly, each mixture has a unique k_{int} value, and consequently, the modification formula has no predictive value for new mixtures; therefore, it serves only to validate known permittivity mixtures.

The first objective of this paper is to present a methodology based on Machine Learning models to calculate the k_{int} value and the effective volume fraction without the risk of overfitting. The second objective is to propose a formula to estimate k_{int} requiring only pure liquid properties to fulfill the need for a general predictive formula of binary mixtures.

2.3. The Machine Learning approach

The starting point for this paper is our previous research [2], in which a Dielectric Resonator (DR) sensor was used to classify glycerine solutions. While techniques such as the open-ended coaxial probe acquire a direct permittivity measure, DR sensors detect substances measuring variations in its resonance frequency, which is closely related to medium permittivity around the sensor. When a liquid sample is dropped in a small cavity on top of the sensor, there is a change of permittivity resulting in a resonance frequency shift that can be detected. Therefore, the signal acquired is an indirect measure of the liquid permittivity within the narrow frequency range of the sensor resonant behavior. This change in technology simplifies the measuring protocol, enabling a faster acquisition and reducing the liquid sample volume. In addition, the DR sensor is designed to be portable, made of economical ceramic materials, and used alongside low-cost electronics. Although the sensor cannot directly measure the permittivity value for each concentration, the signals clearly indicate permittivity variations [2].

The initial objective was to develop a regression model that correlates the reflected DR signal to the corresponding permittivity value of the solution. However, achieving a correct regression prediction requires knowing with precision the real permittivity values as the predictive variable. Which brings back the key issue of this paper: what is the permittivity of a binary mixture? Given the lack of dielectric data for many chemical and biomedical solutions of interest, this can be a critical issue. To the authors knowledge, there is just one reference with glycerine-water permittivity measures in the frequency range of the sensor [18] (Table 1). Consequently, without other experiments to contrast these values, how far is it reasonable to trust them for a regression model? This problem demands either more experimental data, which is not always possible, or theoretical or computational models to contrast with the experimental data.

Table 1
Permittivity of glycerin-water solutions extracted from [18] and [25].

Medium	$\varepsilon_{experimental}$	Medium	$\varepsilon_{experimental}$
Air	1.00	Glycerine 40%	58.78
Glycerine 80%	17.00	Glycerine 30%	65.25
Glycerine 70%	27.45	Glycerine 20%	69.23
Glycerine 60%	39.00	Glycerine 10%	74.32
Glycerine 50%	51.55	Water	78.30

Unfortunately, as was briefly discussed in the previous section, the use of suboptimal formulas is mostly forced in the case of liquid mixtures. However, as was stated before, achieving a correct regression requires knowing the real permittivity values, which implies that the regression error will be lower when more realistic permittivity values are considered within the model. In contrast, the regression error will increase when these values deviate more from reality. Using this methodology, this paper aim to evaluate both the experimental data and the formula predictions. In addition, the optimal interaction factor (k_{int}) could be estimated by minimizing the regression error. Unlike the works of Amooey et al. [7] and Saramy et al. [8], optimization algorithms such as Levenburg-Marquarts cannot be employed since the DR sensor signals do not directly give the mixture permittivity. Thus, the k_{int} cannot be fitted to match the mixing rules estimations with the DR data.

It must be noted that the success of this method depends on how this error is measured and the regression technique selected, considering that DR signals are high-dimensionality data. Linear regression is a standard method to analyze the relationship between independent variables or features and a dependent variable, such as the mixture permittivity. As a result, the regression model can predict the outcome of new input data, even interpolating unseen data points [19]. Nevertheless, linear regression is not able to fit non-linear relationships between the dependent and independent variables and requires more advanced methods such as LASSO or Ridge regression, which enable polynomial fitting of m-degree without the risk of overfitting [20]. However, the main disadvantage of traditional regression is the parametric approach: any statistical modeling formalizes the relationships between variables in the form of mathematical equations. In the case of non-linear relationships, finding a useful model could be challenging, especially when the number of features or independent variables is too large, as in any signal analysis problem.

Machine Learning (ML) is a set of computational algorithms that aim to imitate human learning by developing flexible data-driven models for identifying complex patterns, including non-linear relationships [21]. In contrast to linear regression, ML models assume a non-parametric approach where the algorithm is trained to resolve an optimization problem to fit the data with the model architecture. In a parametric model, the number of parameters is limited, and the optimization only finds the set of values that best fits the data. By contrast, in non-parametric approaches, the model complexity and internal parameters change according to the training data [22]. As a result of this flexibility, ML models are able to approach a more complex feature space without human intervention, just learning from the data structure. For this reason, we propose ML regression as the most suitable approach for permittivity regression from DR signals. Our previous work [2] tested the first concept of this approach, but without applying the volume fraction modification [17], and considering only the Maxwell–Garnett (MG) mixing rule [23] (3) to compare and validate the experimental reference with the $\varepsilon_{Maxwell-Garnett}$ estimation.

$$\varepsilon_{Maxwell-Garnett} = \varepsilon_B + 3\varepsilon_B\phi_B\frac{\varepsilon_A - \varepsilon_B}{\varepsilon_A + 2\varepsilon_B - \phi_B(\varepsilon_A - \varepsilon_B)} \quad (3)$$

We found that the permittivity value differed drastically between the MG mixing rule and the experimental reference (Table 1), and it was not possible to determine a priori if either was correct. A Support Vector

Regressor (SVR) model was trained for each permittivity set to estimate the mixture permittivity. The model performance differed, with a Root Mean Square Error (RMSE) of 1.119 for the experimental values and 2.091 for the Maxwell-Garnett estimated values, pointing to the mismatch between this formula with the experimental values. In addition, while the experimental error was uniformly distributed, the Maxwell-Garnett permittivity (3) was highly concentrated in the low glycerine concentrations. This different pattern in the error distribution indicates that SVR models can validate the fitness of a mixing rule. In this research, this methodology is extended for other mixing rules to perform a comparative analysis of mixing rules for glycerine solutions with and without the modification formula proposed by Puranik et al. [17].

3. Methods

3.1. Dataset description

The main dataset for this work was collected during our previous research [2], testing a microwave Dielectric Resonator (DR) sensor for classifying glycerine solutions. The dataset is available in a GitHub repository and includes 180 reflected signals acquired with a low-cost electronic reader based on Arduino and designed by the authors [24][dataset]. The dataset contains air and nine distinct glycerine concentrations from 0% to 80% in 10% intervals. In order to correlate the sensor response with the permittivity of these concentrations, reference values are extracted from the following studies: Meaney P. et al. [18] for glycerine solutions at 21 °C and Ellison W. et al. for pure water at 20 °C [25] (Table 1). Other data extracted from bibliographic references to validate our approach include: the interaction factors fitted by Puranik for water-alcohol mixtures [17] (Table 3); the permittivity values at several concentrations for anisole-alcohol mixtures [26], propanoic acid mixed with ethyl acetate, ethyl benzoate, and ethyl acrylate [27]; and mixtures of toluene with methanol, ethanol, and propanol [28].

3.2. Machine Learning techniques to predict the mixture permittivity

Due to the high dimensionality of the DR signals, feature reduction techniques are required to improve the training efficiency of ML models. Principal Component Analysis (PCA) is a mathematical technique that detects the directions with greater variability within the data structure and creates a new mathematical space where each signal is projected. This method preserves and condenses the information of each signal in a vector defined by the axes of the new PCA space, which are called principal components [29]. This vector will be the input feature (X) used to train the ML regression model, while the permittivity estimation will be the training target (y) (Fig. 1). For the glycerine-water mixture dataset, the number of principals was established at seven, which condense 95% of the explained variance within the dataset.

Prior screening showed that the most optimal ML model for permittivity regression was Support Vector Regressor (SVR), an extension of the Support Vector Machine (SVM) classification model. While the SVM finds the hyperplane in the feature space, which maximizes the separation between classes [30], the SVR calculates the hyperplane with a flexible error margin that defines the volume containing most of the training data. Thus, the SVR predictions will be inside this volume, which is optimized through model training to make it as narrow as possible [31]. This training is tuned by two hyperparameters: C, which defines the hyperplane exclusion margin, and γ, which regulates the influence distance of a single training point.

The SVR models were implemented with Python using the scikit-learn library [32]. The radial basis function kernel was selected to learn the non-linear relationships within the dataset. Bayesian optimization implemented with scikit-optimize library was used for the hyperparameter tuning [33]. This search algorithm found through training iterations that the hyperparameter combination with the lowest RMSE was C = 7500 and $\gamma = 0.003$. Besides dividing the dataset into train and test

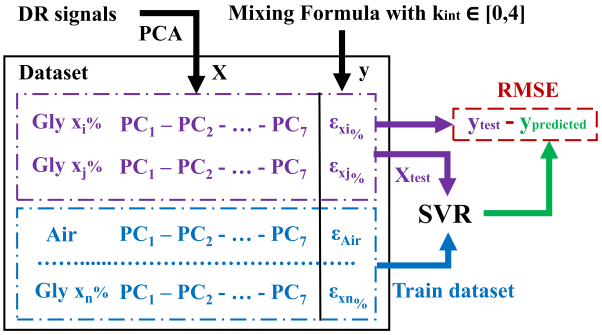

Fig. 1. Summary of the ML approach for a given mixing formula considering a k_{int} value between 0 and 4. This protocol will be repeated for each formula.

to prevent overfitting (70%-30%), the K-fold Cross-Validation method was applied during the model training with k = 5 folds [34].

A set of SVR models were trained to fit the permittivity estimations given by each mixing rule, considering an interaction factor between 0 and 4. After training, each SVR model is fed with the test dataset to generate predictions ($y_{predicted}$) (Fig. 1). The RMSE measures the model accuracy with respect to the test permittivity values (y_{test}). Therefore, this score evaluates the performance of each mixing rule for a particular k_{int} interaction value.

3.3. Mixing rule selection

As the literature indicates, finding the best mixing rule may be not possible since it could depend on the binary mixture. Thus, the aim of this work is proposing new methods to enhance any mixing rule. The mixing rule selection to show the fitting improvement is a subset from the selection made by Sarami et al. [8]. In a preliminary assessment, the whole was tested but all mixing rules show a similar trend but with displaced values, including high-order mixing rules such as Oster [35] or Onsager-Bottcher [36], therefore; for clarity, just the first-order equations were considered. Other mixing rules, such as the Bruggeman asymmetric [37] or Bottcher-Bordewijk [38], achieved a good fitting; however, they were not included to avoid an excessive overlap that made the figures unclear. The final mixing rule selection is a representative set that cover the range of values between the upper a lower bound established by the Ideal (1) and Wiener (9) mixing rules. Besides the Maxwell-Garnett (3) and Ideal (1), the following mixing rules were considered: Hashin-Strikman (4) [39], Looyenga (5) [40], Peon-Iglesias (6) [41], Lichtenecker-Rother (7) [42], Kraszewski (8) [43], Wiener (9) [44].

$$\frac{(\varepsilon_{Hashin-Strikman} - \varepsilon_A)}{(\varepsilon_{Hashin-Strikman} + 2\varepsilon_B)} = \frac{\phi_A(\varepsilon_A - \varepsilon_B)}{3\varepsilon_A} \tag{4}$$

$$\varepsilon_{Looyenga} = [\varepsilon_A^{1/3} + \phi_B(\varepsilon_B^{1/3} - \varepsilon_A^{1/3})]^3 \tag{5}$$

$$\varepsilon_{Peon-Iglesias} = \varepsilon_{Ideal} * [1 - \frac{2}{3}\ln\frac{1 + \phi_A((\frac{\varepsilon_A}{\varepsilon_B}) - 1)}{(\frac{\varepsilon_A}{\varepsilon_B})^{\phi_A}}] \tag{6}$$

$$\varepsilon_{Lichtenecker-Rochter} = \varepsilon_A^{\phi_A} * \varepsilon_B^{\phi_B} \tag{7}$$

$$\sqrt{(\varepsilon_{Kraszewski})} = \phi_A * \sqrt{(\varepsilon_A)} + \phi_B * \sqrt{(\varepsilon_B)} \tag{8}$$

$$\frac{1}{\varepsilon_{Wiener}} = \frac{\phi_A}{\varepsilon_A} + \frac{\phi_B}{\varepsilon_B} \tag{9}$$

3.4. The Gaussian modification and a novel formula to estimate the interaction factor

However, the proposed methodology still demands a significative amount of data acquisition to train the ML models and find the optimal interaction factor. Therefore, to avoid the need for experimental data,

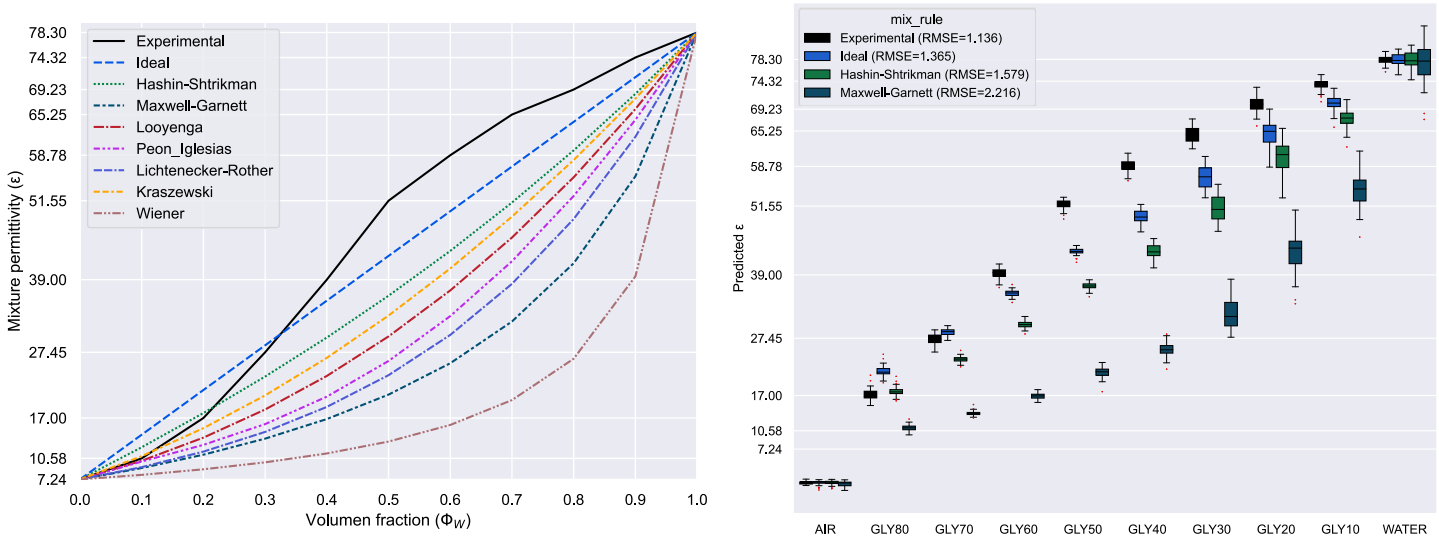

Fig. 2. (a) Comparison of the mixing rules permittivity estimations with the experimental values. (b) Boxplot distribution of permittivity predictions from SVR models trained with different mixing rules.

k_{int} should ideally be estimated with a formula requiring only pure liquid properties, enabling a priori prediction of the mixture permittivity. According to Puranik et al. [17] the change in the effective volume fraction is due to the rearrangement of the molecules within the mixture. This paper proposes that this rearrangement depends on the dielectric strength but also the size of the molecules involved, and therefore k_{int} could be estimated as a function of the dielectric contrast and molar volume relation between both liquids (10). Consequently, this estimation formula considers that the interaction factor is not a constant since the permittivity depends on the frequency of the incident wave. In addition, it also depends on thermodynamic conditions since the molar volume is proportional to the liquid density, which depends on variables such as temperature or pressure.

$$k_{int} = \frac{\varepsilon_A * Vm_A}{\varepsilon_B * Vm_B} \tag{10}$$

To prove this hypothesis, the k_{int} estimated for glycerin-water mixture is compared with the k_{int} optimal values obtained with the SVR models for each formula, but also with the interaction factor calculated by Puranik [17] for several polar binary liquids. Moreover, in order to test the whole methodology, additional measurements with DR sensor were taken for water-PEG_{400} and water-acetone mixtures. Afterwards, the best SVR models trained with the glycerin-water dielectric data and the best mixing rule using our k_{int} estimation (10) will predict the permittivity of these unseen samples. Finally, the model predictions will be contrasted with the values given by the mixing rule itself. On the other hand, as Puranik et al. state in their article, the volume fraction modification proposed (2) is not based on any theoretical justification [17]. This is a critical issue since all the methods rely on the soundness of the formula. Therefore, the mathematical domain and the fitness with the physical conditions of the problem will be analyzed. After studying its limitations, a new Gaussian modification formula is proposed.

4. Results and discussion

4.1. Mixing rules comparison

Fig. 2a shows the estimated permittivity of the chosen mixing rules for the glycerin-water mixture. None of them fit either the extracted experimental values from [18], or the curve shape. The Ideal mixing rule (1) has the best approximation, despite being a simple line crossing the curve of the experimental values. From the Hashin-Strikman (4) to the Wiener (9) mixing rules, the estimated values distance progressively from the experimental values. The Wiener mixing rule not only differs the most from the experimental curve, showing an unrealistic inverted shape, but also, it achieved the worst ML performance, and it was excluded from the discussion for clarity.

Table 2
Comparative performance between standard and modified formulas.

Mixing Rule	Initial RMSE	k_{opt}	$RMSE_{min}$ $RMSE_{min+5\%}$	$[k_{opt-range}]$
Ideal (1)	1.365	2.29	0.877 0.921	1.93-2.66
Looyenga (5)	1.820	2.17	1.182 1.241	1.91-2.49
Peon-Iglesias (6)	1.978	2.21	1.304 1.369	1.87-2.45
Lichtenecker-Rother (7)	2.102	1.99	1.461 1.534	1.81-2.37
Kraszewski (8)	1.696	2.23	1.080 1.134	1.93-2.54
Hashin-Shtrikman (4)	1.579	2.23	1.016 1.067	1.93-2.52
Maxwell-Garnett (3)	2.216	1.88	1.69 1.77	1.63-2.12

The divergences from the experimental curve are correlated with the performance of the trained SVR models (Table 2). The lowest RMSE is reached for the model trained with the experimental values, followed by the Ideal formula (1). As the mixing rule estimation differs from the experimental values in Fig. 2a, the RMSE increases. The Maxwell-Garnett mixing rule (3) used previously in [2] has the second highest RMSE. These results are represented in the boxplot of the predicted permittivity for each concentration (Fig. 2b). As is clearly depicted, lower RMSE implies narrower boxes and a lower standard deviation.

4.2. Interaction factor evaluation

Fig. 3 shows the RMSE as a function of the interaction parameter k_{int}. The experimental set represents a threshold value since it is not modified. All the mixing rules present a similar trend, reaching a minimum RMSE in an optimal region of similar k_{int} values (Table 2). This insight indicates that the interaction factor is a mixture property with a similar impact on each mixing rule. The mixing rules keep the same performance order described in the previous section. The Ideal formula (1) achieves the lowest RMSE, even surpassing the performance of the experimental value set. The Hashin-Shtrikman (4) and Krazsweki (8)

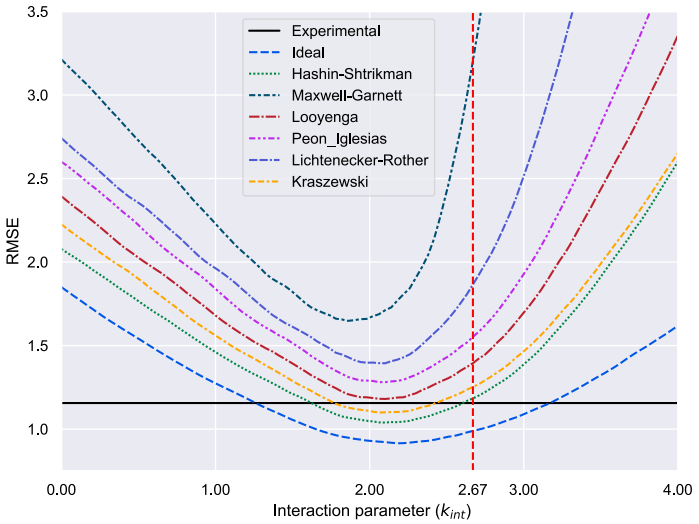

Fig. 3. RMSE variation of SVR models trained with different k_{int} values for each mixing rule. The vertical red line corresponds to the k_{int} estimated with equation (10).

mixing rules also achieved a lower RMSE error. This overperformance may indicate that the considered experimental values to train the SVR could be affected by some measured error.

Table 2 shows that after applying the Puranik modification [17] each mixing rule has a significant RMSE reduction of around 0.5-0.6. However, even with this volume fraction modification, the Maxwell-Garnett mixing rule (3) is still achieving suboptimal results and therefore has been excluded from the following discussions. Considering the remaining mixing formulas, the optimal k_{int} has a mean value of 2.18. According to the parabolic relationship between RMSE and k_{int} (Fig. 3), the RMSE variation is decreasing around the minimum. Considering a 5% error increment ($RMSE_{min+5\%}$), an optimal range with a low impact on the SVR performance can be defined between the k_{int} values of 1.9-2.5.

However, considering the mean $k_{opt} = 2.18$, which is the center of the optimal range, the new values estimated by the mixing rules do not fit the experimental values set either (Fig. 4a). But in contrast to the unmodified formulas, the new curves tend to surpass the experimental curve. Although the Peon-Iglesias (6) and Lichtenecker-Rother (7) mixing rules achieved a higher RSME, they fit quite well, especially for volume fractions (ϕ_B) higher than 0.4. Unfortunately, the Ideal formula (1), which obtains the lowest RMSE, does not fit properly with the experimental values.

On the other hand, considering now a $k_{int} = 1.9$, at the lower limit of k_{int} optimal range, there is a significant improvement in the match between mixing rules estimations and experimental data (Fig. 4b). In this scenario, the Looyenga mixing rule (5) obtains the best balance of RMSE-fitting. Nevertheless, it is clear that there is not a pure correlation between the RMSE and the mixing rule fitness. The reason why could be that the regression error reduction is due to the label distribution rather than the label values. Therefore, similar curve shapes with different permittivity values will score a similar RMSE as in the case of Fig. 4a and Fig. 4b. As a consequence, depending on the k_{int} within the optimal range, this method will find the correct mixture permittivity distribution displaced in a narrow margin.

Following the insights, the boxplot in Fig. 5 compares values 1, 1.9, and 2.18 of k_{int} for the Ideal formula (1), showing slight differences in standard deviation for each concentration. In contrast, Fig. 6 shows the fitness of the formulas with a similar RMSE to the experimental set. In this case, especially for low glycerine concentrations, the predicted permittivity from SVR models is quite similar, with no significant standard deviation differences by mixing rule. In any case, since the whole analysis is biased by the reliability of the experimental values extracted

Table 3
Summary of interaction factor values for several binary liquids compared with our formula estimation.

Mixture	$V_{m_A} \mid V_{m_B}$	$\varepsilon_A \mid \varepsilon_B$	k_{int} [17]	$k_{int} \mid k_{int^{-1}}$ (10)
Methanol (A)	40.65	32.1	1.66	0.90
Water (B)	18.02	80.1		1.11
Ethanol (A)	59.53	24.5	1.53	0.99
Water (B)	18.02	80.1		1.01
Propanol (A)	74-79	17.9	1.33	0.93
Water (B)	18.02	80.1		1.08
Formamide (A)	33.79	111	-0.10	2.597
Water (B)	18.02	80.1		0.385
DMSO (A)	71.03	46.7	2.65	2.29
Water (B)	18.02	80.1		0.437
Acetophenone (A)	116.88	17.4	2.08	1.394
Ethanol (B)	59.53	24.5		0.717

in [18], whose margin of error is unknown, the low dispersion of SVR predictions could be within this error.

4.3. A simple but an effective k_{int} estimation

Despite the considerable improvement after applying the volume fraction modification, the main drawback of this methodology is still its dependency on experimental data to calculate the interaction factor. Therefore, estimating the interaction factor a priori would be a significant advantage. Using our estimation formula (10), the interaction factor for glycerin-water mixtures is close to the optimal range of k_{int} achieved by the SVR models (11).

$$k_{int} = \frac{\varepsilon_{WAT} * Vm_{WAT}}{\varepsilon_{GLY} * Vm_{GLY}} = \frac{78.3 * 18.02}{7.23 * 73.03} = 2.67$$
$$k_{opt-SVR} = [1.9, 2.5] \tag{11}$$

In addition, the k_{int} values fitted by Puranik [17] for several binary mixtures were compared with the estimation given by the proposed formula (10). The results seem promising, with a huge level of concordance between both methods (Table 3). However, more comparisons should be made to gather more evidence that our formula could give correct estimations.

4.4. Analyzing the limitations of the volume fraction modification. A new Gaussian equation to improve permittivity estimations

The core of the previous method is the volume fraction modification proposed by Puranik et al. [17], which is not based on any theoretical justification as is stated by the authors. Therefore, its suitability depends on how well the mathematical formulation (2) is able to model the volume fraction change due to the interaction between liquids. Under the assumption of the proposed estimation formula (10), the interaction factor is the relationship between the pure liquid properties that define the molecular arrangement. Therefore, if $k_{int} = 1$, the volume fraction does not change since there is an equilibrium between the properties of both liquids. The Puranik modification satisfies this condition, and Fig. 7(a) shows how the effective volume fraction changes when the equilibrium is broken for several initial solvent volume fractions (ϕ_A). Thus, if $k_{int} < 1$, the solute liquid (B) will have more influence over the solvent liquid (A), and $\phi_{A_{eff}}$ will decrease due to the molecular packing exerted by liquid B. In contrast, if $k_{int} > 1$, liquid A will have more influence, and it will expand to compress liquid B, resulting in an increment of its effective volume fraction ($\phi_{A_{eff}}$). The Puranik modification shows that these volume fraction variations follow a linear behavior (Fig. 7(a)). Nevertheless, if $k_{int} > 2$ with this modification formula, the effective volume fraction will surpass value 1, at a speed depending on the initial volume fraction of liquid A. This behavior cannot be realistic since $\phi_A + \phi_B = 1$ implies that negative values of ϕ_B do not have

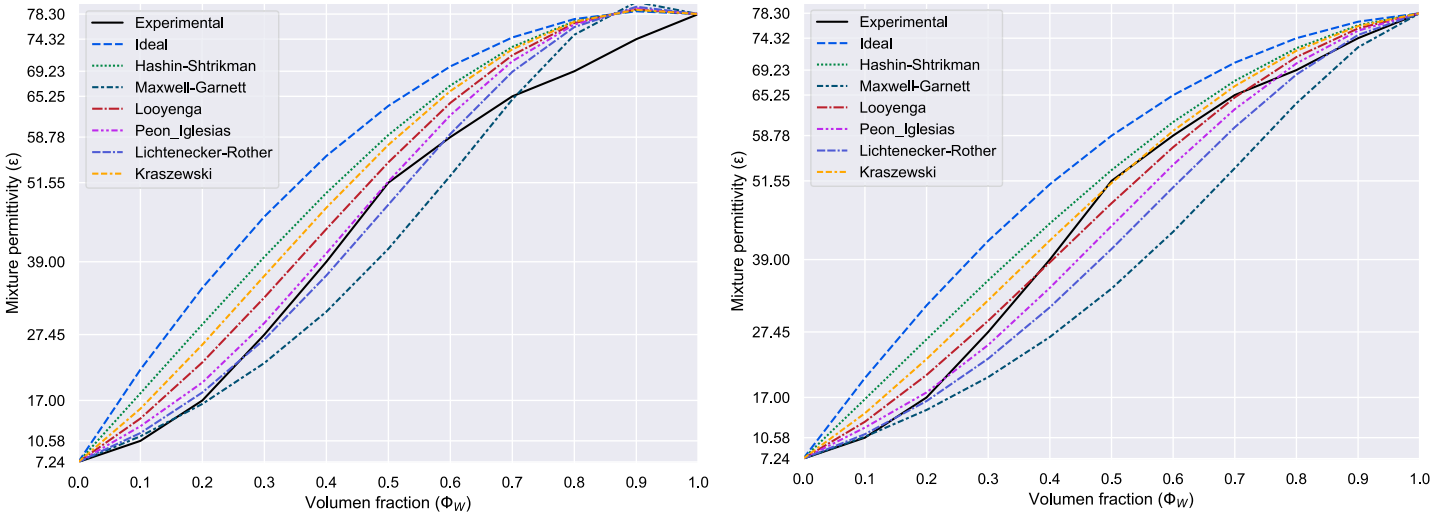

(a) k_{int}=2.18 (b) k_{int}=1.9

Fig. 4. Comparison of modified mixing rules.

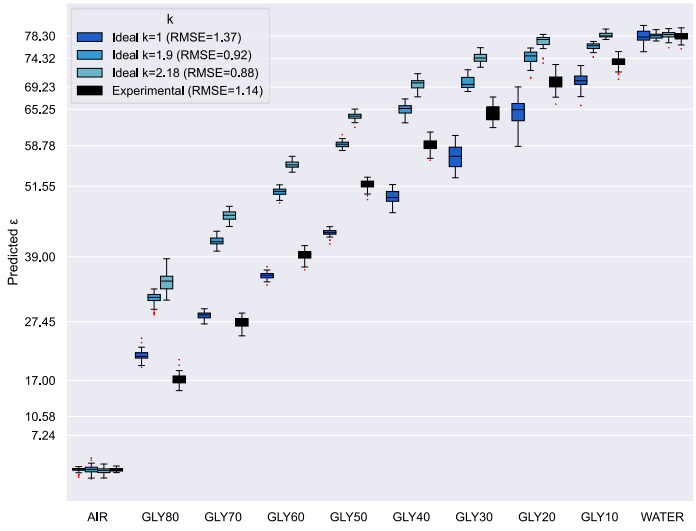

Fig. 5. Boxplot distribution of permittivity predictions of SVR models trained with different modifications of the Ideal mixing rule (1).

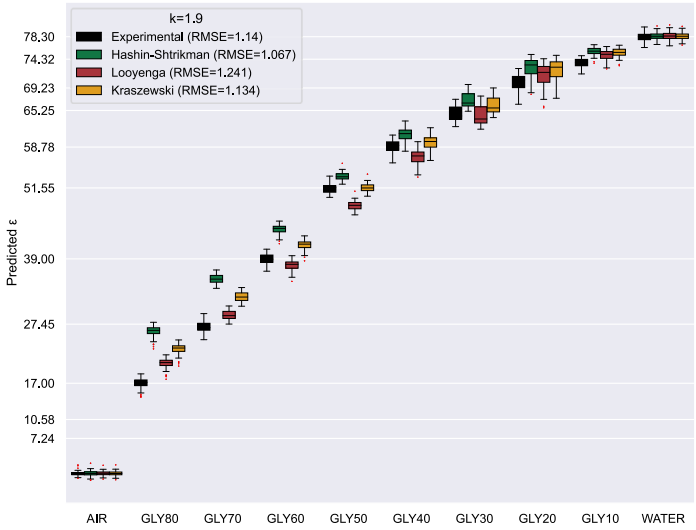

Fig. 6. Boxplot distribution of permittivity predictions of SVR models trained with different modified mixing rules with k_{int}=1.9.

a physical mean. This insight is a serious concern about applying the Puranik modification for high interaction factors and high volume fractions of solvent.

After studying these limitations, we propose a new volume fraction modification based on a Gaussian formula that satisfies the convergence to a maximum volume fraction for a high interaction factor and the equality between the effective and initial volume fraction when there is no interaction ($k_{int}=1$). The maximum expansion of ϕ_A due to molecular packing is unknown and should depend on solvent properties. Nevertheless, the value one is the physical limit, which was considered the maximum ϕ_A under the assumption that the k_{int} estimation avoids unrealistic $\phi_{A_{eff}}$ values due to the "overpacking" of liquid B.

$$\lim_{k_{int}\to 1} F(k_{int},\phi_A)=\phi_A$$
$$\lim_{k_{int}\to \infty} F(k_{int},\phi_A)=\phi_{A_{max}}=1 \tag{12}$$

However, these conditions (12) are not fulfilled by one unique function, in fact there are infinite Gaussian curves defined by the parameter μ in the exponent (13). This parameter tunes the steepness of the Gaussian curve alongside the volume fraction and interaction factor. It was determined that the optimal value for the glycerine-water mixture is $\mu=2$.

$$\phi_{A_{eff}}=1-\phi_B e^{-\phi_A^{\mu}(k_{int}-1)} \tag{13}$$

Fig. 7(b) shows that the new relationship between the interaction factor and the effective volume fraction is a smooth asymptotic curve for high-volume fractions of liquid A. In contrast, the relationship is mostly linear for lower fractions as with the Puranik modification (2) but with a lower slope. In addition, for $k_{int}<2$, both modification formulas perform in a comparable range. It must be noted that the asymptotic steepness is for $\mu=2$, but could be modified to enable a better adaptation to other liquid mixtures.

In the case of glycerine-water, applying the Gaussian modification formula with $\mu=2$ and $k_{int}=2.67$ improves the fitting for all the mixing rules (Fig. 8a). Compared to the Puranik modification (Fig. 4b), the curve shape of each mixing rule resembles more the sigmoid-like shape of experimental permittivity values. In addition, the Hashin-Shtrikman (4) and Kraszewski (8) are still the mixing rules that achieve the best fitting, as pointed out in previous insights. In summary, the combination of both proposed formulas, the Gaussian modification with the estimation of k_{int}, improves the dielectric behavior modeling.

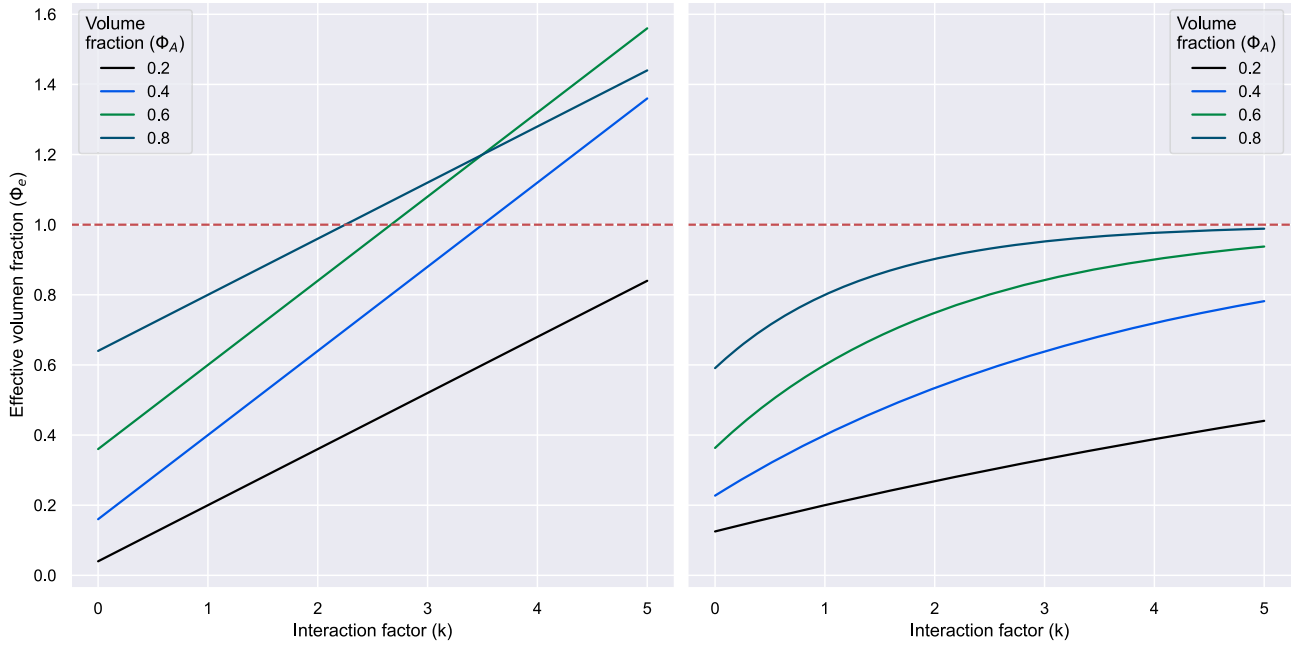

Fig. 7. Volume fraction variation as function of the interaction factor (a) Puranik et al. [17] modification (b) Gaussian modification (10).

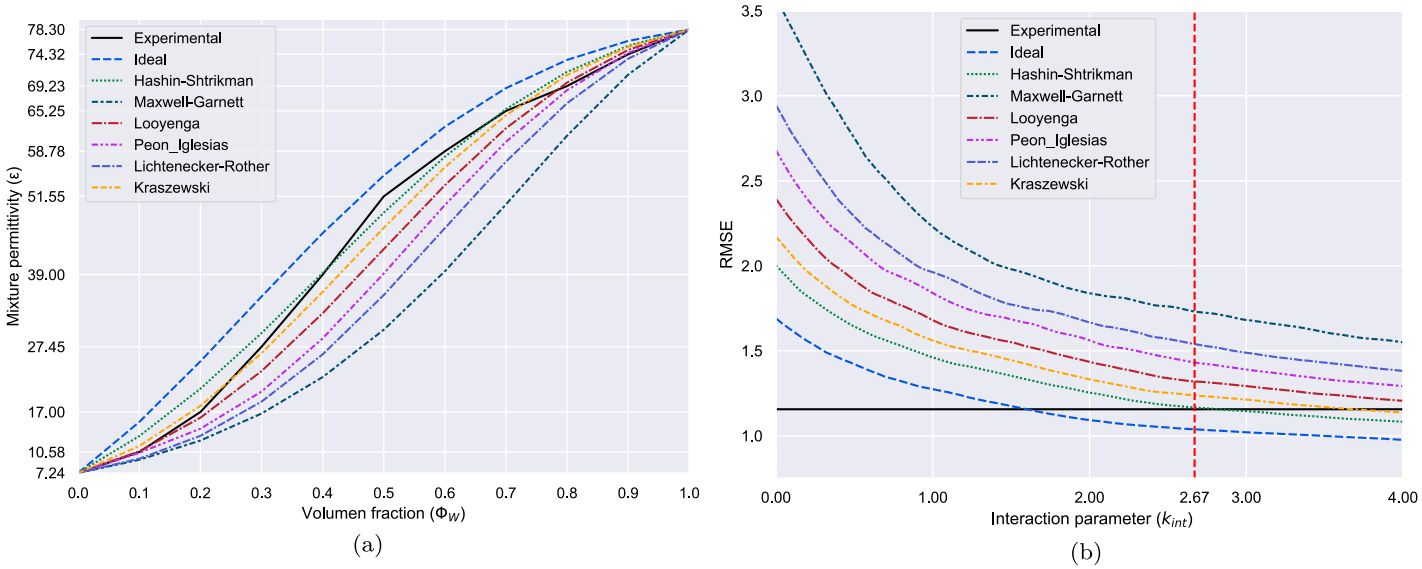

Fig. 8. (a) Comparison of modified mixing rules with $k_{int} = 2.67$ and applying the Gaussian modification. (b) Asymptotic reduction of RMSE for SVR models trained with mixing rules applying the Gaussian modification. The vertical red line is the k_{int} threshold estimated by equation (10).

On the other hand, the Gaussian modification also changes the sensitivity of k_{int} on the regression error of SVR predictions. In contrast to the parabolic behavior from Puranik modification (Fig. 3), the RMSE is reduced asymptotically to a limit value (Fig. 8b). While the Puranik modification defines an optimal region, the Gaussian modification establishes a threshold value. Indeed, for the glycerin-water system, this threshold coincides with $k_{int} = 2.67$, estimated with the pure liquid properties (10), for the Hashin-Shtrikman (4) and Kraszewski (8) mixing rules. Below the threshold, the fitting worsens exponentially (Fig. 9a) due to the nature of the Gaussian equation. In comparison, for larger k_{int} values beyond the threshold, the fitting deviates slightly (Fig. 9b) while the RMSE tends to stabilize. Additionally, it must be noted that the mixing rules keep the same performance order as previous sections, suggesting that the mixing rule suitability could depend mostly on solvation mechanism of each liquid mixture.

4.5. Validation with other liquid mixtures through other experimental data from bibliographic references

In order to evaluate if both proposed formulas could be applied to other liquid mixtures to obtain accurate permittivity estimations, dielectric data for several solutions were extracted from the following references: [26], [27], [28]. In addition, this data was used to estimate the k_{int} for each solution (Table 4).

The results vary between mixtures of anisole with several alcohols [26]; for the anisole-methanol solution, the experimental data and the modified mixing rules estimations are drastically outfitted (Fig. 10 (a)), while the anisole-hexanol mixture achieves a perfect fitting with the Hashin-Shtrikman (4) and Kraszewski (8) mixing rules (Fig. 10 (d)). Indeed, the fitting seems to worsen as the dielectric contrast increases, as is shown between the anisole-propanol and anisole-butanol mixtures in Fig. 10 (b-c). This insight could indicate that the influence of dielec-

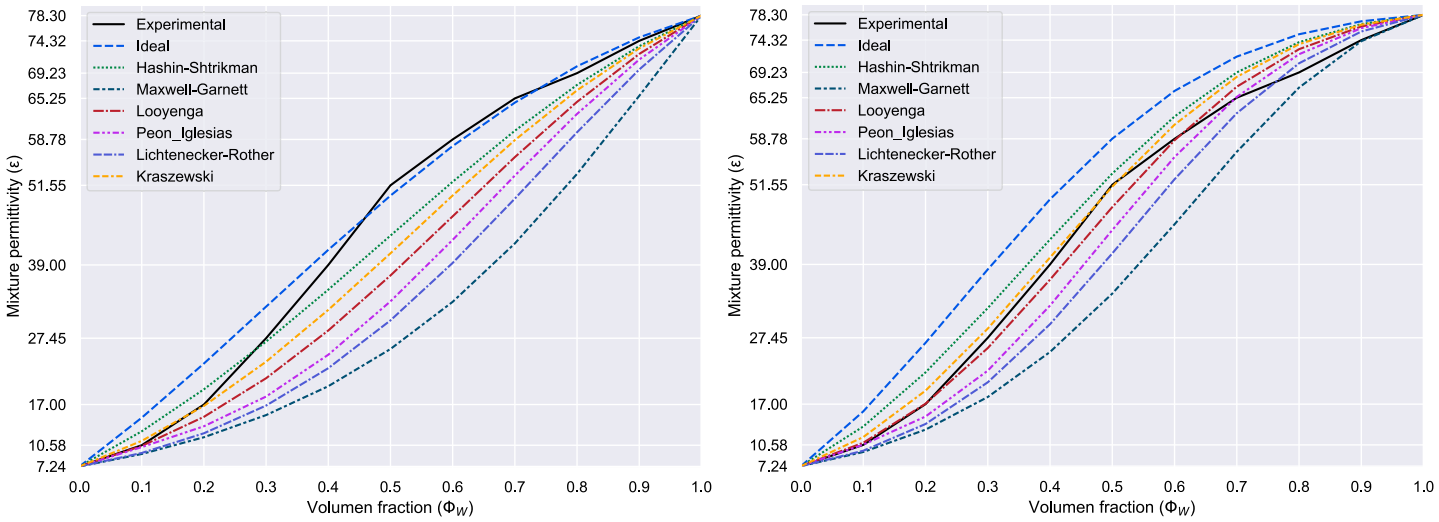

(a) $k_{int} = 1.9$ (b) $k_{int} = 3.4$

Fig. 9. Comparison of modified mixing rules after applying the Gaussian modification below (a) and above (b) the optimal threshold.

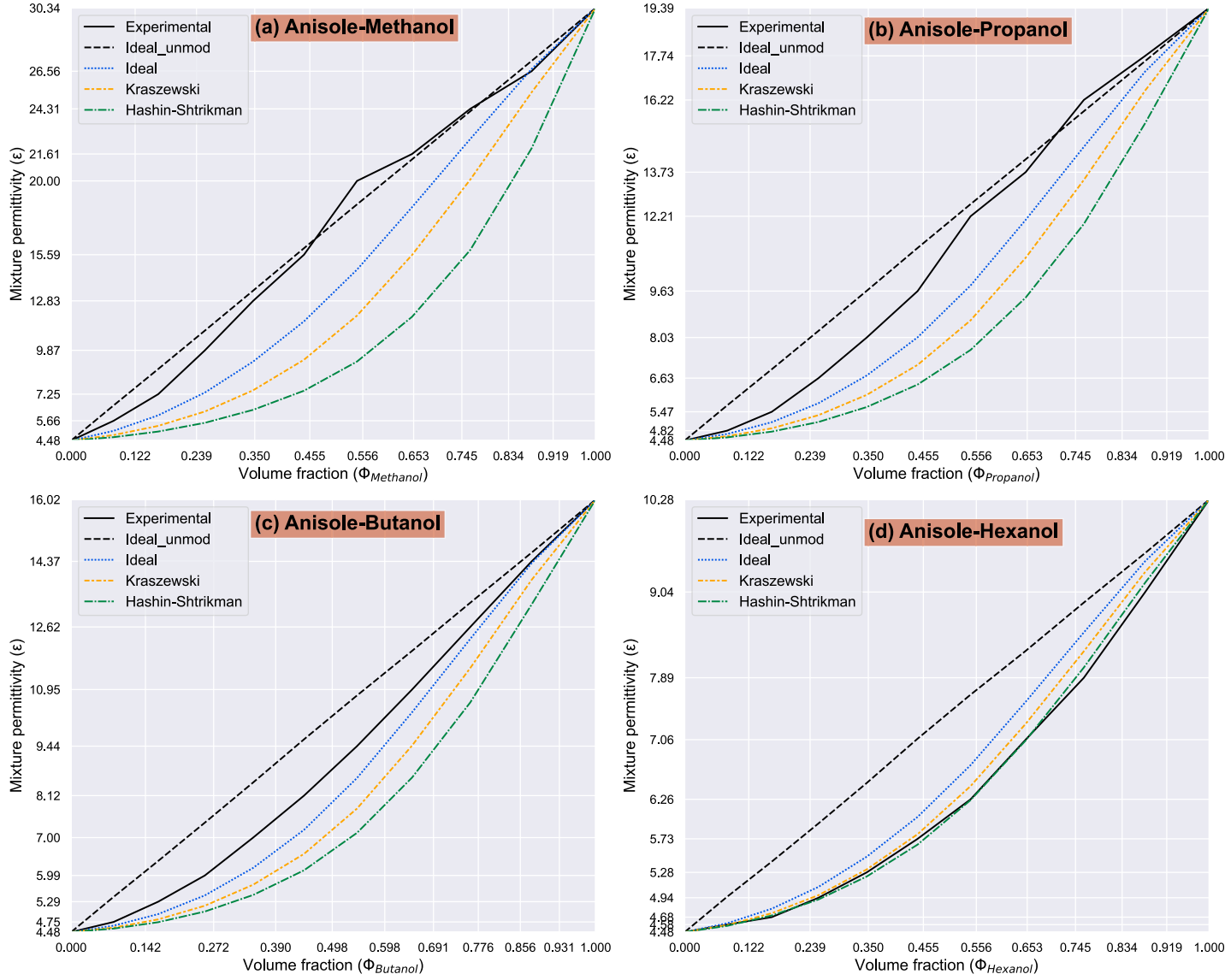

Fig. 10. Fitting of permittivity estimations for anisole mixtures after applying the Gaussian modification with $\mu = 2$ (13).

Table 4
Summary of interaction factor values for several binary liquids from the bibliography [23], [24], [25].

Mixture	$Vm_A \mid Vm_B$	$\varepsilon_A \mid \varepsilon_B$	k_{EST}	Mixture	$Vm_A \mid Vm_B$	$\varepsilon_A \mid \varepsilon_B$	k_{EST}
Methanol (A)	40.46	30.34	2.521	Propanoic acid (A)	74.98	3.36	0.296
Anisole (B)	108.68	4.48		Ethyl benzoate (B)	143.03	5.94	
Propanol (A)	74.8	19.39	2.98	Propanoic acid (A)	74.98	3.36	0.381
Anisole (B)	108.68	4.48		Ethyl acrylate (B)	106.45	6.21	
Butanol(A)	91.51	16.02	3.011	Toluene (A)	106.29	2.46	0.193
Anisole (B)	108.68	4.48		Methanol (B)	40.46	33.19	
Hexanol (A)	124.61	10.28	2.63	Toluene (A)	106.29	2.46	0.181
Anisole (B)	108.68	4.48		Ethanol (B)	59.53	24.26	
Propanoic acid (A)	74.98	3.36	0.428	Toluene (A)	106.29	2.46	0.175
Ethyl acetate (B)	97.68	6.01		Propanol (B)	74.793	19.96	

tric contrast should be adjusted to estimate k_{int}. However, the dielectric contrast between glycerine-water is greater than anisole-methanol, yet the adjustment worked perfectly. Likewise, the interaction factor could also depend on the solvation mechanisms and therefore, a formula to estimate k_{int} should be designed to address how different types of compounds interact. Although our proposed formula (11) estimates k_{int} correctly for the glycerine-water mixture, improving the formula to include other parameters could lead to better results for other liquids.

Similar discrepancies can be found in the rest of the liquid mixtures analyzed. While the fitting for propanoic acid with ethyl acetate, ethyl benzoate, and ethyl acrylate [27] was promising, the mismatch for the mixtures of toluene with methanol, ethanol, and propanol [28] was very significant. However, changing the exponent in the Gaussian modification formula can improve the fitting of the mixing rules to the experimental data. For example, after applying the equation with $\mu = 3$ (14), the anisole-propanol and anisole-butanol estimations using the Ideal mixing rule (1) lead to a better fitting (Fig. 11 (b-c)). In contrast, this exponent change hinders the fitting of the anisole-hexanol mixture (Fig. 11 (d)). In fact, the increment of μ moves the curve, approaching the unmodified ideal mixing rule. On the other hand, the estimations for the anisole-methanol mixture are slightly improved for high volume fractions, especially for the Ideal mixing rule (1), but it is still a bad fitting (Fig. 11 (a)).

$$\phi_{A_{eff}} = 1 - \phi_B e^{-\phi_A^3 (k_{int}-1)} \tag{14}$$

$$\phi_{A_{eff}} = 1 - \phi_B e^{-\phi_A^{1.5} (k_{int}-1)} \tag{15}$$

In the same way, the mixtures of propanoic acid with ethyl acetate, ethyl benzoate, and ethyl acrylate slightly improve their fitting with the Gaussian modifications with $\mu = 1.5$ (15) (Fig. 12 (a-c)). In addition, for the mixtures of toluene-ethanol and toluene-methanol, the Gaussian modifications with $\mu = 3$ (14) achieve a reasonable fitting with Looyenga's mixing rule (5) (Fig. 12 (d-f)).

These results reinforce the idea that the asymptotic steepness from the Gaussian modification could depend on the mixing behavior. As the literature indicates, the main drawback to achieving a general mixing rule is probably the different solvation processes, which are the key to defining the mixture microstructure and, therefore, the volume fraction and relative permittivity. Probably, the interaction factor cannot explain by itself the complexity of the mixture permittivity. Therefore, a multiparametric approach could be the best option to enhance mixing rules. Additional parameters, such as the factor μ, must be considered to correlate the mixture permittivity with the solvation mechanics and liquid properties. This approach could be applied to other mathematical expressions beyond the Gaussian formulation. For example, another parameter could be included in the linear formulation proposed by Puranik et al. [17].

4.6. Validation with other liquid mixtures through DR measures and SVR predictions

Most articles report dielectric measurements in static and near optic frequencies, to address minimum and maximum relaxation, respectively. As a result, finding dielectric data at specific frequency ranges for many liquid mixtures is not always possible. Thus, the DR sensor, in combination with the Machine Learning approach, can be a low-cost method to validate mixing rules estimations and/or the modification formulas proposed in this article. To prove this concept, new measurements were performed with our DR sensor for PEG_{400} and acetone in water at two concentrations: 30% and 60%. The estimated interaction factor for the PEG_{400}-water mixture (16) differs from the glycerine-water mixture (11); although the PEG_{400} has a lower permittivity at 2.45 GHz [45] than glycerol, the molecular volume is significantly larger, resulting in a $k_{int} < 1$. On the other hand, the permittivity of acetone at 2.45 GHz [46] is four times lower than water, while the molecular volume ratio is just the inverse of the dielectric contrast. Thus, the interaction factor for the acetone-water mixture is close to $k_{int} = 1$ (17), indicating that the volume fraction does not change upon mixing.

$$k_{int} = \frac{\varepsilon_{WAT} * Vm_{WAT}}{\varepsilon_{PEG} * Vm_{PEG}} = \frac{78.3 * 18.02}{6.7 * 354.61} = 0.594 \tag{16}$$

$$k_{int} = \frac{\varepsilon_{WAT} * Vm_{WAT}}{\varepsilon_{ACE} * Vm_{ACE}} = \frac{78.3 * 18.02}{19.4 * 74.034} = 0.982 \tag{17}$$

After applying PCA, the new mixture signals were analyzed using two SVR models trained with the glycerin-water mixture. The first was trained with the permittivity values from the experimental reference [18]. The second was trained with the estimations from the modified Hashin-Strihkman (4) mixing rule. This formula was selected because it achieved the best performance for the glycerine-water mixture and, therefore, has the best correlation between the sensor response and the relative permittivity of the liquid sample. The predictions of these models for both liquid mixtures were compared with the estimations from the whole set of mixing rules considered in this paper. In agreement with previous results, there are significant differences between mixing rules depending on the liquid mixture and its solvation mechanisms. In the case of the PEG_{400} solution, the Ideal formula (1) achieved the best results Fig. 13a. In contrast, for the Acetone solution, the Kraszewski mixing rule (8) obtained the best fitting (Fig. 13b), with a trend quite similar to the results. Both SVR models considered for each binary mixture gave similar predictions; once again showing how well the modified Hashin–Shtrikman mixing rule (4) models glycerine-water permittivity.

Finally, it must be noted that these new measurements for acetone and PEG_{400} were taken a year after the glycerine-water dataset, which was used to train the SVR models. However, since the DR sensor was used for other projects during this period, the air reference signal without a sample has been displaced. This sensor drift was detected after

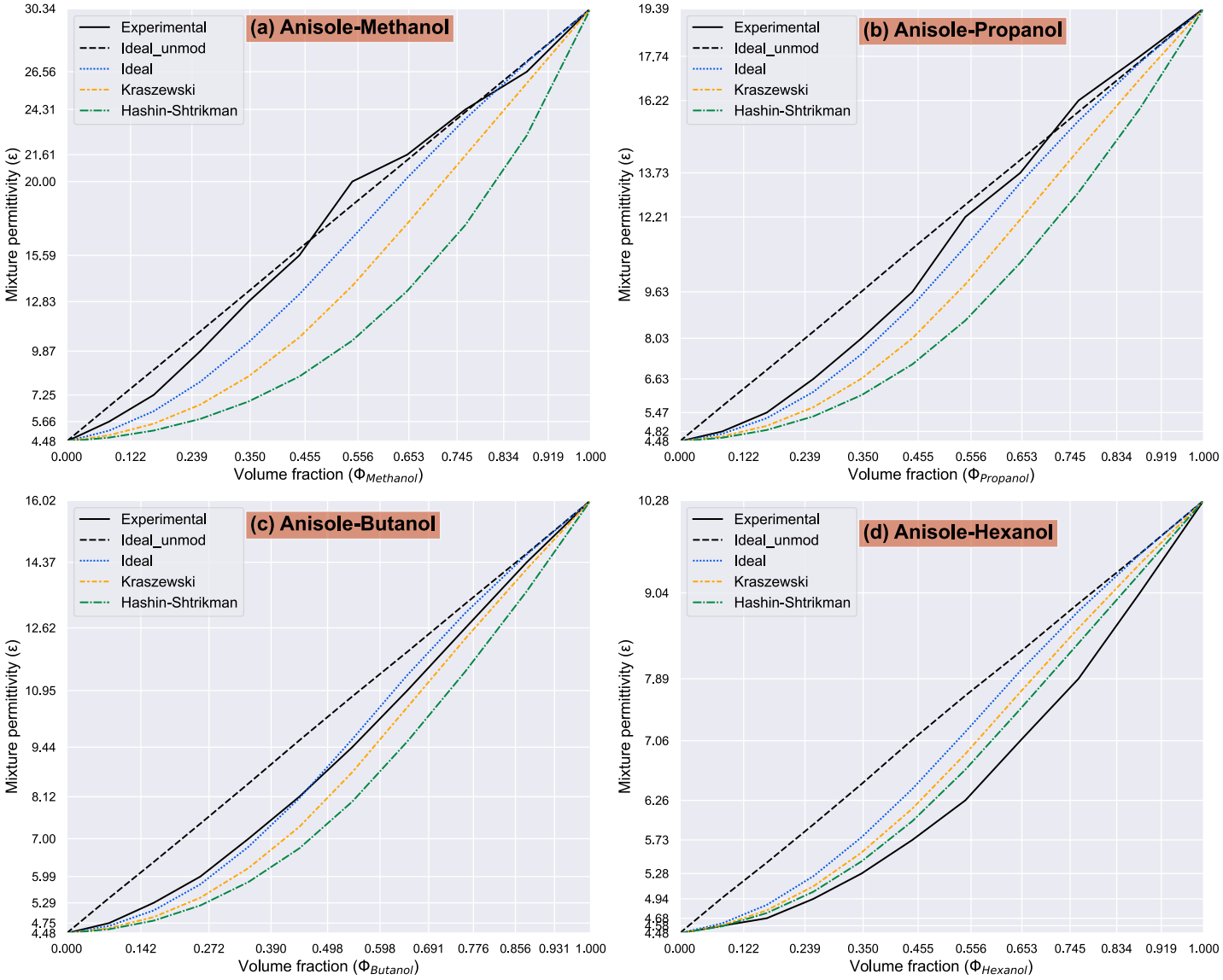

Fig. 11. New fitting of permittivity estimations for anisole mixtures after applying the Gaussian modification with $\mu = 3$ (14).

analyzing the results. Consequently, the predictions for the air reference present a small shift from the real value (Fig. 13a, Fig. 13b); this deviation must affect the rest of the measurements. Therefore, SVR predictions for water-PEG_{400} and water-acetone could be adjusted by reducing the permittivity predictions around two points, fitting the reference air prediction. This modification would slightly improve the match between the mixing rule estimated ε and the SVR predicted ε for acetone 60% and both PEG_{400} 60% and 30%, while acetone 30% deviates slightly. However, despite the sensor drift, the original results were not modified due to its qualitative information about the potential of the ML approach to validate mixing rules estimations.

5. Conclusion

Determining the dielectric behavior of a liquid solution is still an unsolved problem due to the high-complexity relationships between the liquid microstructure and the solvation mechanics. Traditional mixing rules must be modified to include this complexity in order to enhance their accuracy. The literature has proved that considering volume fraction change caused by the molecular interaction can improve the fitting of mixing rules estimations to the experimental values. This paper presents a novel approach to calculating this interaction factor (k_{int}) by applying ML regression models trained with glycerin-water reflective signals acquired with a Dielectric Resonator sensor.

Modifying the mixing rules by applying the volume fraction modification improved both the SVR performance and the fitting between estimations and experimental values. Therefore, the model RMSE can indicate both the optimal range of k_{int} and the mixing rule that obtains better estimations for the studied binary mixture. However, this methodology is limited to validation and is not suitable for a priori estimations, since it depends on acquired dielectric data. Therefore, we propose an estimation formula for k_{int}, considering only the molar volume of each liquid and their dielectric contrast ($\varepsilon_A/\varepsilon_B$), which approximately fits both the SVR results and the k_{int} estimated by Puranik et al. for water-alcohol mixtures [17].

After studying the mathematical domain of the Puranik et al. modification [17], we proposed an alternative method to calculate the effective volume fraction through a Gaussian function. This new modification formula fulfills the conditions to obtain a physically realistic volume fraction for any k_{int}. For the glycerine-water mixture, combining the formulas proposed in this article improved both the experimental fitting of the Puranik modification [17] and the match between the minimum RMSE and k_{int}. Afterward, the suitability of the Gaussian modification was tested for several binary mixtures, achieving an optimal fitting for most of them. However, the Gaussian modification

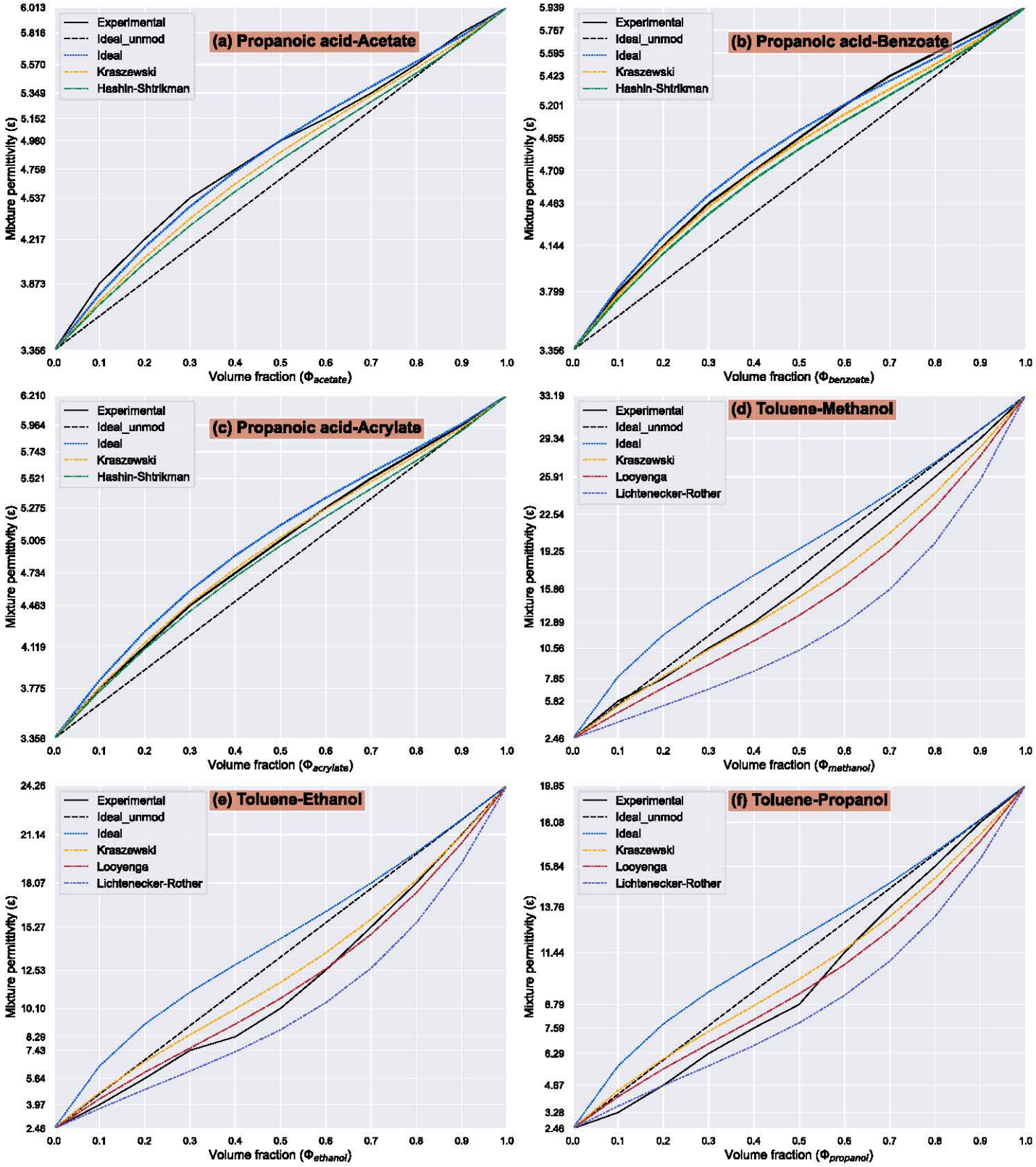

Fig. 12. Fitting of permittivity estimations for Propanoic acid mixtures (a-c) after applying the Gaussian modification with $\mu = 1.5$ (15) and Toluene mixtures (d-f) after applying $\mu = 3$ (14).

required the additional parameter μ to model the dielectric behavior. The multiparametric approach can help to improve the understanding of the mixture dielectric behavior. However, the relationship between the proposed formulas and the nature of the molecular interaction and the resulting liquid microstructure is still unknown and demands further studies.

Finally, the ML approach was also tested for acetone-water and PEG_{400}-water mixtures, proving that ML models trained with a specific mixture, such as glycerine-water, can obtain reasonable permittivity predictions to validate the mixing rules estimations for other mixtures. In conclusion, the ML approach is a promising method to validate any permittivity characterization. Using the SVR models, the interaction fac-

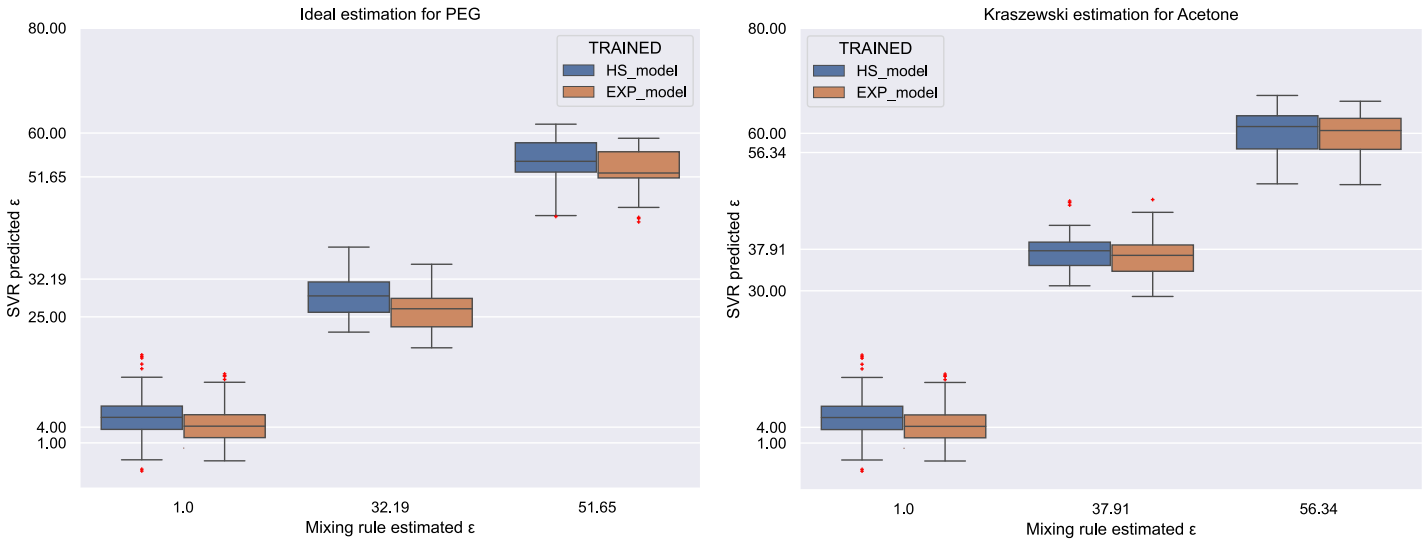

(a) $PEG_{400}30\%$ and $PEG_{400}60\%$ (b) acetone 30% and acetone 60%

Fig. 13. Distribution of SVR permittivity predictions compared to the (a) Ideal (1) and (b) Kraszewski (8) estimations.

tor can be estimated for non-direct permittivity measures from resonant techniques without the risk of overfitting. Therefore, this approach is a sound alternative to other optimization methods for enhancing mixing rules.

CRediT authorship contribution statement

Miguel Monteagudo Honrubia: Conceptualization, Formal analysis, Investigation, Software, Validation, Writing – original draft, Writing – review & editing. **Francisco Javier Herraiz-Martínez:** Project administration, Supervision, Validation, Writing – review & editing. **Javier Matanza Domingo:** Project administration, Supervision, Validation, Writing – review & editing.

Declaration of competing interest

The authors declare that they have no known competing financial interests or personal relationships that could have appeared to influence the work reported in this paper.

Data availability

The data is available in a public repository and referenced in the article.

Acknowledgement

The authors would like to express their gratitude to Christopher Michael Turner for proofreading and suggesting valuable insights about the writing.

References

[1] T.P. Iglesias, J.C.R. Reis, Separating the contributions of the volume change upon mixing, permittivity contrast and molecular interactions in the excess relative permittivity of liquid mixtures, Phys. Chem. Chem. Phys. 17 (2015) 13315–13322, https://doi.org/10.1039/c4cp05987e.

[2] M.M. Honrubia, J.M. Domingo, F.J. Herraiz-Martínez, R. Giannetti, Low-cost electronics for automatic classification and permittivity estimation of glycerin solutions using a dielectric resonator sensor and machine learning techniques, Sensors 23 (2023) 3940, https://doi.org/10.3390/s23083940, https://www.mdpi.com/1424-8220/23/8/3940.

[3] M.A. Stuchly, S.S. Stuchly, Coaxial line reflection methods for measuring dielectric properties of biological substances at radio and microwave frequencies-a review, IEEE Trans. Instrum. Meas. 29 (1980) 176–183, https://doi.org/10.1109/TIM.1980.4314902.

[4] G. Ruvio, M. Vaselli, V. Lopresto, R. Pinto, L. Farina, M. Cavagnaro, Comparison of different methods for dielectric properties measurements in liquid sample media, Int. J. RF Microw. Comput.-Aided Eng. 28 (2018) e21215, https://doi.org/10.1002/mmce.21215.

[5] M. Cavagnaro, G. Ruvio, Numerical sensitivity analysis for dielectric characterization of biological samples by open-ended probe technique, Sensors 20 (2020), https://doi.org/10.3390/s20133756.

[6] C. Brosseau, Modelling and simulation of dielectric heterostructures: a physical survey from an historical perspective, J. Phys. D, Appl. Phys. 39 (2006) 1277–1294, https://doi.org/10.1088/0022-3727/39/7/S02.

[7] A.A. Amooey, Improved mixing rules for description of the permittivity of mixtures, J. Mol. Liq. 180 (2013) 31–33, https://doi.org/10.1016/j.molliq.2013.01.003.

[8] M.A. Sarami, M. Moghadam, A.G. Gilani, Modified dielectric permittivity models for binary liquid mixture, J. Mol. Liq. 277 (2019) 546–555, https://doi.org/10.1016/j.molliq.2018.12.149.

[9] F. Qin, M. Peng, D. Estevez, C. Brosseau, Electromagnetic composites: from effective medium theories to metamaterials, J. Appl. Phys. 132 (2022), https://doi.org/10.1063/5.0099072.

[10] D.J. Griffiths, Introduction to Electrodynamics, Cambridge University Press, 2017, https://www.cambridge.org/highereducation/product/9781108333511/book.

[11] H. Tang, J. Cai, C.Y. Zhu, G.J. Chen, X.H. Wang, C.Y. Sun, Review on the clustering behavior in aqueous solutions, J. Mol. Liq. 367 (2022), https://doi.org/10.1016/j.molliq.2022.120382.

[12] R. Li, C. D'Agostino, J. McGregor, M.D. Mantle, J.A. Zeitler, L.F. Gladden, Mesoscopic structuring and dynamics of alcohol/water solutions probed by terahertz time-domain spectroscopy and pulsed field gradient nuclear magnetic resonance, J. Phys. Chem. B 118 (2014) 10156–10166, https://doi.org/10.1021/jp502799x.

[13] S. Pradhan, S. Mishra, An eye on molecular interaction studies of non-aqueous binary liquid mixtures with reference to dielectric, refractive properties and spectral characteristics, J. Mol. Liq. 279 (2019) 317–326, https://doi.org/10.1016/j.molliq.2019.01.138.

[14] M. Homocianu, A. Airinei, Intra-/inter-molecular interactions – identification and evaluation by optical spectral data in solution, J. Mol. Liq. 225 (2017) 869–876, https://doi.org/10.1016/j.molliq.2016.11.013.

[15] J.C.R. Reis, T.P. Iglesias, G. Douhéret, M.I. Davis, The permittivity of thermodynamically ideal liquid mixtures and the excess relative permittivity of binary dielectrics, Phys. Chem. Chem. Phys. 11 (2009) 3977–3986, https://doi.org/10.1039/b820613a.

[16] S.E. Wood, R. Battino, Thermodynamics of Chemical Systems, Cambridge University Press, 1990.

[17] S.M. Puranik, A.C. Kumbharkhane, S.C. Mehrotra, The static permittivity of binary mixtures using an improved Bruggeman model, J. Mol. Liq. 59 (1994) 173–177.

[18] P.M. Meaney, C.J. Fox, S.D. Geimer, K.D. Paulsen, Electrical characterization of glycerin: water mixtures: implications for use as a coupling medium in microwave tomography, IEEE Trans. Microw. Theory Tech. 65 (2017) 1471–1478, https://doi.org/10.1109/TMTT.2016.2638423.

[19] N. Altman, M. Krzywinski, Points of significance: simple linear regression, Nat. Methods 12 (2015) 999–1000, https://doi.org/10.1038/nmeth.3627.

[20] J. Friedman, T. Hastie, R. Tibshirani, Regularization paths for generalized linear models via coordinate descent, J. Stat. Softw. 33 (2010), http://www.jstatsoft.org/.

[21] A. Singh, A. Sharma, A. Ahmed, A.K. Sundramoorthy, H. Furukawa, S. Arya, A. Khosla, Recent advances in electrochemical biosensors: applications, challenges, and future scope, Biosensors 11 (2021), https://doi.org/10.3390/bios11090336.
[22] Z. Ghahramani, Probabilistic Machine Learning and Artificial Intelligence, vol. 521, Nature Publishing Group, 2015.
[23] A. Sihvola, Mixing rules with complex dielectric coefficients, vol. 1, https://doi.org/10.1023/A:1026511515005, 2000.
[24] M.M. Honrubia, Vna_er_glycerinsolutions, https://github.com/MigMH/VNA_ER_GlycerinSolutions, 2023.
[25] W.J. Ellison, K. Lamkaouchi, J.-M. Moreau, Liquids water: a dielectric reference water: a dielectric reference chapter I, J. Mol. Liq. 68 (1996) 171–279, https://doi.org/10.1016/0167-7322(96)00926-9.
[26] H.A. Chaube, V.A. Rana, D.H. Gadani, Dielectric absorption in mixtures of anisole with some primary alcohols at microwave frequency, Philos. Mag. 91 (2011) 4465–4473, https://doi.org/10.1080/14786435.2011.610374.
[27] T. Thenappan, A.P. Devaraj, Dielectric studies on binary polar mixtures of propanoic acid with esters, J. Mol. Liq. 123 (2006) 72–79, https://doi.org/10.1016/j.molliq.2005.04.010.
[28] C.V. Ramana, A.B. Kumar, A.S. Kumar, M.A. Kumar, M.K. Moodley, Dielectric and excess dielectric constants in non polar + polar binary liquid mixtures of toluene with alcohols at 303, 313 and 323 K, Thermochim. Acta 566 (2013) 130–136, https://doi.org/10.1016/j.tca.2013.05.022.
[29] J. Lever, M. Krzywinski, N. Altman, Points of significance: principal component analysis, Nat. Methods 14 (2017) 641–642, https://doi.org/10.1038/nmeth.4346.
[30] D. Bzdok, M. Krzywinski, N. Altman, Points of significance: machine learning: supervised methods, Nat. Methods 15 (2018) 5–6, https://doi.org/10.1038/nmeth.4551.
[31] F. Zhang, L.J. O'Donnell, Support Vector Regression, Elsevier, 2019.
[32] F. Pedregosa, G. Varoquaux, A. Gramfort, V. Michel, B. Thirion, O. Grisel, M. Blondel, P. Prettenhofer, R. Weiss, V. Dubourg, J. Vanderplas, A. Passos, D. Cournapeau, M. Brucher, M. Perrot, E. Duchesnay, Scikit-learn: machine learning in Python, J. Mach. Learn. Res. 12 (2011) 2825–2830.
[33] T. Head, M. Kumar, H. Nahrstaedt, G. Louppe, I. Shcherbatyi, scikit-optimize, https://doi.org/10.5281/zenodo.5565057, 2021.
[34] G.C. Cawley, N.L.C. Talbot, On over-fitting in model selection and subsequent selection bias in performance evaluation, J. Mach. Learn. Res. 11 (2010) 2079–2107.
[35] G. Oster, The dielectric properties of liquid mixtures, J. Am. Chem. Soc. 68 (1946) 2036–2041, https://doi.org/10.1021/ja01214a050.
[36] L. Onsager, Electric moments of molecules in liquids, J. Am. Chem. Soc. 58 (1936) 1486–1493.
[37] D.A.G. Bruggeman, Berechnung verschiedener physikalischer konstanten von heterogenen substanzen. i. dielektrizitätskonstanten und leitfähigkeiten der mischkörper aus isotropen substanzen, Ann. Phys. 416 (1935) 636–664, https://doi.org/10.1002/andp.19354160705.
[38] C.J.F. Böttcher, O.C. van Belle, P. Bordewijk, A. Rip, D.D. Yue, Theory of electric polarization, J. Electrochem. Soc. 121 (1974) 211Ca.
[39] Z. Hashin, S. Shtrikman, A variational approach to the theory of the effective magnetic permeability of multiphase materials, J. Appl. Phys. 33 (2004) 3125–3131, https://doi.org/10.1063/1.1728579.
[40] H. Looyenga, Dielectric constants of heterogeneous mixtures, Physica 31 (1965) 401–406, https://doi.org/10.1016/0031-8914(65)90045-5.
[41] J. Peón-Fernández, T. Iglesias, On the permittivity of mixtures: a low-fluctuation approach, J. Electrost. 32 (1994) 113–122, https://doi.org/10.1016/0304-3886(94)90002-7.
[42] K. Lichtenecker, K. Rother, Die herlritung des logarithmischen mischungsgesetzes aus allgemeinen prinzipien der stationaren stromung, Phys. Z 32 (1931) 255–260, https://cir.nii.ac.jp/crid/1572543025156436352.
[43] A. Kraszewski, Prediction of the dielectric properties of two-phase mixtures, J. Microw. Power 12 (1977) 216–222, https://doi.org/10.1080/16070658.1977.11689049.
[44] O. Wiener, Theorie des mischkorpers fur das feld der stationaren stromung, Abhandl. Sachs. Ges. Wiss. Math. Phys. K 1 (1912) 509–598, https://cir.nii.ac.jp/crid/1570854174137180800.
[45] A.V. Sarode, A.C. Kumbharkhane, Dielectric relaxation study of poly(ethylene glycols) using TDR technique, J. Mol. Liq. 164 (2011) 226–232, https://doi.org/10.1016/j.molliq.2011.09.020.
[46] A.Y. Zarubina, S.G. Kibets, A.A. Politiko, V.N. Semenenko, K.M. Baskov, V.A. Chistyaev, Complex permittivity of organic solvents at microwave frequencies, IOP Conf. Ser., Mater. Sci. Eng. 862 (2020), https://doi.org/10.1088/1757-899X/862/6/062085.

CHAPTER 6

INTO THE LATENT SPACE OF CAPACITIVE SENSORS

6.1. Introduction

Although the results obtained in Chapter 4 were promising, the ML approach for enhancing sensor performance requires extensive data acquisition to feed the model training. Indeed, collecting an experimental signal dataset could be a time-consuming and expensive task, such as in the field of human activity recognition [1]. This could be a high drawback for many sensors or analytical applications, even for the designed DR sensor, which is a portable device with a relatively simple measurement protocol for low liquid volumes. Therefore, this Chapter proposes to model the capacitive sensor behavior with a Variational Autoencoder (VAE), a Deep Learning (DL) model to generate synthetic signals to expand the dataset already collected or interpolate unseen samples, such as unmeasured glycerin concentrations.

6.2. The VAE framework

Within the context of capacitive sensors, any measured signal can be considered as a random sample (x) from the dataset distribution $p_D(x)$, which is an unknown high-dimensional probability distribution and is defined by the implicit sensor behavior. Thus, in order to generate synthetic samples, Deep Generative Models (DGMs) must find the best distribution approximation $p_\theta(x)$, parametrized by the model parameters (θ) [2]. Due to the high complexity of this task, the solution adopted by many model architectures consists in transforming the unknown data distribution into an intermediate and simpler prior distribution, commonly a Gaussian $(p_\theta(z) = N(0, I))$, that defines a lower dimension latent space [3]. Therefore, the model must also learn the joint distribution $p_\theta(x, z)$, being $p_\theta(z)$ the latent distribution that encodes the original data (6.1) [4]. This is the approach of Variational Autoencoders (VAE), which achieve the representation learning by solving a Variational Inference (VI) problem to estimate the posterior distribution $p_\theta(z|x)$ [5], [6].

$$p_\theta(x) = \frac{p_\theta(x, z)}{p_\theta(z|x)} = \frac{p_\theta(z)p_\theta(x|z)}{p_\theta(z|x)} \tag{6.1}$$

The VAE framework is based on the autoencoder (AE) architecture (Figure 6.1), which is divided into two modules: an encoder for compressing the input data in a lower-dimension encoded space, and a decoder to reconstruct the input data from the encoded representation [7]. Indeed, the result of this dimensionality reduction is analogue to a non-linear Principal Component Analysis [8]. Commonly, both modules have a symmetric design with several neural network layers, and their weights (ϕ, θ) are optimized simultaneously to reduce the reconstruction error [9]. If the reconstruction error after training is sufficiently low, the AE will generate realistic copies of the original data, fulfilling the requirements for many SDG tasks. An optimized AE could replicate signals of substances or concentrations measured by the capacitive sensor.

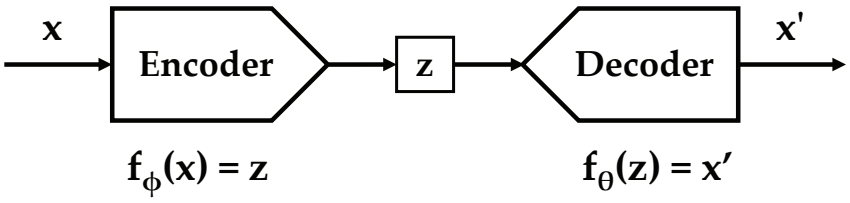

Figure 6.1: *Autoencoder structure showing the deterministic function associated with each module*

However, the basic AE is not a generative model since the learned representation barely captures any semantic relationships between latent variables. Therefore, this lack of meaningful latent variables implies a poor representation learning, leading to an unregularized latent space that avoids the generation of new data [10]. Consequently, the data classes are distributed in the latent space without any logical order, while the space between them would encode only noise. For example, the sensor signals from two very different substances, or concentrations, could be coded closely in the latent space, whereas a third substance, similar to the first, would be completely separated. This disorganization hinders the sampling of the latent space to interpolate synthetic signals corresponding to concentrations or substances unmeasured by the sensor. The VAE framework aims to overcome these drawbacks, adapting the autoencoder architecture into a probabilistic model where the encoder and decoder estimate multivariate probability distributions (Figure 6.2) [9].

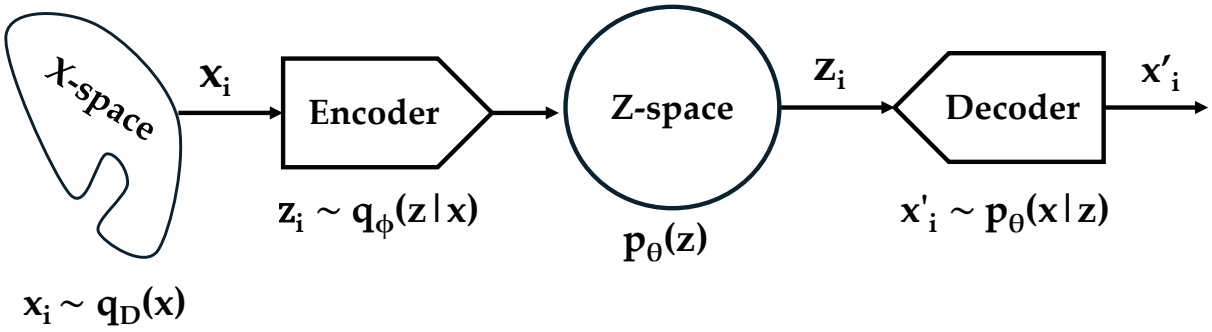

Figure 6.2: *Varitional Autoencoder structure showing the probability distribution associated with each module*

While the decoder learns the joint distribution $p_\theta(x, y)$ to sample the latent space to generate a sample from p_θ, the encoder tries to learn the true poste-

rior distribution $p(z|x)$, which models the relation between input (x) and latent (z) variables [6]. However, this distribution is also unknown and intractable; therefore, it must be approximated by solving a VI problem (Figure 6.3) [8].

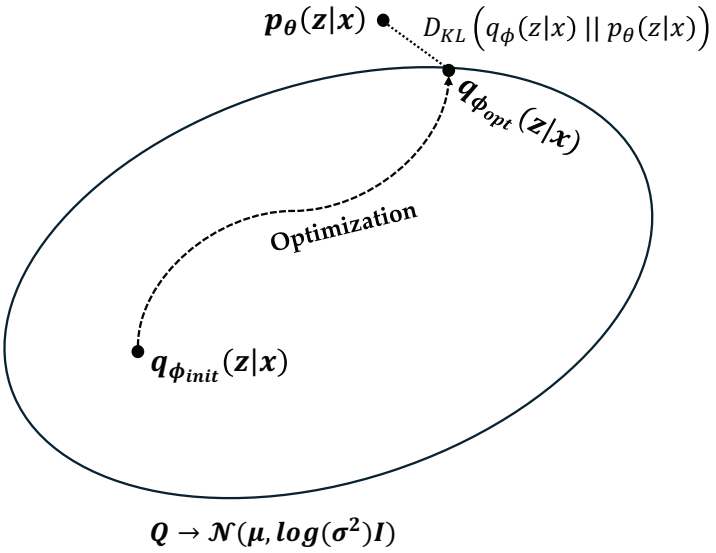

Figure 6.3: *The Variational Inference problem*

From an initial estimate $q_{\phi_{init}}(z|x)$ within a family distribution set, commonly gaussian $(q_\phi(z|x) = \mathcal{N}(\mu, log(\sigma^2)\mathcal{I})$, the true posterior can be approximated through an optimization process by varying the distribution parameters (Figure 6.3) [4]. This search can be performed by the encoder, considering its neuronal network weights (ϕ) as the variational parameters [3]. Thus, the model training through gradient backpropagation can be oriented to maximize the similarity between $p_\theta(z|x)$ and $q_\phi(z|x)$ through the Kullback-Leibler divergence (D_{KL}) (Eq. 6.2) [2].

$$D_{KL}(q_\phi(z|x)||p_\theta(z|x)) = \int q_\phi(z|x) \log\left(\frac{q_\phi(z|x)}{p_\theta(z|x)}\right) dz = \mathbb{E}_{q_\phi(z|x)}\left[\log\left(\frac{q_\phi(z|x)}{p_\theta(z|x)}\right)\right] \quad (6.2)$$

Nevertheless, since the posterior $p_\theta(z|x)$ is unknown, this (D_{KL}) expression cannot be calculated, and the VI problem therefore requires a reformulation using the Bayes rule (2) and logarithm properties (Eq. 6.3). Thus, the VAE training objective can be oriented to maximize the evidence lower bound (ELBO), which directly improves the encoder by minimizing $D_{KL}(q_\phi(z|x)||p_\theta(z|x))$ [4]. More-

over, due to the non-negativity of (D_{KL}), the ELBO (noted as $\mathcal{L}(x, \phi, \theta)$) represents the lower bound of the data log-likelihood (Eq. 6.4) [6]. Therefore, to maximizing $\mathcal{L}(x, \phi, \theta)$ is also equivalent to maximize the log-likelihood $(\log(p_\theta(x))$. In other words, finding the optimal decoder parameters (θ) improves the fitness of the estimated distribution to the original data.

$$\underbrace{\mathbb{E}_{q_\phi(z|x)}\left[\log \frac{q_\phi(z|x)}{p_\theta(z|x)}\right]}_{D_{KL}(q_\phi(z|x)||p_\theta(z|x))} = \mathbb{E}_{q_\phi(z|x)}[\log p_\theta(x)] - \underbrace{\mathbb{E}_{q_\phi(z|x)}\left[\log \frac{p_\theta(x,z)}{q_\phi(z|x)}\right]}_{\mathcal{L}(\phi,\theta;x)} \tag{6.3}$$

$$\mathcal{L}(x, \phi, \theta) = \mathbb{E}_{q_\phi(z|x)}[\log p_\theta(x)] - D_{KL}(q_\phi(z|x)||p_\theta(z|x)) \leq \log p_\theta(x) \tag{6.4}$$

Another advantage of the ELBO objective is to enable the optimization of both set of parameters at the same time through the stochastic gradient descent (SGD) technique, commonly used for training neural networks [2]. However, the random nature of latent variables (z) impedes gradient backpropagation since sampling is a non-differentiable operation. For this reason, Kingma et al. proposed externalizing the latent randomness through the "reparametrizing trick" [6]. Thus, the latent vector sampled by the encoder $(z \sim q_\phi(z|x))$ can be transformed as the combination of Gaussian noise $(\varepsilon \sim \mathcal{N}(0, \mathcal{I}))$ with the parameters of the posterior distribution (Eq 6.5).

$$z = \mu + \sigma^2 \cdot \varepsilon \tag{6.5}$$

6.3. Insights on VAE training: challenges and improvements

The ELBO objective can be rearranged to ease the computation by avoiding $p_\theta(z|x)$ (Eq. 6.6-6.7); thus, this formulation reveals additional insights about the performance of VAE training. The first term addresses the reconstruction fidelity i.e., the decoder output given a latent vector [11]. This factor is conceptually equivalent to the traditional autoencoder reconstruction objective. The (D_{KL}) term acts as a regularizer preventing the posterior distribution from di-

verging too much from the prior (Eq. 6.7). Therefore, maximizing the ELBO enforce the encoder to learn a latent space that fits a chosen prior distribution [12]. If it is a Gaussian distribution, then the training will search for latent vectors that occupy a more centralized and uniform location.

$$\underbrace{\mathbb{E}_{q_\phi(z|x)}\left[\log \frac{p_\theta(x,z)}{q_\phi(z|x)}\right]}_{\mathcal{L}(\phi,\theta;x)} = \mathbb{E}_{q_\phi(z|x)}\left[\log p_\theta(x|z) + \log p_\theta(z) - \log q_\phi(z|x)\right] \tag{6.6}$$

$$\mathcal{L}(\phi,\theta;x) = \underbrace{\mathbb{E}_{q_\phi(z|x)}[\log p_\theta(x|z)]}_{\textit{Reconstruction}} - \underbrace{D_{KL}(q_\phi(z|x)||p_\theta(z))}_{\textit{Regularization}} \leq \log p_\theta(x) \tag{6.7}$$

However, both factors can lead to poor training performance due to the contrasting effects between terms (Eq. 6.7). For example, improving the reconstruction could push the encoder to ignore the latent space shape [5]. In contrast, prioritizing the KL term could lead to overlapped latent variables that generate noisy reconstructions [13]. Therefore, the VAE training must be tuned to find a proper trade-off between both factors. The objective of this Chapter is to understand how VAEs learn the signals from capacitive sensors in order to obtain good-quality reconstruction without losing the shape of the latent space.

There are many approaches to face this challenge [8, 10, 14],but the most straightforward method is to introduce a parameter in the loss function to tune the balance between the reconstruction and the regularization term [15]. The β-VAE architecture reweights the ELBO to ensure that the posterior $q_\phi(z|x)$ match the prior $p_\theta(z)$ when $\beta > 1$ (Eq. 6.8). Whereas $\beta = 1$ is equivalent to the unmodified VAE, and $\beta < 1$ will prioritize the reconstruction over the regularization.

$$\mathcal{L}_{VAE} = \mathcal{L}_{RE} - \beta\mathcal{L}_{D_{KL}} \tag{6.8}$$

6.4. Latent space exploration to generate desired samples

Instead of decoding random vectors, how do we generate samples with desired characteristics? This is the problem of latent space exploration, which consists in understanding how the data classes and features are coded within the latent space [16]. In the case of capacitive sensors, the objective is to generate signals corresponding to specific concentrations or substances. Therefore, random sampling is clearly a suboptimal strategy to find these samples. This problem is also present in many applications, such as molecular design or drug discovery, where the randomly generated structures usually miss the desired properties [17].

Consider a well-regularized latent space where any variable z_i from the vector $z \sim p(z)$ represents a specific data feature. However, due to the lack of explainability from neural networks, finding this relationship can be challenging [18]. Therefore, exploring a high-dimensional latent space requires heuristic search algorithms to find the latent vector that generates a specific output [19]. For example, On et al. proposed an evolutionary optimization method to explore the latent space in order to find new metamaterial designs for microwave absorbers [20]. The reconstructed designs are scored according to the quality factor of the simulated spectrum; this evaluation guides the search algorithm and maps the latent space as a function of the selected score.

Other alternatives aim to incorporate structure in the latent space with conditional models [21] or using label regression to map certain subspaces through semantic keywords [22]. However, these methods limit the generation to known classes. Therefore, this work proposes to combine strategies with a Bayesian optimization search. In any case, it must be noted that the latent dimension is relevant for the search algorithms, which convergence could be hindered by too high-dimensional latent spaces. In contrast, if the dimension is too small, the VAE learning could be underfitted [3]. Consequently, the latent space size is a key hyperparameter to approach this objective.

6.5. Materials and Methods

The dataset employed in Chapter 4 is the base for this exploratory analysis of the VAE framework to generate synthetic signals of capacitive sensors. As a reminder, the dataset includes signals acquired with a VNA of air and glycerine concentrations ranging from 0% to 80%.

VAE architecture

The VAE model was implemented with Python using the Tensorflow library and Keras API. Both modules have a symmetric design made of two Neuronal Network layers with 50 neurons each and Rectified Linear Unit (ReLU) as activation function (Figure 6.4). Whereas the Linear activation is employed in the decoder output layer to reconstruct the signal, indicating that Mean Squared Error is employed to measure the Reconstruction Error. It should be changed to the sigmoid function in case of considering the Binary CrossEntropy metric instead. In addition, batch normalization is applied to ensure stable training.

On the other hand, as suggested by the Principal Component Analysis performed in Chapter 4; a latent space dimension of two is able to condense all the signal information and facilitate the interpretation of the results. In addtion, the custom Sampling Layer applies the "re-parametrization trick" to ensure the stochasticity of the latent vector.

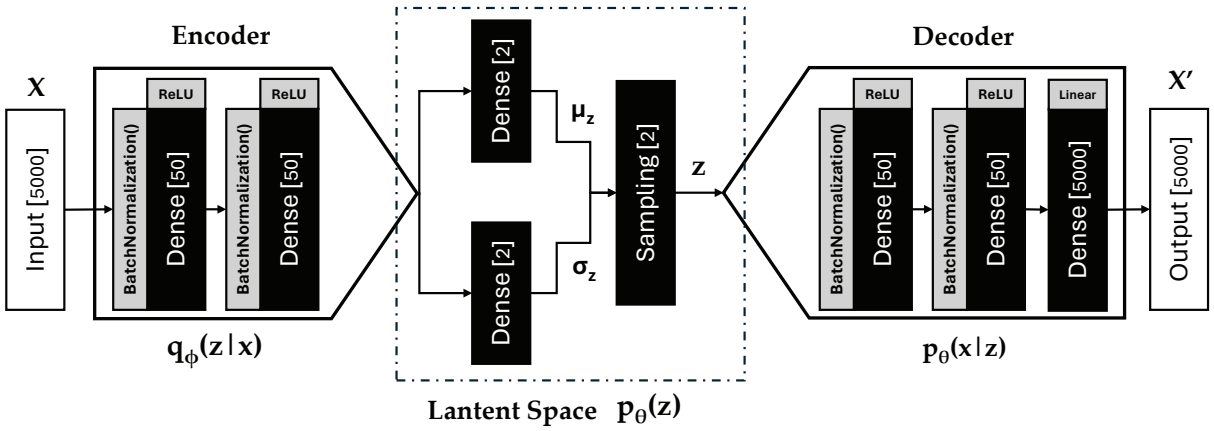

Figure 6.4: *The architecture of the VAE model implemented with Python and Tensorflow.*

Bayesian latent space search

Once the VAE model is trained, the decoder can be employed as a generator of synthetic signals. Indeed, the decoder can be fed with the latent representation of the validation dataset in order to generate similar signals. Nevertheless, as introduced before, selecting the input is not a trivial task since random vectors are not useful, and employing only the validation dataset limits our generation capacity. Consequently, this PhD thesis proposes a latent space search based on the regression error of the reconstructed signals as the score that guides the optimization search algorithm (Figure 6.5).

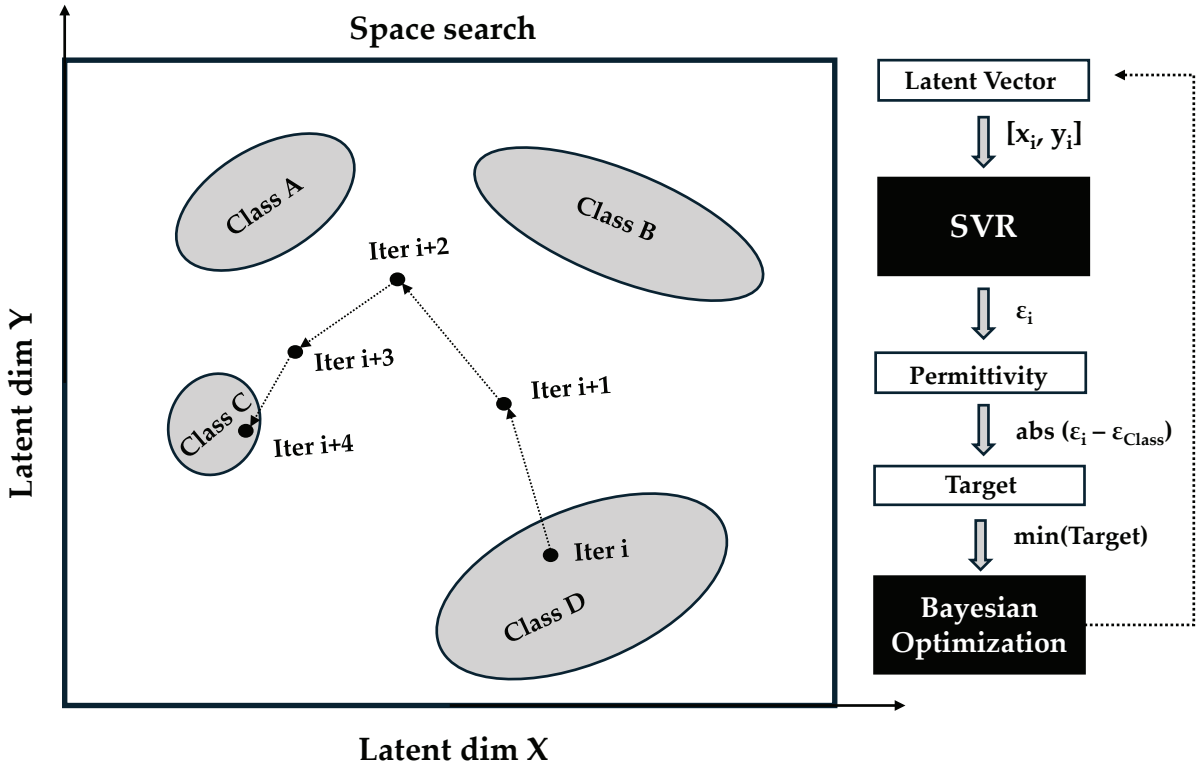

Figure 6.5: *Latent space search guided by the minimization of the regression error of latent vectors*

First, the latent representation of the whole original dataset is employed to train an ML regression model to relate the latent dimensions to the permittivity. Thus, the latent space is mapped with a parameter that is known for the desired vector. Therefore, considering a desired glycerine signal with a known permittivity $\varepsilon_{x\%}$, the proposed method searches in the latent space for the vec-

tor that minimizes the regression error (Figure 6.5). This search is performed through the Bayesian Optimization algorithm to ensure a fast convergence to the desired class, which would have a regression error close to zero. In the results section, the drawbacks and improvements of this search method are analyzed in detail.

6.6. Results an disscusion

Reconstruccion quality

In total, six VAE models were trained to evaluate the model performance for several beta values (Table 6.1). Indeed, the results for the validation dataset coincide with the insights from the literature regarding the balancing between reconstruction and D_{KL} error [5]. While the reconstruction error decreases for smaller β values, the D_{KL} error follows the opposite trend.

Beta (β)	**Reconstruction Error$_{(MSE)}$**	**D_{KL} Error**	**D_{KL} Error / β**	**Total Loss**
2.00	0.90	2.43	1.22	3.34 | 2.12
1.50	0.80	2.04	1.36	2.84 | 2.16
1.00	0.55	1.47	1.47	2.02 | 2.02
0.50	0.34	0.88	1.76	2.10 | 1.22
0.10	0.30	0.27	2.70	3.00 | 0.57
0.05	0.26	0.17	3.45	3.71 | 0.43

Table 6.1: *Reconstruction and D_{KL} Errors for different values of Beta (β).*

Figure 6.6 shows the slight improvement of reducing the balancing parameter β in the average of the reconstructed train signals for each glycerine concentration. Although the generation quality is optimal in all the cases, a small synthetic-original mismatch can be observed for $\beta = 1$. In contrast, for $\beta = 0.1$, the match between averages is almost perfect. Therefore, the proposed VAE framework can generate realistic signals of substances that belong to the original dataset and consequently enlarge the dataset by reducing the number of experiments. Nevertheless, models with values of $\beta > 1$ were discarded since they showed an unacceptable reconstruction error.

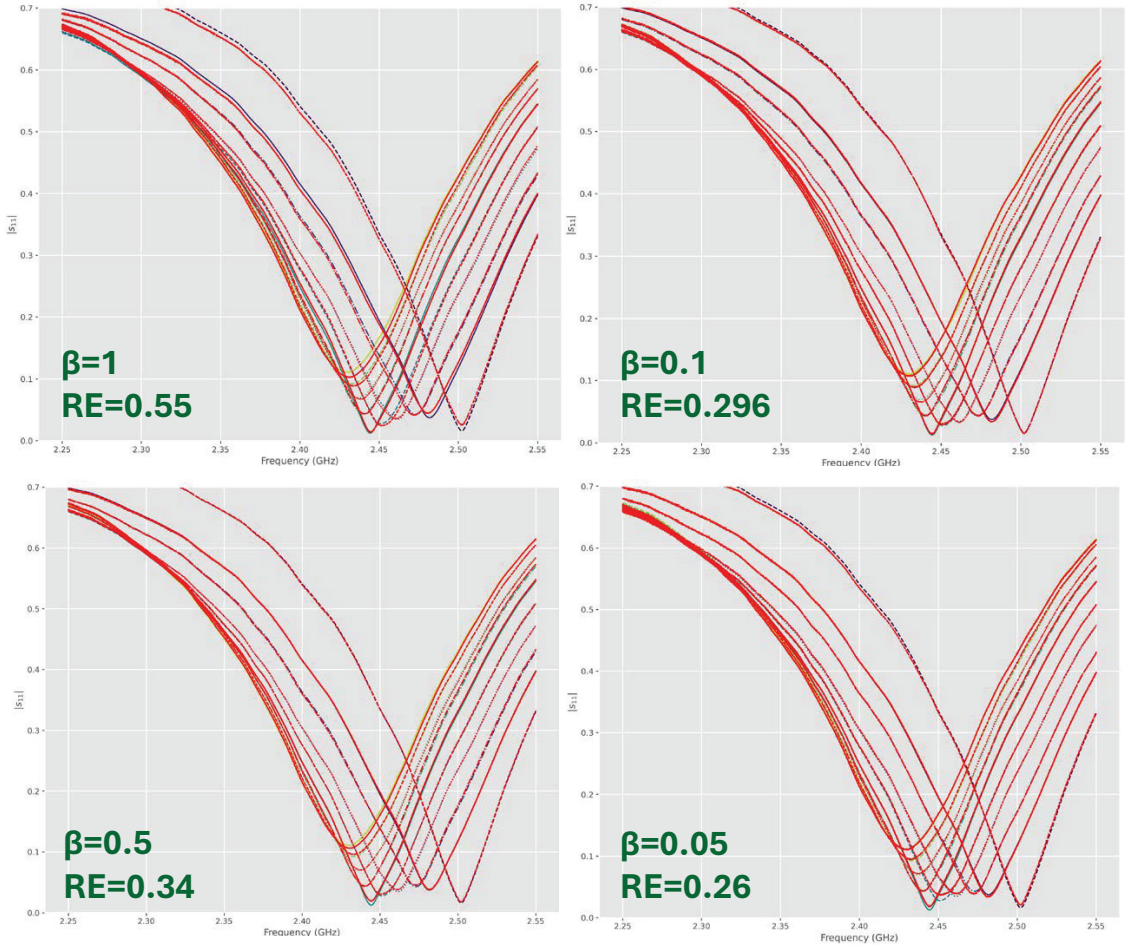

Figure 6.6: *Averages of the reconstructed signals compared to the original averages.*

While the decoded signals show slight differences, the variation of β has a more relevant impact on the latent space shape (Figure 6.7). For $\beta = 1$, the encoded signals are much more dispersed, blurring the separation between glycerin concentrations. However, when β is reduced, the latent representations for each glycerin concentration tend to concentrate in clusters, ensuring separation between classes. The latent space shape is related to the estimated distribution learned by the VAE ($p_\theta(z) = \mathcal{N}(\mu, \sigma)$). Thus, lower values of β reduce the penalty for not matching the target prior ($p_\theta(z) = \mathcal{N}(0, 1)$). The dispersion of the encoded signals is the consequence of the changes in the parameters that define the latent space distribution. Specifically, the value of σ drops from 0.11 for $\beta = 1$ to 0.01 for $\beta = 0.1$. Despite this variation, the D_{KL} error remains quite stable, probably due to the fact that the VAE manages to converge the mean distribution to $\mu = 0$ regardless of the β value.

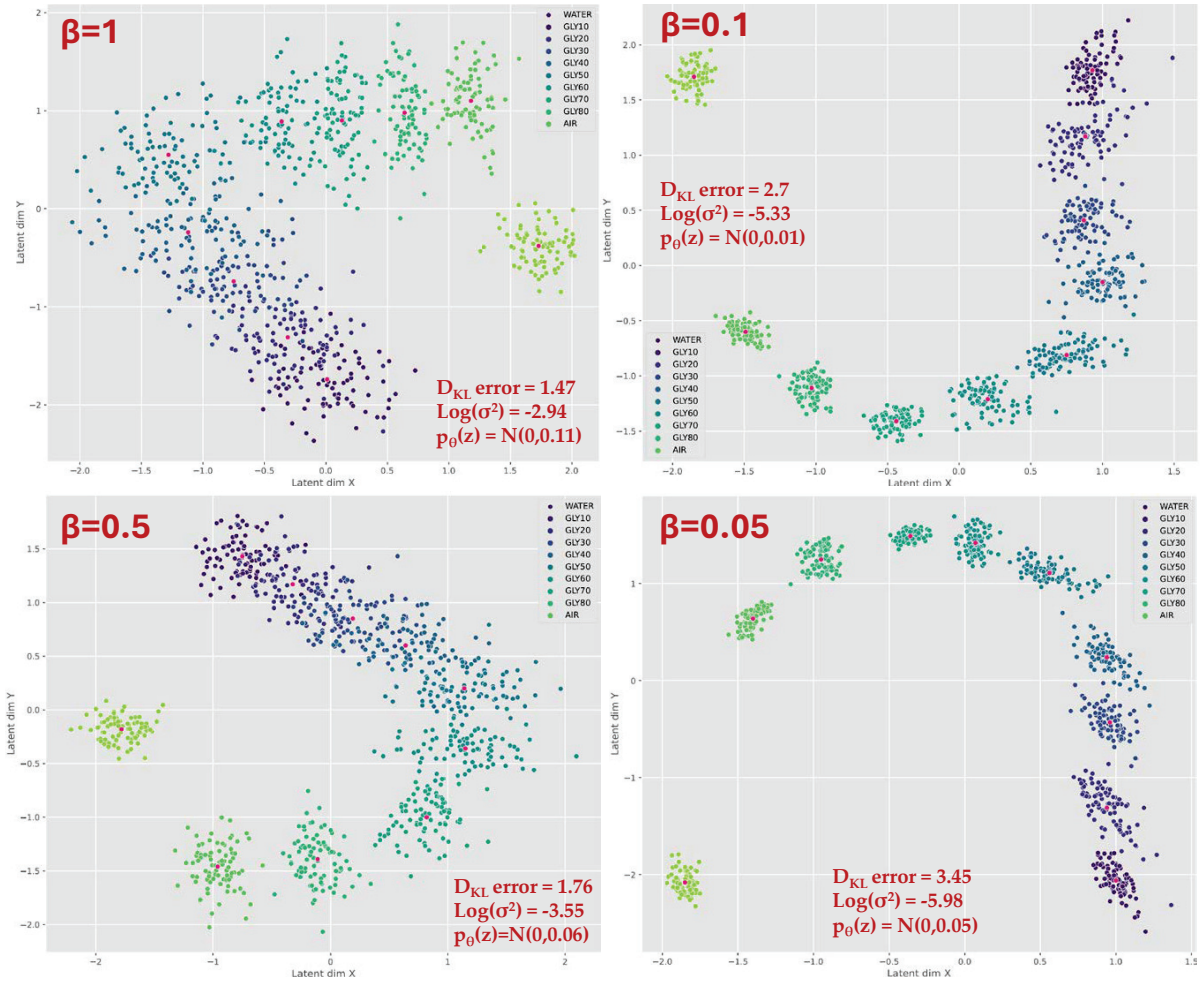

Figure 6.7: *Latent representation of the training dataset. The changes in the latent space shape for different values of β impact into the class separability.*

The value $\beta = 0.1$ is the most optimal for interpolation since it obtains a balanced compromise between the D_{KL} error and class separability without hindering the reconstruction capability (Figure 6.6), which is resilient to changes in latent space shape.

Manual search

The most straightforward interpolation approach for generating a specific synthetic signal is through a visual study of the latent space in order to select the area of interest. However, this approach is limited to low-dimensional latent spaces. In addition, it lacks generalization since the learned latent space rotates in each model (Figure 6.7). Despite these limitations, a manual search is an interesting first step to validate the VAE generation performance.

The objective of this research is to generate signals of glycerine concentrations unmeasured by the sensor. Therefore, the latent space between clusters is the target area since the VAE should have learned to encode that area as the unseen sensor behavior. To prove this hypothesis, several latent vectors representing points between glycerin concentrations were chosen to be decoded (Figure 6.8 *(left)*). Indeed, the generated signals are plotted between the average signals of the original concentrations (Figure 6.8 *(right)*). Therefore, they are plausible interpolations of intermediate concentrations. Nevertheless, the signals are a bit noisy, indicating a slightly worse reconstruction quality, which could be improved with a noise filter or reducing the β value.

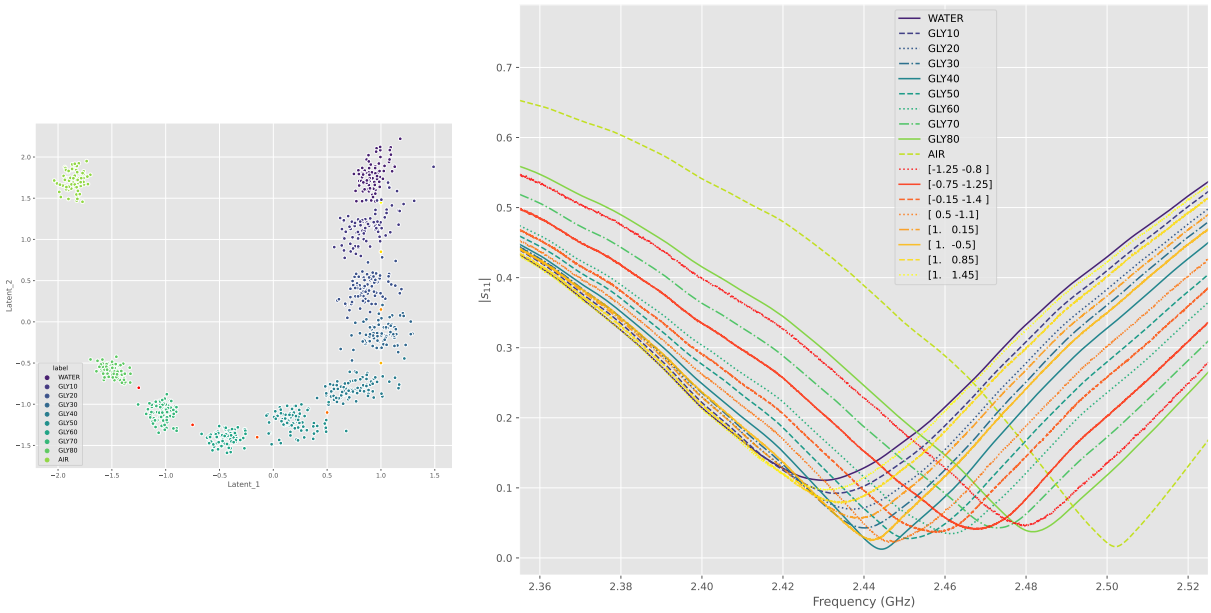

Figure 6.8: *Selected latent vectors between concentration clusters (left) and the corresponding decoded signals (right).*

In the same way, Figure 6.9 explores the latent space between the classes "AIR" and "GLY80" showing a reasonable progression of signals that could represent a gradation of permittivity. However, the interpolation quality is lower in both shape and noise-signal ratio compared to Figure 6.8. This reduction of fidelity could be due to the large separation in the latent space, which represents an excessive permittivity shift, hindering the VAE model learning of the sensor behavior. In contrast, the shorter latent distances, as in Figure

6.8, demonstrate the potential of VAE models to generate unmeasured classes. Therefore, a balanced class separability is a key factor, it must allow sufficient space to interpolate but at the same time not hinder the VAE learning. Class separability also depends on sensor sensitivity, and therefore, these results indicate that the interpolation capacity of the VAE framework cannot exceed the detection limit of the sensor.

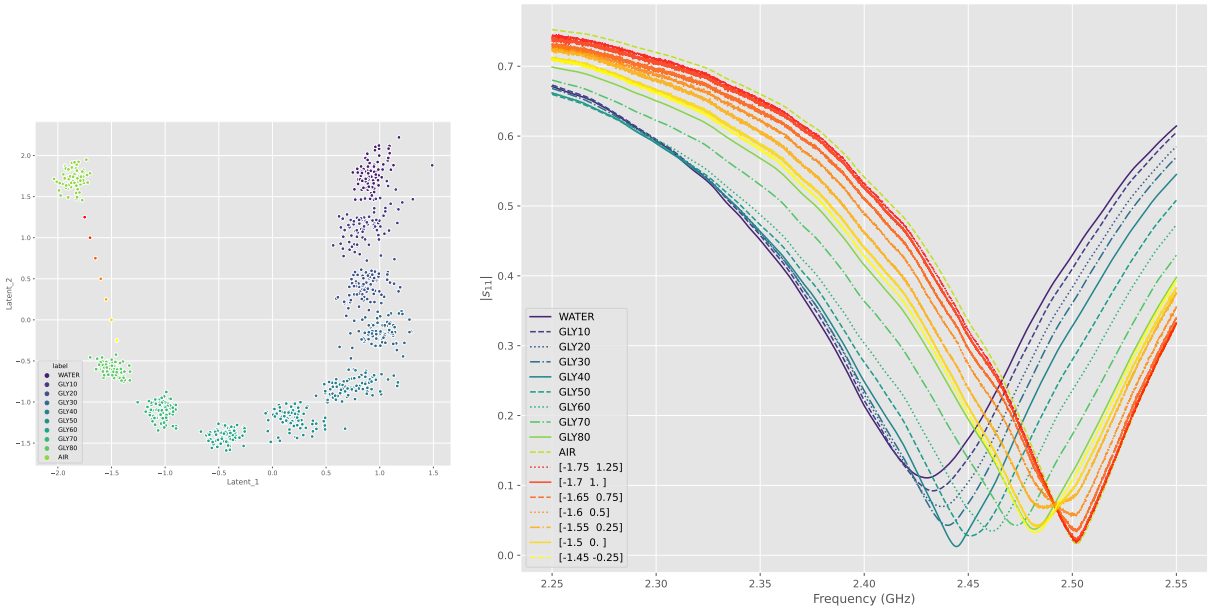

Figure 6.9: *Selected latent vectors between the AIR and GLY80 clusters (left) and the corresponding decoded signals (right).*

Bayesian latent space search

The previous approach indicates how to evaluate the results from the Bayesian latent space search. Consequently, the interpolation method should converge in the regions between clusters where the target permittivity corresponds to an intermediate concentration. Since the Bayesian search method was tested to generate signals with a permittivity of 30, the method should select a latent vector in the latent space between the glycerin classes of 70% and 60%. The method was initialized 20 times to evaluate its reproducibility. However, only a fraction of these vectors converged in the desired area between clusters (Figure 6.10). Likewise, the generated signals show an erratic behavior corresponding to the disparity of "optimal" latent vectors found by the method.

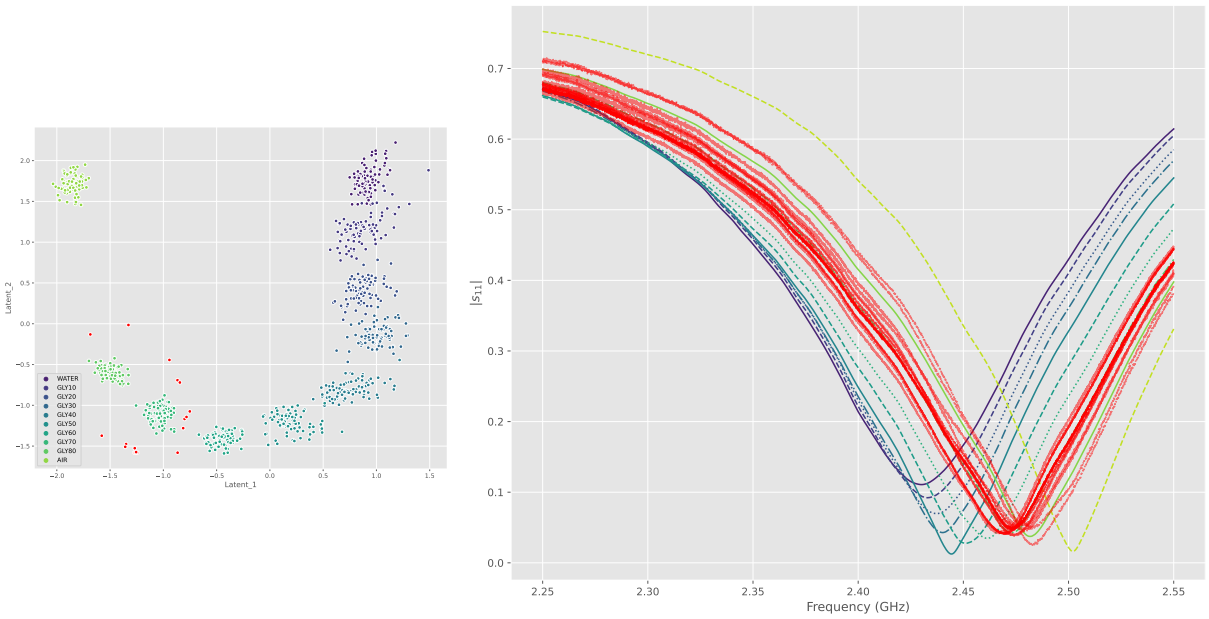

Figure 6.10: *Optimal latent vectors found by the Bayesian search method that minimizes the regression for $\varepsilon_r = 30$ (left) and the corresponding decoded signals (right).*

One of the reasons for this error lies in how the SVR model maps the latent space during the training, which is tuned by the gamma hyperparameter. Indeed, Figure 6.11 compares two SVR models trained with the same latent vectors but applying a different gamma. Whereas a high value ($\gamma = 3.5$) fits better the shape of the clusters to minimize the regression error ($RMSE = 0.67$), the resulting latent space map is very irregular. In contrast, a lower value of gamma ($\gamma = 0.1$) generates smoother transitions in the latent space but at the cost of losing prediction accuracy ($RMSE = 1.22$).

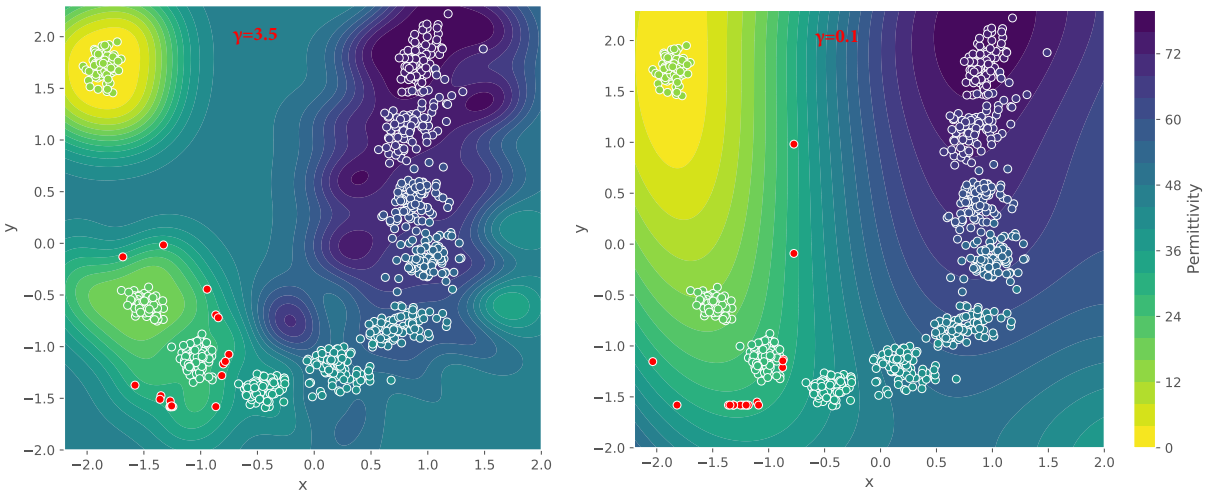

Figure 6.11: *The effect of γ in SVR permittivity predictions within the latent space.*

Nevertheless, it is not clear that sacrificing model precision could achieve a better convergence. As depicted in Figure 6.11, for both gamma values, the Bayesian latent explorer successfully converges in regions where the SVR predicts the requested target permittivity. Therefore, the failure of the proposed search method is mostly due to the dissonance between the permittivity map learned by the SVR and the latent space learned by the VAE model. Therefore, since both models learn different spaces, using only the SVR feedback to guide the Bayesian search leads to a very inefficient search method. Given these results, it is proposed to modify the Bayesian Optimization search target to include the reconstruction error of the closest clusters (Equation 6.9). Where F is a tuneable factor to correct the error dimension.

$$\begin{aligned} \varepsilon_z &= SVR(z) \qquad RE = MSE(decoder(z), decoder(z_{class})) \\ z_{opt} &= \arg\min_{z\in\mathbb{R}}[abs(\varepsilon_z - \varepsilon_{target}) + F * (RE_{class\uparrow} + RE_{class\downarrow})] \end{aligned} \tag{6.9}$$

The new optimization function includes the competition between the reconstruction errors of the closest concentrations to the target permittivity. Balancing these errors drives the search method to find the area between both class clusters (Figure 6.12). Thus, the Bayesian search obtains a better convergence and more plausible interpolated signals.

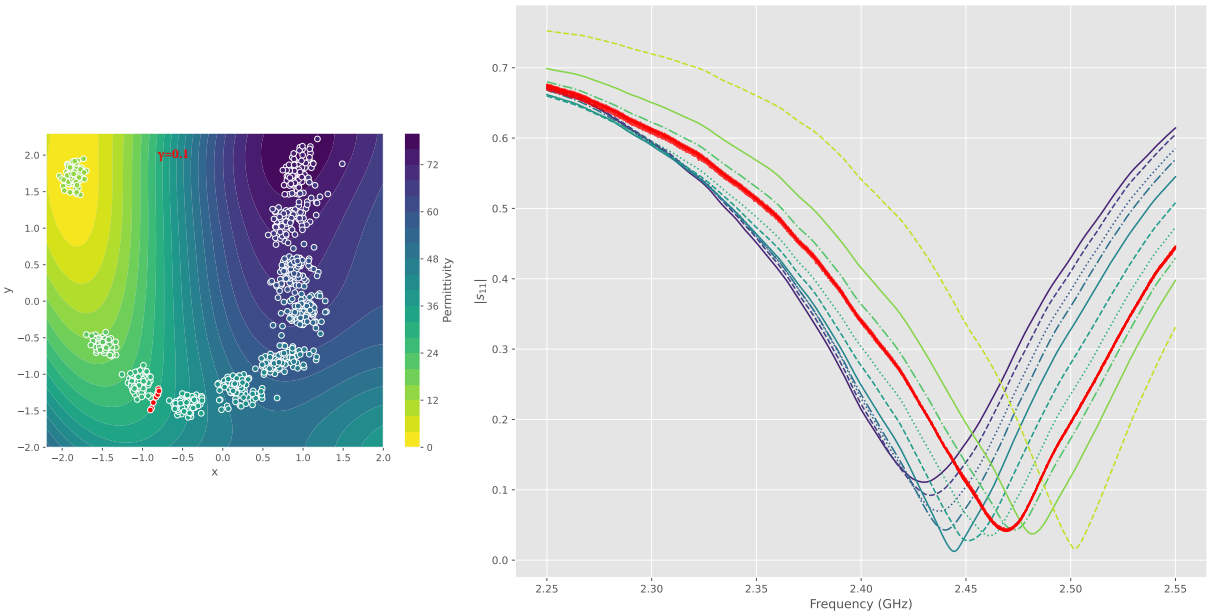

Figure 6.12: *New latent vectors found by the improved Bayesian search method with the new optimization objective (left) and the corresponding decoded signals (right).*

6.7. Conclusions

In the last few years, the VAE framework has lost the spotlight against other generative models for image generation and large language models (LLMs). Nevertheless, the results of this Chapter indicate that this model architecture can be employed for the generation of sensor signals. Since the data structure of frequency signals is relatively less complex, the VAE advantages, such as simplicity or fast training, can be exploited without suffering its poor performance in comparison to GANs or diffusion models. In conclusion, the VAE models are the perfect tool for this novel application. On the other hand, the Bayesian latent space search method proposed in this chapter could be applied to more complex models and data sources. Therefore, future studies should test this alternative, performing a comparative analysis with this work and addressing the potential of this method.

BIBLIOGRAPHY

[1] O. Steven Eyobu and D. Han, "Feature representation and data augmentation for human activity classification based on wearable imu sensor data using a deep lstm neural network," *Sensors*, vol. 18, no. 9, p. 2892, 2018.

[2] M. Ding, "The road from mle to em to vae: A brief tutorial," *AI Open*, vol. 3, pp. 29–34, 2022.

[3] L. Ruthotto and E. Haber, "An introduction to deep generative modeling," *GAMM-Mitteilungen*, vol. 44, no. 2, p. e202100008, 2021.

[4] K. P. Murphy, *Probabilistic Machine Learning: Advanced Topics*. MIT Press, 2023.

[5] A. Asperti and M. Trentin, "Balancing reconstruction error and kullback-leibler divergence in variational autoencoders," *IEEE Access*, vol. 8, pp. 199440–199448, 2020.

[6] D. P. Kingma and M. Welling, "An introduction to variational autoencoders," *Foundations and Trends® in Machine Learning*, vol. 12, no. 4, pp. 307–392, 2019.

[7] I. Goodfellow, Y. Bengio, and A. Courville, *Deep learning*. MIT press, 2016.

[8] A. Singh and T. Ogunfunmi, "An overview of variational autoencoders for source separation, finance, and bio-signal applications," *Entropy*, vol. 24, no. 1, 2022.

[9] S. Chen and W. Guo, "Auto-encoders in deep learning—a review with new perspectives," *Mathematics*, vol. 11, no. 8, 2023.

[10] R. Wei, C. Garcia, A. El-Sayed, V. Peterson, and A. Mahmood, "Variations in variational autoencoders - a comparative evaluation," *IEEE Access*, vol. 8, pp. 153651–153670, 2020.

[11] S. Bond-Taylor, A. Leach, Y. Long, and C. G. Willcocks, "Deep generative modelling: A comparative review of vaes, gans, normalizing flows, energy-based and autoregressive

models," *IEEE Transactions on Pattern Analysis and Machine Intelligence*, vol. 44, no. 11, pp. 7327–7347, 2022.

[12] I. Eddahmani, C.-H. Pham, T. Napoléon, I. Badoc, J.-R. Fouefack, and M. El-Bouz, "Unsupervised learning of disentangled representation via auto-encoding: A survey," *Sensors*, vol. 23, no. 4, 2023.

[13] C. Guo, J. Zhou, H. Chen, N. Ying, J. Zhang, and D. Zhou, "Variational autoencoder with optimizing gaussian mixture model priors," *IEEE Access*, vol. 8, pp. 43992–44005, 2020.

[14] A. Asperti, D. Evangelista, and E. Loli Piccolomini, "A survey on variational autoencoders from a green ai perspective," *SN Computer Science*, vol. 2, no. 4, 2021.

[15] C. P. Burgess, I. Higgins, A. Pal, L. Matthey, N. Watters, G. Desjardins, and A. Lerchner, "Understanding disentangling in β-vae," 2018.

[16] P. Fernandes, J. Correia, and P. Machado, "Evolutionary latent space exploration of generative adversarial networks," in *Applications of Evolutionary Computation: 23rd European Conference, EvoApplications 2020, Held as Part of EvoStar 2020, Seville, Spain, April 15–17, 2020, Proceedings 23*, pp. 595–609, Springer, 2020.

[17] W. Zheng, J. Li, and Y. Zhang, "Desirable molecule discovery via generative latent space exploration," *Visual Informatics*, vol. 7, no. 4, p. 13–21, 2023.

[18] Y. Liu, E. Jun, Q. Li, and J. Heer, "Latent space cartography: Visual analysis of vector space embeddings," *Computer Graphics Forum (Proc. EuroVis)*, 2019.

[19] B. Machin, S. Nesmachnow, and J. Toutouh, "Evolutionary latent space search for driving human portrait generation," in *2021 IEEE Latin American Conference on Computational Intelligence (LA-CCI)*, IEEE, Nov. 2021.

[20] H.-I. On, L. Jeong, M. Jung, D.-J. Kang, J.-H. Park, and H.-J. Lee, "Optimal design of microwave absorber using novel variational autoencoder from a latent space search strategy," *Materials & Design*, vol. 212, p. 110266, Dec. 2021.

[21] C. Liu, R. Antypenko, I. Sushko, and O. Zakharchenko, "Intrusion detection system after data augmentation schemes based on the vae and cvae," *IEEE Transactions on Reliability*, vol. 71, no. 2, 2022.

[22] T. Jahan, Y. Guan, and O. van Kaick, "Semantics-guided latent space exploration for shape generation," *Computer Graphics Forum*, vol. 40, no. 2, p. 115–126, 2021.

CHAPTER 7

CONCLUSIONS

According to the papers published during the development of this PhD research, it can be stated that the objectives established at the beginning of this thesis (Chapter 1) have been covered. The findings of this research not only provide practical methodologies for improving the performance of Microwave resonant sensors (Chapters 2,4), but also advance our understanding of the dielectric behavior of liquid mixtures (Chapter 5).

The main success of this PhD research corresponds to the validation that low-cost electronics and open-hardware designs supported by ML techniques can obtain a great performance similar to complex electronic instruments (Chapter 4). Moreover, while commercial instruments come with fixed specifications, open hardware offers modular and flexible architectures with the inherent benefit of customization. Thus, the sensor design can be tailored to meet the requirements of any analytical objective. The insights from this PhD indicate the advantages of integrating Machine Learning with low-cost platforms such as Arduino or Raspberry Pi to develop low-cost sensing devices.

Nevertheless, this PhD research faced certain limitations, such as the lack of permittivity values in the microwave range for many substances of interest, hindering the training of ML regression models (Chapter 4). This issue led to a review of the modification of mixing rules to obtain useful permittivity estimation from the pure liquid characteristics (Chapter 5). Another limitation lies in the training dataset construction, which requires a significant number of samples to ensure the model learning. Therefore, this demands time investment for designing and performing experiments and can critically depend on the analytical target. The promising results in Chapter 6 offer a complementary method for reducing costs and time by generating synthetic signals to enlarge the dataset.

In summary, applying Machine Learning techniques combined with MW resonant structures has yielded significant contributions to developing low-cost sensors, which are listed below.

Contributions

- A novel and fast nanoparticle characterization method based on their sedimentation dynamics measured by a Square Spiral Resonator sensor. This method can determine the concentration of nanoparticles and chemical composition **(O-1 ✓)**.

- A workflow based on ML techniques for sensing data for classifying liquids solution and their relative permittivity estimation **(O-2 ✓)**.

- A demonstration that low-cost portable electronics can achieve comparable results to complex electronic instrumentation equipment with the help of ML models for signal analysis **(O-2 ✓)**.

- A methodology to validate permittivity characterizations based on minimizing the regression error of ML models. This approach can also be applied to select the best mixing rule estimations for a specific binary so-

lution. In addition, the model error can indicate an optimal range of the interaction factor that modifies the mixing rules to obtain better permittivity estimations **(O-3 ✓)**.

- A multiparametric Gaussian modification formula to model the mixture dielectric behavior improves the match between mixing rule estimations and experimental values. This formula provides physically realistic volume fraction modifications, and it is supported by a novel estimation of the interaction factor through the molar volume ratio and the dielectric contrast **(O-3 ✓)**.

- An exploration of Variational Autoencoders representative learning for the generation of synthetic signals of MW resonant sensors. A solid foundation for future developments to enhance the training datasets for the previously commented ML workflow for sensors **(O-4 ✓)**.

Publications

The contributions achieved by this PhD research are collected in this compendium of three articles published in high-impact factors journals:

- **(Chapter 3) –** *"Measuring sedimentation profiles for nanoparticle characterization through a square spiral resonator sensor"*, **Sensors, vol. 24, no. 9, 2024. (JCR: 3,900 12 (2022) – SJR: 0,764 q1 (2022))**

- **(Chapter 4) –** *"Low-cost electronics for automatic classification and permittivity estimation of glycerin solutions using a dielectric resonator sensor and machine learning techniques"*, **Sensors, vol. 23, no. 8, 2023. (JCR: 3,900 q2 (2022) – SJR: 0,764 q1 (2022))**

- **(Chapter 5) –** *"A machine learning approach for enhancing permittivity mixing rules of binary liquids with a gaussian modification and a new interaction factor estimation"*, **Journal of Molecular Liquids, vol. 399, p.124290, 2024. (JCR: 6,000 q1 (2022) – SJR: 0,914 q1 (2022))**

In addition, the preliminary results of these works were presented at several conferences:

- *"Automatic classification and permittivity estimation of organic solvents using a dielectric resonator sensor and machine learning techniques"*, **XXXVII Simposio Nacional de la Unión Científica Internacional de Radio - URSI 2022, Malaga (Spain). 05-07 September 2022.**

- *"Automatic classification and permittivity estimation of glycerin solutions using a dielectric resonator sensor and machine learning techniques"*, **IEEE International Instrumentation and Measurement Technology Conference - I2MTC 2023, Kuala Lumpur (Malaysia). 22-25 May 2023.**

- *"A Machine Learning approach for the validation and optimization of permittivity mixing rules for binary liquids"*, **XXXVIII Simposio Nacional de la Unión Científica Internacional de Radio - URSI 2023, Caceres (Spain). 13-15 September 2023.**

Future research

The contributions of this PhD thesis have opened many interesting research lines that should be addressed in future works. In the first place, the results of Chapter 3 suggest that the sedimentation profile measured could reveal other nanoparticle characteristics, such as particle size distribution. More studies must be conducted to determine the full capability of this characterization method. In addition, the workflow to implement ML techniques in sensing applications developed in Chapter 4 is not limited to the tested devices. Indeed, this workflow could be applied to any sensor technology, and therefore, it must be tested with new analytical targets to confirm its versatility and reach its whole potential.

On the other hand, Chapter 5 explored the dielectric behavior of binary liquids and how to improve mixing rules to model it. Nevertheless, the re-

lationship between the proposed Gaussian modification and the nature of the molecular interaction is still unknown and demands further studies.

Finally, the results in Chapter 6 are promising to enlarge and enhance the sensor dataset. However, these preliminary insights are only the first steps in an interesting field that requires exploring Deep Learning architectures to ensure the interpolation of unseen synthetic signals.